Fermilab

FERMILAB-THESIS-2000-04

Atomic mass dependence of Ξ^- and $\overline{\Xi}^+$ production in central 250 GeV/c π^--nucleon interactions

A dissertation

submitted by

William David Dagenhart

In partial fulfillment of the requirements

for the degree of

Doctor of Philosophy

in

Physics

TUFTS UNIVERSITY

February 2000

Adviser: Austin Napier

ABSTRACT

Atomic mass dependence of Ξ^- and $\overline{\Xi}^+$ production in central 250 GeV/c π^--nucleon interactions

William David Dagenhart

Adviser: Austin Napier

Fermilab E769 Collaboration

We present the first measurement of the atomic mass dependence of central Ξ^- and $\overline{\Xi}^+$ production. It is measured using a sample of 22,459 Ξ^-'s and $\overline{\Xi}^+$'s produced in collisions between a 250 GeV/c π^- beam and targets of beryllium, aluminum, copper, and tungsten. The relative cross sections are fit to the two parameter function $\sigma_0 A^\alpha$, where A is the atomic mass. We measure $\alpha = 0.924 \pm 0.020 \pm 0.025$, for Feynman-$x$ in the range $-0.09 < x_F < 0.15$.

Acknowledgements

I'm indebted to many people for their help and support while completing this dissertation. Austin Napier provided guidance from start to finish. Austin, Jeff Appel, and Paul Karchin spent many hours listening and giving advice during E769 phone meetings and collaboration meetings. I would have never finished without them.

Juan Astorga and David Passmore gave their time and help when I was new to the Fermilab E769 collaboration. They taught me how to use the E769 software, access the data, and find Ξ^-'s. They were around to discuss E769 problems, physics, and other things. I missed them after they graduated.

I also have to thank the rest of the E769 collaboration. Some provided guidance and help, like Andrew Wallace, Marleigh Sheaff, and Simon Kwan. There were many others I never met. They built the detector and collected the data used for this dissertation.

I appreciate the opportunity Krzysztof Sliwa gave me with the CDF collaboration. Although my CDF work did not contribute to my thesis, it was a valuable part of my physics education. It has contributed a great deal to my future in physics. I also enjoyed working with the other members of the Tufts CDF group, Simona Rolli and Kristo Karr.

My father, my mother, my brother Jon, and my sister Pam have been always been there for me when I needed them. Their love and support has been there throughout my time in graduate school.

I thank the members of my thesis committee, Austin Napier, Jeff Appel, Krzysztof Sliwa, Roger Tobin, and Jack Schneps.

Contents

List of Tables

List of Figures

Chapter 1

Introduction

The atomic mass dependence of strong interaction cross sections is sensitive to the behavior of hadrons and quarks inside nuclear matter. In addition, knowledge of this dependence is needed to compare cross section results from experiments using different target materials. Many atomic mass dependence measurements have been made. Nevertheless, little exists in the literature for central hyperon production. This dissertation describes the first measurement of the atomic mass dependence of central Ξ^- and $\overline{\Xi}^+$ production. The results were published in Physical Review D [1, 2].

The atomic mass dependence of cross sections is frequently parameterized as

$$\sigma = \sigma_0 A^\alpha \ ,$$

where A is the atomic mass of the target. By using four target materials, α is measured and the applicability of this parameterization is checked.

The first part of this document describes the work done by others. Chapter 2 describes some of the theory. It is brief and its purpose is to put the dissertation in the proper context. The material should be familiar to particle physicists. Chapter 3 describes other experimental measurements of atomic mass dependence. Chapter 4 describes the Fermilab E769 detector used to collect the data.

The rest of the document describes the data analysis used to derive the results and estimate the errors. This part of the document should be familiar to E769 collaborators. It is simply a version of the internal E769 memorandum [3] with the text heavily edited and the figures reformatted. About half the information was deleted in the editing process, so one might still want to reference the internal memorandum for some things. Chapter 5 describes the process of selecting and copying interesting data events from the large set of data tapes to one Ξ^- strip tape. Chapter 6 describes the steps necessary to determine the data signal for each target material. Chapter 7 describes the simulation and the acceptance calculation. In Chapter 8, it is all put together. The atomic mass dependence results are calculated. The first appendix describes the systematic error calculation.

The last appendix is really unrelated to the rest of the thesis. It briefly describes other research activities performed as part of the CDF collaboration.

There is one convention adopted throughout this document to make it easier to read. In everything that follows, charge conjugates are implied unless it is explicitly stated otherwise. For example, "Ξ^- cross-section" will actually mean "Ξ^- cross-section plus the $\overline{\Xi}^+$ cross-section." This also applies to particles produced in Ξ^- decay.

Chapter 2

Background

To put this thesis in the proper context, this chapter gives a brief review of the Standard Model and the development of QCD. It concludes with a description of how the process studied in this analysis fits into the Standard Model.

2.1 The Standard Model

The Standard Model describes nature in terms of particles whose behavior and interactions are described by quantum fields. One can divide the elementary particles into two types. One type includes all particles that are the building blocks of what we commonly think of as matter. Both quarks and leptons fall in this category. The other type includes particles that mediate the forces and are called mediators or gauge bosons.

Each of these particle types has a characteristic spin. Quarks and leptons have spin 1/2. A fermion is defined as a particle with half integral spin, therefore quarks and leptons are fermions. The mediators have spin 1. A boson is defined as a particle with integral spin, therefore mediators are bosons.

The different types of fermions are shown in Table 2.1. Quarks come in "flavors". The six possible quark flavors are listed in the first two columns of Table 2.1. Each

	Quarks		Leptons	
	down	up	electron	electron neutrino
	strange	charm	muon	muon neutrino
	bottom	top	tau	tau neutrino
Charge	$-1/3$	$+2/3$	-1	0

Table 2.1: Elementary particles with spin 1/2, fermions.

flavor has a characteristic mass and charge. The up and down quarks have a mass that is small compared to their typical binding energies. The other quark flavors get progressively more massive in the order: strange, charm, bottom, top. The down, strange, and bottom quarks have charge $-1/3$. The up, charm, and top quarks have charge $+2/3$.

Quarks carry another property that is analogous to electrical charge called "color". Electrical charge comes in one variety and the electrical charge of an object is specified by one number. Color comes in three varieties called "red", "blue", and "green". Note that "color" has nothing to do with the common definition of color, which relates to visible light. "Color", "red", "blue", and "green" are just labels for things which have no other name. The relationship of color to the strong force is similar to the relationship of electrical charge to the electromagnetic force. One can have a green down quark, a blue down quark, or a red down quark. In a sense, there are three elementary particles for each flavor of quark, one for each color.

The different types of leptons are shown in the last two columns of Table 2.1. Leptons do not have color and do not interact via the strong force. The electron, muon, and tau have charge -1. The electron is the lightest of the charged leptons, the muon has medium weight, and the tau is the heaviest. The three types of neutrinos have zero charge and zero or very small mass.

Relativistic quantum field theory requires that antiparticles exist for all types of

Mediator	Associated Force		Mass
Photon (γ)	Electromagnetic	Electroweak	0
W^+, W^-	Weak, Charged		80.3 GeV/c^2
Z^0	Weak, Neutral		91.2 GeV/c^2
Gluons	Strong		0

Table 2.2: Elementary particles with spin 1, bosons.

fermions. A particle and antiparticle have exactly the same mass and spin. They are affected by the same forces, but have opposite charge and opposite color.

The mediators are shown in Table 2.2. Each mediator can be associated with a kind of force. The photon is associated with electromagnetic forces. The W^+, W^-, and Z^0 are associated with the weak force. In the Standard Model, these forces are viewed as different aspects of a combined electroweak force. Interactions that are not governed by electroweak theory are governed by the theory of quantum chromodynamics (QCD). QCD describes the interactions that are the source of the strong force. The gluons are associated with the strong force. Gluons carry color and because of the different ways they carry color, there can be eight different types of gluon.

The Standard Model describes almost all phenomena in terms of the particles discussed above and the interactions of their quantum fields. There are a few exceptions. Gravity is not covered by the Standard Model. In high energy particle physics, gravitational effects are usually negligible. There is also one additional particle predicted by the Standard Model. Electroweak theory predicts the existence of at least one Higgs particle.

There are many textbooks where one can get further information on the Standard Model. For example, see *Introduction to Elementary Particles* by Griffiths [4].

2.2 Quark Model and QCD

The results of this thesis are driven by QCD processes. This section provides some more detail for this part of the Standard Model along with some historical perspective.

Today, grade school students know the structure of an atom. An atom is composed of negatively charged electrons orbiting around a nucleus which is much smaller than the size of the electron orbits. The nucleus consists of positively charged protons and uncharged neutrons. At the beginning of the twentieth century this was unknown. Many experiments were performed in the first third of the century to determine this structure.

The pivotal experiment in the discovery of the electron was performed by J. J. Thomson [5] in 1897. Thomson used electric and magnetic fields to measure the charge to mass ratio of particles in a beam in a cathode ray tube. This, combined with other evidence, led to a model of the atom as a combination of heavy positively charged particles that filled the volume of an atom. Small, light electrons were interspersed in this positively charged volume to balance the charge. This model was struck down in 1911 by Rutherford's [6] analysis of an experiment where a beam of alpha particles was scattered by a thin metal foil. The distribution of scattered particles as a function of the scattering angle was measured. They expected the distribution would drop exponentially as the angle increased. The actual result showed a significant number of particles scattered at large angles. Rutherford concluded that the large angle scattering could only be caused by a nucleus which is small and dense compared to the volume of the atom.

Consensus on the constituents of the nucleus was finally reached after Chadwick [7] discovered the neutron in 1932. Before 1932, it was known that α radiation on beryllium produced neutral particles. Chadwick studied the neutral particles to determine their properties. He studied the ionizing radiation produced when these

neutral particles collided with targets of hydrogen, helium, lithium, beryllium, carbon, air, and argon. From the velocities of the recoil particles, he deduced that the neutral particles had roughly the same mass as the proton.

A nucleus contains neutrons and protons packed densely together. The electromagnetic repulsion of the positively charged protons should make the nucleus fly apart. It was postulated that there was a "strong force" that holds the nucleons together. This force had to be short range since it had no macroscopic effects. In the early 1930's, the proton and neutron were the only particles known to interact via this strong force. Particles that interact strongly are called hadrons. Over the next thirty years, dozens of other hadrons were discovered. For example, in 1954 Cowan [8] confirmed the existence of the Ξ^-, which is the focus of this analysis. It was seen in cosmic rays using a cloud chamber. By measuring the momentum in a magnetic field and the ionization, Cowan was able to identify the charged decay products and measure the Ξ^- mass.

By the early 1960's, a large number of hadrons had been discovered. There were many efforts to organize and find patterns in the properties of these particles. Gell-Mann [9] and independently Zweig [10] came up with the quark model in 1964 to explain the patterns found in the hadrons. At that time, three flavors (up, down, and strange, abbreviated u, d, s) of quarks were sufficient to describe all the known hadrons. Baryons are combinations of three quarks. Mesons are composed of one quark and one antiquark. For example, a proton is made of two up quarks and one down quark (uud) and a neutron is made of one up quark and two down quarks (udd). The Ξ^- has two strange quarks and one down quark (ssd). Based on the quark model, Gell-Mann predicted the existence of the Ω^- particle. The particle was found not long after the prediction was made [11].

The quark theory was not immediately accepted by the physics community because of two problems. These problems actually turned out to be important properties of the strong force. First, no one has ever observed a bare quark. For the

last 30 years, many experiments have looked and failed. The theory now includes a property called confinement, which basically says that it is impossible to create a physical state with just one quark. The idea is that as quarks are separated the potential energy grows very large. At some point, a new quark-antiquark pair is created and this pair splits. One new quark going with each of the original quarks.

The second problem relates to the Ω^- particle. It is a fermion and must have an antisymmetric wavefunction [12]. The problem is that the space, flavor, and spin parts of this wavefunction are symmetric. Color was invented so that the wavefunction could be made antisymmetric. The color part of the wavefunction for the Ω^- and all baryons is

$$brg + rgb + gbr - bgr - grb - rbg \ .$$

This is a linear combination of states. For example, brg is the state with the first quark blue, the second quark red, and the third quark green. This linear combination reverses sign when two quarks are swapped. At the time, the invention of color was viewed skeptically. But over the last 30 years, a lot of experimental evidence has accumulated that confirms that color exists.

In the late 1960's, more evidence for the quark model appeared. Deep inelastic scattering experiments were performed. In these experiments, an electron with energy E is scattered off a proton with 4-momentum p. The electron exchanges a photon with the proton. The 4-momentum of the photon is q. After the collision, an electron is detected with energy E' scattered by angle θ. After the collision, the proton turns into a spray of many particles. One can derive the following formula for the cross section (see page 268 of [4]),

$$\frac{d\sigma}{dE'd\Omega} = \left(\frac{\alpha\hbar}{2Esin^2(\theta/2)}\right)^2 [2W_1 sin^2(\theta/2) + W_2 cos^2(\theta/2)] \ .$$

This formula is derived from the known electromagnetic factors for the photon exchange, general covariance arguments, charge conservation, and momentum conservation. The strong interactions that determine how the proton breaks up into a

spray of other particles are considered unknown. This unknown part is all in the functions $W_1(q^2, x)$ and $W_2(q^2, x)$. These are functions of $x \equiv -q^2/(2q \cdot p)$ and q^2 only. W_1 and W_2 can be measured experimentally in deep inelastic scattering.

Björken [13] predicted that for large q^2 and large $q \cdot p$

$$MW_1(q^2, x) \to F_1(x) \ ,$$

$$\frac{-q^2}{2Mc^2x} W_2(q^2, x) \to F_2(x) \ .$$

The significant point is that F_1 and F_2 do not depend on q^2. Callan and Gross [14] took this further and predicted that $2xF_1(x) = F_2(x)$. These theoretical predictions were based on the assumption that the electron scatters incoherently from pointlike constituents inside the proton. The predictions were motivated by existing data and verified experimentally at SLAC [15] in 1969 and in many other experiments.

The quark model gained acceptance in the general physics community after the discovery of the J/Ψ in 1974. It was discovered by two collaborations working independently. Samuel Ting's group was studying Drell-Yan production in proton–beryllium collisions at Brookhaven. Burton Richter's group was studying e^+e^- annihilation at SLAC. Both groups were surprised by the result. They published in November 1974 [16, 17]. The theoretical explanation of the high mass and long lifetime of the J/Ψ was based on the charm quark. This discovery was followed by the discovery of the bottom quark in 1977 by Lederman's group [18] at Fermilab. More recently, the top quark was discovered by the CDF [19] and D0 [20] collaborations at Fermilab in 1995.

QCD theory developed from the quark model. It is a gauge theory that is patterned after QED, the electromagnetic theory. QCD theory came together in the early and mid 1970's. Many contributed to its development. References [21, 22, 23] are but a few of the more significant papers. By 1978, QCD theory was essentially in its present form. The Standard Model is a combination of QCD and electroweak theory.

2.3 Ξ^- Production and Decay

Frequently, collision processes are divided into the following three stages.

- Hard Process
- Fragmentation
- Particle Decay

In the hard process, two partons interact. In this experiment, one parton comes from a π^- in the incident beam and one parton from a proton or neutron in a nucleus in the target. The partons could be the valence quarks. The valence quarks are bound together by the strong force. This means they are constantly exchanging gluons. These gluons can temporarily split into quark–antiquark pairs called sea quarks. The partons in the hard collision might be gluons or sea quarks instead of valence quarks. In this experiment, Ξ^- production is dominated by strong interactions between the two partons. The cross section is written in the form [24]

$$\sigma_{ij\to k} = \sum_{ij} \int dx_1 \int dx_2 f_i^1(x_1) f_j^2(x_2) \hat{\sigma}_{ij\to k}(x_1 x_2 s, \mu) \ .$$

The sum is over all different types of partons. The functions f_i^1 and f_j^2 are the parton distribution functions. These give the probability to find a parton with fraction x of the momentum of the beam π^- (superscript 1) or nucleon (superscript 2). $\hat{\sigma}$ is the hard partonic process cross section.

It would be nice to calculate the Ξ^- production cross section for different nuclear targets and compare to the experimental results. Unfortunately, the problem is too difficult to solve rigorously. There are several problems. The energy is low enough for it to be a nonperturbative calculation. The center of mass energy of the 250 GeV/c π^- beam and target proton is about 22 GeV. The vast majority of the Ξ^-'s have transverse momentum p_T less than 1.5 GeV/c. In addition, this is a many body

Particle	Mass	Lifetime
Ξ^-	1321 MeV/c^2	1.6×10^{-10} sec or 4.91 cm
Λ	1116 MeV/c^2	2.6×10^{-10} sec or 7.89 cm
π^-	140 MeV/c^2	2.6×10^{-8} sec or 780 cm
proton	938 MeV/c^2	$> 1.6 \times 10^{25}$ years

Table 2.3: Particle masses and lifetimes.

problem. One must consider all the quarks and gluons in the nuclear target. Also, there is frequently more than one inelastic collision within the nucleus.

After the hard process, there is a system of quarks and gluons flying out away from the collision point. These are connected by tubes or strings of virtual gluons and sea quarks. As these tubes are stretched, the amount of potential energy in them increases linearly with separation. Sooner or later they split producing quark-antiquark pairs. These pairs divide and join up with the quarks already flying apart to form hadrons. This process is called fragmentation. No one knows how to rigorously predict fragmentation results from QCD theory. Parametrizations based upon experimental data are generally used to model fragmentation.

After the hadrons are formed, the unstable ones decay. Nearly all Ξ^-'s decay in the mode

$$\Xi^- \rightarrow \Lambda + \pi^- \ .$$

The Λ decays by the two modes

$$\Lambda \rightarrow p + \pi^- \ ,$$

$$\Lambda \rightarrow n + \pi^0 \ .$$

The neutral mode is not detected in this analysis. The branching ratio for the charged mode is 63.9%. The lifetimes and masses of relevant particles are given in Table 2.3. Values were taken from the compilation of the Particle Data Group [25].

Chapter 3

Relevant Data on Atomic Mass Dependence from Other Experiments

There have been a large number of atomic mass dependence experiments performed in the last 50 years. The subject is very large. This chapter reviews only the most significant ones related to the quantity measured in this analysis. See the article by Fredriksson *et al.* [26] for a more complete review.

The atomic mass dependence of absorption cross sections is discussed first. The subject of particle multiplicity follows. Many interesting effects are seen by looking at the mass dependence of the inclusive differential cross sections. The last section describes the additive quark model and discusses the experimental results from that point of view.

3.1 Absorption Cross Sections

Carroll *et al.* [27, 28, 29] measured the absorption cross sections for many different targets and beams in the 1970's. To measure the cross sections, they placed scintillator detectors upstream and downstream of a target in a beam. Each beam particle was detected by the upstream scintillators. The downstream scintillators covered

a small solid angle when viewed from the target. The solid angle was symmetric around the beam out to a certain scattering angle. A particle that was not absorbed in the target would hit the downstream detector. A hit in the upstream scintillator with no corresponding hit in the downstream detector signaled an absorption. Using these data, they calculated the cross section. Unfortunately, this does not account for interactions where particles are emitted at small angles and hit the downstream scintillators. They repeated the experiment and moved the downstream scintillators so they covered different scattering angles. They measured the cross section as a function of angle. Then they extrapolated this function to a scattering angle of zero.

The absorption cross section is defined as follows:

$$\sigma_{absorption} = \sigma_{total} - \sigma_{elastic} - \sigma_{quasielastic} - \sigma_{Coulomb} \ .$$

The extrapolation procedure was also used to remove the elastic, quasielastic and Coulomb scattering events. They assumed the angular distributions for these events had specific functional forms that peaked at small scattering angles. The shape of the distributions allowed them to separate these parts of the cross section from the absorption cross section.

Carroll *et al.* repeated this procedure for many different energies and targets. They used Cerenkov detectors to identify the type of each beam particle. This allowed them to measure the absorption cross section separately for each type of beam particle. For each beam type and energy, they fit their cross section results to the following form:

$$\sigma = \sigma_0 A^{\alpha} \ .$$

In this equation, A is the atomic mass of the target. σ_0 and α are parameters determined from a fit to the data. σ is the measured absorption cross section. Their results are shown in Figure 3.1. The exponent α is shown in the top plot and the parameter σ_0 in the lower plot. The horizontal axis is the total hadron-proton cross section (including the elastic part). Note that σ_0 is not a good measure of

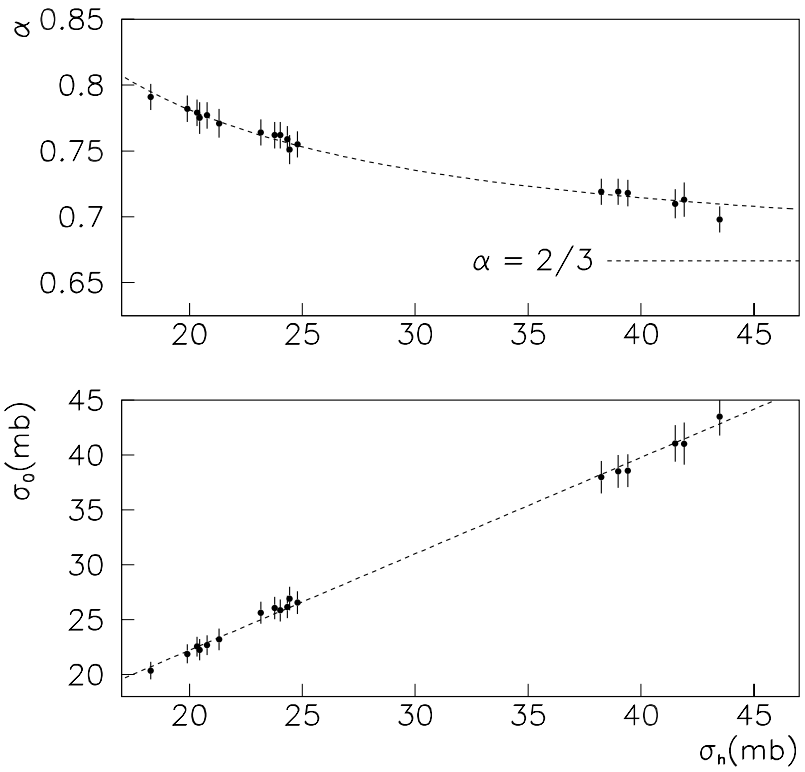

Figure 3.1: Atomic mass dependence (α and σ_0) of absorption cross sections for different beam particles and energies (see text). They are plotted as a function of the hadron-proton total cross section. The horizontal axis is the same for both plots. The lines are drawn to guide the eye. This is similar to Figure 4 in Ref. [28].

the hadron-proton absorption cross section. The parametrization fails at A = 1. Points are plotted for $K^{\pm}$, $\pi^{\pm}$, proton, and antiproton beam particles at 60, 200, and 280 GeV/c.

One can see three groups of data points in Figure 3.1. The data points with the highest total cross section (farthest right) are for the proton and antiproton beams. The six in the middle are from the pion beams. The six points to the left are from the kaon beams. Note that α for pions is typically 0.05 higher than for proton beams.

If the nuclear cross section were the sum of the cross sections of the protons and neutrons, then the value of α in the parametrization would be 1.0. One might expect this if the cross sections were small. The nucleons would be pointlike. On the other hand, if the nucleus behaved as a totally absorbing sphere and if the projectile were

small, then the cross section would be proportional to the area of the nucleus when projected onto a plane. In this case, the value of α would be 2/3. In the figure, α seems to asymptotically approach 2/3 as the cross section grows larger.

One can calculate the hadron-nucleus absorption cross section from the hadron-proton cross section and a density function for the nucleus using the Glauber model [30]. Carroll *et al.* found satisfactory agreement of their data with the Glauber model. Extending the Glauber model to inclusive or differential cross sections is problematic because so many other factors come into play. For example, one cannot predict the multiplicity of particle production from the Glauber model.

3.2 Particle Multiplicities

Multiplicity is the number of particles produced. DeMarzo *et al.* [31] reported results typical of multiplicity studies. Figure 3.2 shows the ratio between the multiplicity for Xenon-proton collisions and proton-proton collisions from that study. The multiplicities include all charged particles except slow protons. One can see three regions in the figure.

The target fragmentation region is at low rapidity. In this region, the multiplicity increases dramatically with atomic mass. Production in this region is usually modeled by a cascade process. Secondary particles are created in the primary interaction. In the cascade, the secondaries collide on their way out of the nucleus and create more particles. These particles usually have low momentum. Because of their low momentum, they have little direct impact on the results of the Ξ^- production reported in this thesis. They usually do not make it to the drift chambers or are swept away by the first magnet. Central Ξ^- production rarely falls in this region.

The central production region is of most interest. In this region, the multiplicity is higher by a factor between 1 and 3 for nuclear targets as compared to proton targets. This is the region that has the most effect on the results of this analysis.

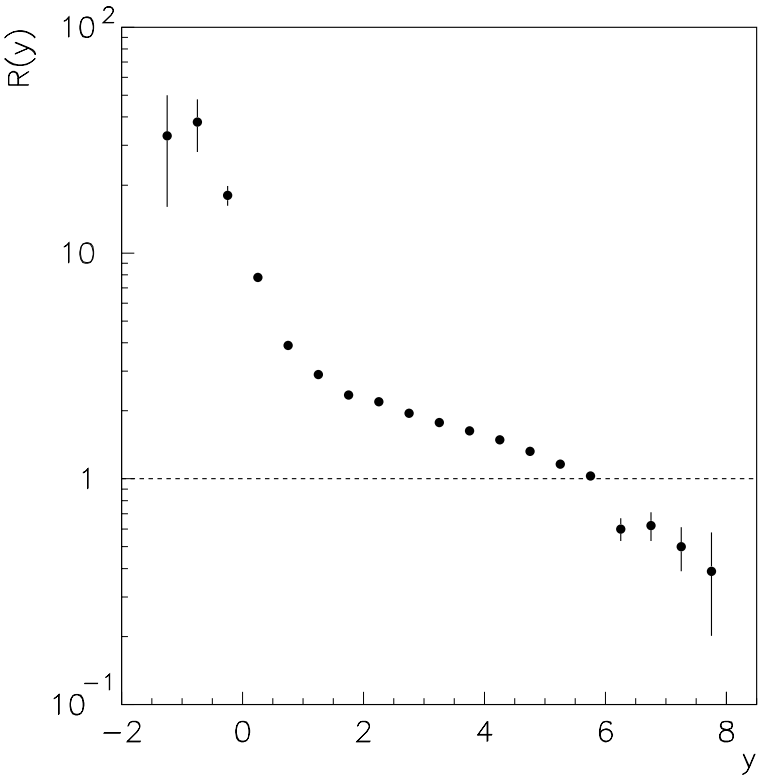

Figure 3.2: The particle multiplication ratio $R(y) = (d\sigma/dy)_{pXe}/(d\sigma/dy)_{pp}$ measured from proton-Xenon collisions and proton-proton collisions. The horizontal axis measures rapidity in the frame of the target. Data are from Figure 7 in Ref. [31].

This region includes both central Ξ^- production and production of particles that create background ionization tracks in the drift chambers.

The third region is the projectile fragmentation region. The multiplicity in this region is usually less for nuclear targets than for proton targets. A large fraction of the particles in this region are formed from quarks in the beam particle that do not interact in the target. These are usually called spectator quarks.

Multiplicity in the central and projectile fragmentation regions is not usually modeled by cascade processes. If cascade production occurred in these regions, then the multiplicities would be much higher. From a theoretical point of view, one discusses the formation length. When a constituent quark undergoes a collision it is absorbed. An intermediate state is formed. It takes time for that intermediate state

to coalesce into hadrons. For high momentum particles, relativistic effects cause this formation time to increase. The hadrons in the central and forward regions are not formed until after the intermediate state has traveled far enough to exit the nucleus. The intermediate state has a much lower cross section for soft inelastic collisions than a hadron. It does not usually interact in a way that increases multiplicity as it exits the nucleus. The review by Nikolaev [32] discusses formation length and its effect on multiplicity in some detail.

3.3 Inclusive Cross Sections

Inclusive cross sections are related to reactions of the form:

$$a + b \rightarrow c + X \ .$$

a is the beam particle. b is the target particle. c is the particle of interest. X is anything, which means any number of all kinds of particles. The cross section for this reaction is called the inclusive cross section for particle c. Inclusive cross sections are determined by both the cross section for the underlying hard processes and the multiplicity in those processes.

For a produced particle, x_F is defined as $p_{parallel}/p_{max}$, where $p_{parallel}$ is the component of momentum parallel to the beam and p_{max} is the maximum possible momentum. Both momenta are measured in the center of momentum frame of the beam hadron and target nucleon. Inclusive cross sections on nuclear targets are frequently parameterized in the forms

$$(Ed^3\sigma/dp^3)_A = A^{\alpha(x_F,p_T)}(Ed^3\sigma/dp^3)_{A=1} \ ,$$

$$(d\sigma/dx_F)_A = A^{\alpha(x_F)}(d\sigma/dx_F)_{A=1} \ ,$$

$$(d\sigma/dp_T)_A = A^{\alpha(p_T)}(d\sigma/dp_T)_{A=1} \ .$$

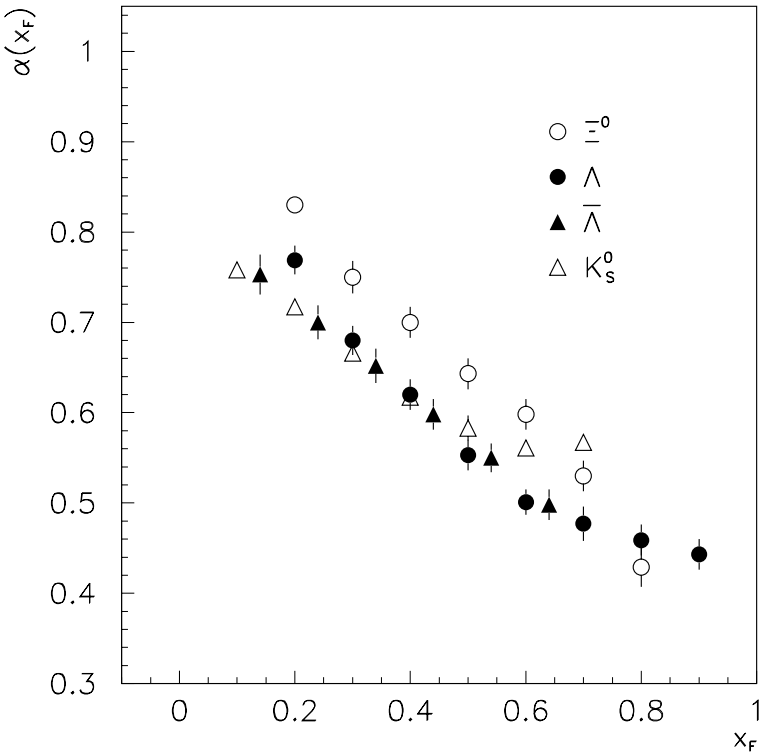

Figure 3.3: The exponent α in $\sigma = \sigma_0 A^\alpha$ as function of x_F (data from Figure 33 in Ref. [34]).

The parameter α varies significantly as a function of x_F and p_T. The plots on the next few pages show these trends, which were established in many experiments over the last 25 years.

Figure 3.3 shows α as a function of x_F for several different inclusive cross sections. In general, α is between 2/3 and 1 near $x_F = 0$. As x_F increases, α drops. In many cases it drops well below 2/3. The Ξ^0 data follow this trend for x_F between 0.2 and 0.8 [34, 35]. There are no published measurements for the Ξ^0 for x_F less than 0.2. One of the goals of this analysis is to fill the range near $x_F = 0$ using Ξ^- data. One expects the Ξ^- to behave like the Ξ^0, because both are composed of two strange quarks and one lighter quark.

In Figure 3.3, the distributions for the Λ, $\overline{\Lambda}$, and K^0_S are slightly lower than the Ξ^0 distribution. The Λ, $\overline{\Lambda}$, and K^0_S distributions are nearly the same. In fact,

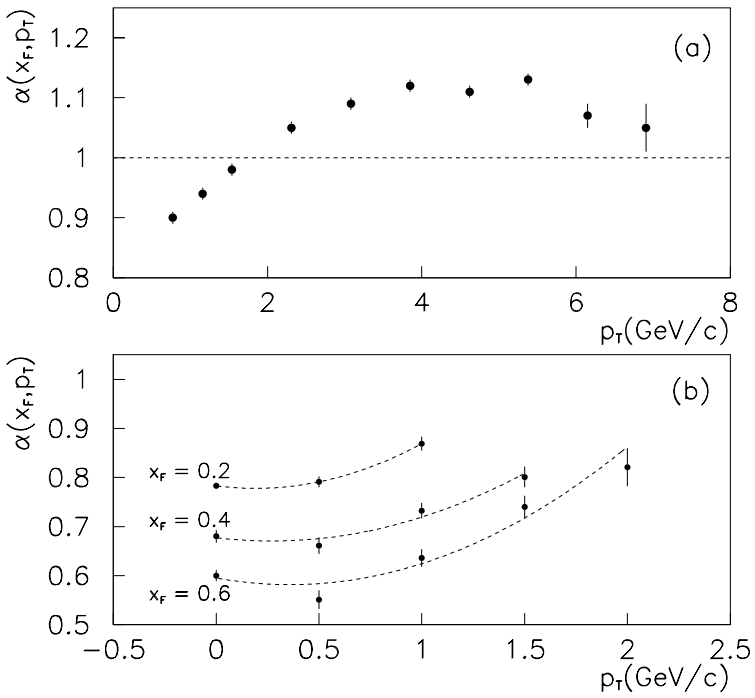

Figure 3.4: The exponent α in $\sigma = \sigma_0 A^\alpha$ as a function of p_T. Plot (a) shows α for the π^+ inclusive cross section near $x_F = 0$. The data are from Figure 2(a) of Ref. [36]. Note the horizontal axis in the upper plot covers a wider range of p_T than in the lower plot. Plot (b) shows α for the Ξ^0 inclusive cross section measurements. The Ξ^0 data are from Figure 31 in Ref. [34]. The lines are drawn to guide the eye to the points corresponding to each value of x_F.

studies [33] have shown that the distributions are very similar for many types of particles lighter than the Ξ^0.

Figure 3.4 shows the dependence of α on transverse momentum p_T. The distribution in the top plot is typical for most inclusive cross sections. As p_T rises, α rises and becomes greater than 1. This is interesting, because it means the cross section of a nucleus is greater than the sum of cross sections of the nucleons it contains. Usually, this is described in terms of multiple collisions enhancing the high p_T part of the spectrum for large nuclei. This was discovered for light particles in the 1970's [36, 37, 38].

Figure 3.4 (b) shows results for Ξ^0 production. Again, there are no published data available near $x_F = 0$ for the Ξ^0. A goal of this analysis is to study $\alpha(p_T)$ in

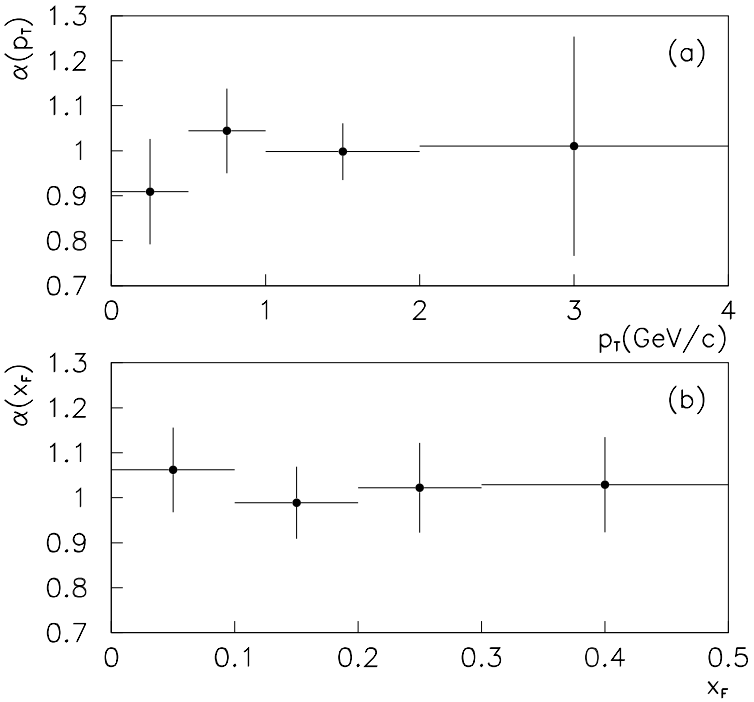

Figure 3.5: The exponent α in $\sigma = \sigma_0 A^\alpha$ for inclusive production of D^+, D^0, and their antiparticles. Plot (a) shows the dependence on p_T. Plot (b) shows the dependence on x_F. These measurements are from the same experiment as this analysis. See Figure 4 in Ref. [39].

the region near $x_F = 0$ with Ξ^- data.

This analysis measures α for Ξ^- production, but the Fermilab E769 experiment was actually designed primarily for charm measurements. One expects the mass dependence of charm production to be qualitatively different from the mass dependence of the production of lighter particles. The charm quarks are much more likely to be produced directly in the hard process. The hard process is expected to be more energetic and dominated by gluon–gluon fusion. It is much less likely that charm quarks will be produced during fragmentation than up, down, or strange quarks. For these reasons, α for charm mesons is expected to be closer to 1.0 and to depend less strongly on p_T and x_F than α for light particle production.

An earlier Fermilab E769 analysis measured α for some of the D mesons. The results are shown in Figure 3.5. The results are consistent with α being 1.0 for all the

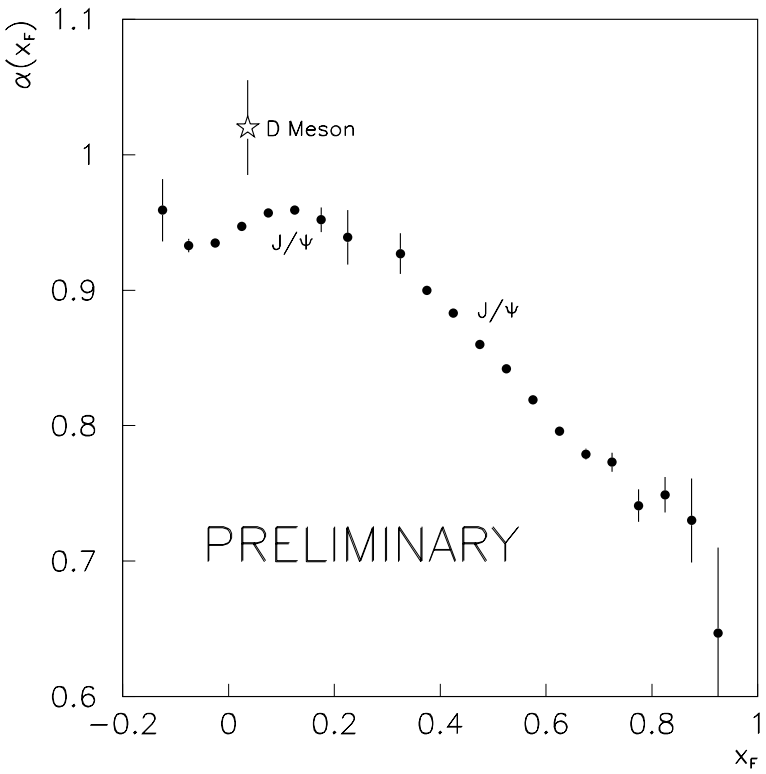

Figure 3.6: The exponent α in $\sigma = \sigma_0 A^\alpha$ as a function of x_F. These are very recent measurements from the Fermilab E866 collaboration. The solid circles show α for the J/Ψ inclusive cross section. The star shows data from an earlier experiment, Fermilab E789. Data are from Figure 3 in Ref. [40].

data points. Ref. [39] concludes that "this reinforces the picture that charm production and fragmentation are short-range processes and that the gluon distributions in various nuclei, in the x range probed by charm production, are similar."

The Fermilab E866 collaboration is currently working on a similar analysis for J/Ψ production. They have very high statistics. Figure 3.6 shows preliminary results shown at a workshop [40] last year. The distribution falls as x_F increases, as for lighter particles, but the slope of the drop is much smaller.

There is a lot of discussion about why the J/Ψ distribution is different from the distribution seen in the D mesons. The issue is not yet resolved. Measurements with higher statistics of the D meson cross section would help to resolve the issue.

One could ask whether Ξ production is more like charm production or production

Beam Particle	α	$\sigma_0(mb)$
Σ^-	0.679 ± 0.011	1.00 ± 0.04
n	0.891 ± 0.034	0.25 ± 0.03
π^-	0.931 ± 0.046	0.086 ± 0.013

Table 3.1: WA89 collaboration results for the atomic mass dependence of Ξ^- production (integrated over the region $x_F > 0$).

of lighter particles. The Ξ has two strange quarks. If they were produced together as a strange diquark, it would require almost as much energy as for charm production. If one looks at the x_F distribution, one sees that the Ξ distribution is higher than the distribution for the lighter particles, but lower than the distribution for charm. One would expect that the Ξ production process is harder than the processes responsible for production of light particles with zero or one strange quark and softer than the processes responsible for charm production.

The WA89 collaboration at CERN published [41] a measurement of the atomic mass dependence of Ξ^- production at the same time that the results of this thesis were published. These are the only two measurements of α for Ξ^- production. The WA89 result is interesting, because they measured the result for a Σ^- beam, a π^- beam, and a neutron beam. The WA89 results are summarized in Table 3.1.

The result for the Σ^- beam is significantly lower than for the π^- beam and the neutron beam. Most believe this is because the Σ^- (sdd) and Ξ^- (ssd) share two quarks. Spectator quarks from the Σ^- beam particle contribute significantly to Ξ^- production. Spectator quarks are much less likely to survive passage through a larger nucleus, and thus α is smaller for the Σ^- beam. This fits in with the additive quark model that is described in the next section.

3.4 Additive Quark Model

There is no universally accepted model to explain the atomic mass dependence of cross sections. There is a model based on particles losing momentum in collisions as they exit the nucleus [42, 43]. There is a model based on the quark recombination model [35]. In this model, the quarks lose momentum in the nucleus before they recombine. There is a dual parton model [44]. There are other models. The review by Zalewski [45] discusses the proliferation of models. Zalewski concludes that existing experimental measurements are not yet precise enough to exclude most of the models. One of the more popular models is the additive quark model.

The additive quark model was originally suggested by Anisovich *et al.* [46] in 1977. Many have written about this model or compared experimental results to the model [32, 34, 35, 47, 48, 45]. It does a reasonably good job of describing existing data. The additive quark model is usually used to describe the x_F dependence of α for forward and central production.

In the additive quark model, one looks at the beam particle as a system of constituent quarks. Sea quarks and gluons are ignored. In the case of a proton beam, there are three quarks. For a pion beam, there are two. In an inelastic collision, some of these quarks interact and some do not. The ones that interact are called wounded quarks. The ones that do not are called spectator quarks. The multiplicity in the central region is then proportional to the number of wounded quarks in the beam hadron. The particles at high x_F are formed primarily from spectator quarks.

The x_F dependence is written in the following form [48]:

$$g_{pA}^{B}(x_F)/\sigma_{pA} = P_{pA}^{(1)} g_{p\to B}^{(1)}(x_F) + P_{pA}^{(2)} g_{p\to B}^{(2)}(x_F) + P_{pA}^{(3)} g_{p\to B}^{(3)}(x_F) \ .$$

This is for the inclusive interaction $p + A \to B + X$. $P_{pA}^{(1)}$, $P_{pA}^{(2)}$, and $P_{pA}^{(3)}$ are the probabilities that 1, 2, or 3 quarks in the incident proton are wounded. All the atomic mass dependence is in these terms. They can be calculated from total inelastic cross

sections and assumptions about the distribution of matter in the nucleus. The functions $g^{(1)}_{p\to B}(x_F)$, $g^{(2)}_{p\to B}(x_F)$, and $g^{(3)}_{p\to B}(x_F)$ are empirically determined for each inclusive cross section. Note that they are independent of A. $g^{(1)}_{p\to B}(x_F)$ is larger than $g^{(2)}_{p\to B}(x_F)$ at high x_F, which is higher than $g^{(3)}_{p\to B}(x_F)$ at high x_F. For a pion beam, there is a similar equation without the term for three quarks interacting.

The probability that only one beam quark is wounded, $P^{(1)}_{pA}$, decreases as A increases. This means $g^{(1)}_{p\to B}(x_F)$ contributes less as the atomic mass increases. Since $g^{(1)}_{p\to B}(x_F)$ is large at higher x_F, production at high x_F is attenuated.

In other words, the spectator quarks are responsible for a lot of the forward production. Fewer spectator quarks survive passage through a larger nucleus. Therefore, α is lower at high x_F.

The data discussed in this chapter tend to support the additive quark model over models based on multiple collisions of particles produced in the primary interaction as they exit the nucleus.

- First, Figure 3.3 shows that $\alpha(x_F)$ is very similar for Λ, $\overline{\Lambda}$, and K^0_S production for proton beams. This would not be true for models based on particles slowing down in collisions as they exit the nucleus. Then $\alpha(x_F)$ would depend heavily on the x_F differential cross sections, which are very different for Λ and $\overline{\Lambda}$ production for proton beams.

- Second, one might expect multiple collision models to greatly increase multiplicity. Figure 3.2 shows the large increase in multiplicity at low rapidity. If this was occurring in central production, then α would probably be larger than 1.0. It is not. For all inclusive cross sections measured so far, α is less than or equal to 1.0 in the central region (except at high p_T). The type of production seen in the target fragmentation region simply does not occur in the central and forward regions. On the other hand, the additive quark mechanism for explaining the larger multiplicity would not raise α above 1.0 for

central production.

- Third, the assumption that gluons and sea quarks are ignored gets worse as we progress to production of heavier particles like the charm mesons. We also expect the spectator quarks to contribute less for forward charm production. We expect the slope of $\alpha(x_F)$ to be closer to zero for charm production. It is.

The additive quark model leads one to believe that α for central production is determined by the primary interaction, not secondary interactions of debris as it exits the nucleus, and not by spectator quarks. If one assumes the major factor that determines α is shadowing, then one concludes that α is a measure of the hardness of the production interaction. One can look at α for the inelastic cross section as a lower limit for the mass dependence of the central inclusive cross sections. For the inelastic cross section, α lies between 0.7 and 0.8 (see Figure 3.1). For light particle production, one can extrapolate in Figures 3.3 and 3.4 and see that near $x_F = 0$ and $p_T = 0$, α is roughly 0.85. From Figure 3.5, one can see that α for central charm production is near 1.0. For central Ξ^- production, one expects to find a value somewhere between 0.85 and 1.0, because the Ξ^- mass is higher than the mass of the light particles, but less than the mass of charm mesons.

Chapter 4

Detector Description

This analysis is based on data recorded using the Tagged Photon Spectrometer (TPS) at Fermi National Laboratory. This spectrometer has been used in a variety of experiments. This analysis uses data from the E769 era. The E769 collaboration focused on studies of charm hadroproduction using four different target materials with proton, kaon, and pion beams. The E769 data set was also excellent for studies of Ξ^- production. The E691 experiment preceded E769 and used the TPS to study photoproduction of charm. The E791 collaboration used the spectrometer after E769 and continued the studies of charm hadroproduction. Although E791 recorded much more data and had data from two target materials, a technical problem made the E791 data useless for atomic mass dependence measurements.

Figure 4.1 gives a view of the parts of the spectrometer downstream of the target. Table 4.1 shows the positions of the major components of the detector, as well as their area and resolution. The coordinate system used to describe the detector has its origin near the center of the beam, about 1 cm downstream of the target. The z axis points along the beam in the same direction as the incident particles. The y axis points vertically up. The x axis is horizontal and oriented to form an orthogonal right-handed coordinate system.

The first component of the detector was the DISC, which means differential

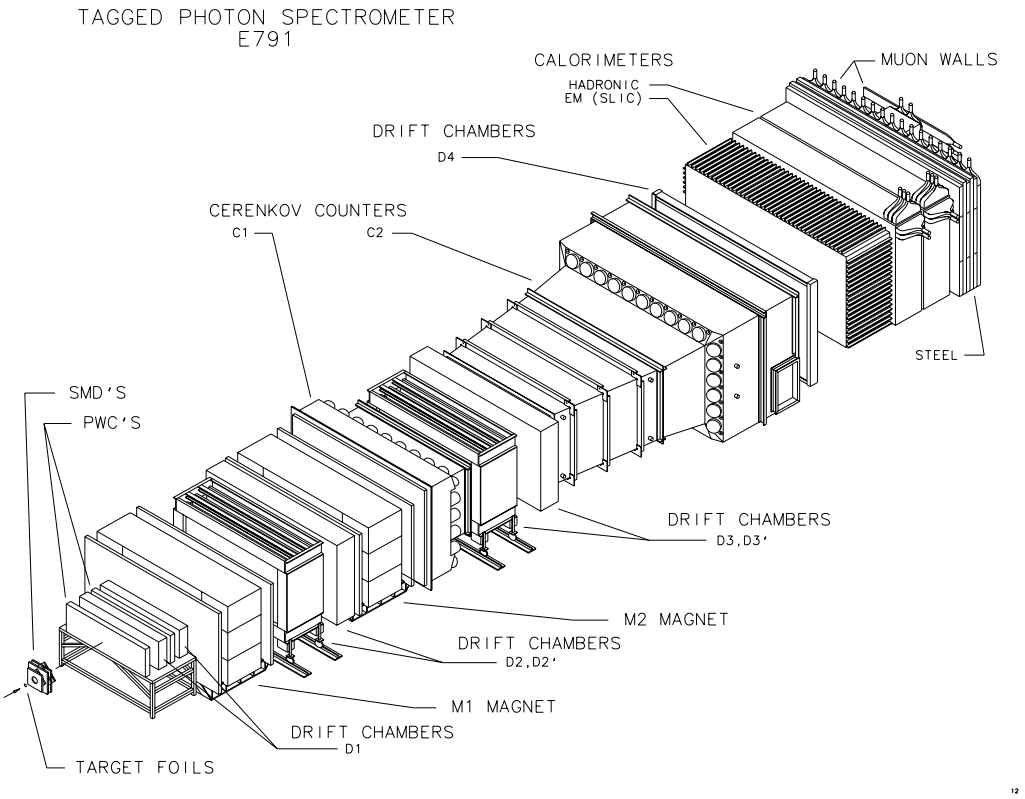

Figure 4.1: A view of the spectrometer. At this level of detail, the Fermilab E791 and E769 spectrometers were identical.

isochronous self-collimating Cerenkov counter. It was used to identify kaons in the beam. A transition radiation detector (TRD) followed the DISC. The TRD was used to discriminate pions from kaons and protons during the positive beam running. There were also silicon microstrip detectors and proportional wire chambers to measure the position and direction of the beam. All these components were upstream of the target.

There were three types of components used to measure the positions of the tracks of charged particles downstream of the target. These were the PWC's (proportional wire chambers), drift chambers (four groups of them labeled D1, D2, D3, and D4), and the silicon microstrip detectors (SMD's). By measuring the bend in tracks created by two large magnets, these tracking chambers also measured the momentum of

Detector Component	Z coordinate of center (cm)	Active Area (cm x cm)	Resolution
DISC	-4000		
TRD	-3500		
PWC Beam 1 (X, Y, X', W)	-3155		300 μm
PWC Beam 2 (X, Y, X', W)	-1224		300 μm
Beam Spot Scintillator	-19	2.5 x 2.5	
SMDA (Y, X)	-17	1.0 x 1.0	9 μm
1st Target Foil	-5.0	2.5 x 2.5	
Last Target Foil	-1.0	2.5 x 2.5	
Interaction Scintillator	-0.38	3.5 x 3.5	
SMDB (Y, X)	0.4	2.5 x 2.5	9 μm
SMD1 (X, Y, V)	3.8	2.6 x 2.6	16 μm
SMD2 (Y, X, V)	12.4	3.8 x 3.8	16 μm
SMD3 (X, Y, V)	21.3	5.0 x 5.0	16 μm
PWC1 (Y)	130	57.6 x 57.6	300 μm
D1-A (U, V, X, X')	156	86 x 65	350 μm
PWC2 (Y)	175	57.6 x 57.6	300 μm
D1-B (U, V, X, X')	192	114 x 65	350 μm
Magnet 1	286	174 x 86	$\frac{\Delta p}{p} \sim 0.1\% p$
D2-1 (U, X, V)	384	182 x 130	300 μm
D2-2 (U, X, V)	426	182 x 130	300 μm
D2-3 (U, X, V)	468	210 x 130	300 μm
D2-4 (U, X, V)	499	228 x 130	300 μm
Magnet 2	621	171 x 88	$\frac{\Delta p}{p} \sim 0.05\% p$
Cerenkov 1 Mirror plane	866	250 x 130	
D3-1 (U, X, V)	930	254 x 130	350 μm
D3-2 (U, X, V)	972	254 x 130	350 μm
D3-3 (U, X, V)	1014	254 x 130	350 μm
D3-4 (U, X, V)	1046	302 x 130	350 μm
Cerenkov 2 Mirror plane	1653	465 x 240	
D4 (U, X, V)	1744	508 x 240	800 μm
EM Calorimeter	1900	490 x 240	$\frac{\Delta E}{E} \sim \frac{21\%}{\sqrt{E}}$
Hadronic Calorimeter	1956	490 x 270	$\frac{\Delta E}{E} \sim \frac{75\%}{\sqrt{E}}$
Muon Wall	2235	547 x 305	

Table 4.1: Summary of the positions, sizes, and resolutions of the detector components. Information comes from Table 4.4 of [49] and from [50]. Measured resolutions from Ref. [51] are a little higher than those shown here.

tracks. There was an electromagnetic (EM) calorimeter and an hadronic calorimeter near the end of the detector. The calorimeters were used to measure the total transverse energy in each event. The rest of this chapter describes each of these components in more detail. It also discusses the beam, the scintillator detectors, the trigger, and the data acquisition system.

There were several components of the detector that were not used in this analysis. These include the downstream Cerenkov detectors, the kaon wall, the muon wall, and the TRD (transition radiation detector). Since they are not relevant, these will not be mentioned again.

The information in this chapter comes from references [49, 50, 51, 52, 53, 54].

4.1 The Accelerator

Figure 4.2 shows the path of the beam. The beam started at a very small ion source where hydrogen gas was passed over cesium to turn it into H^- ions. The ions were accelerated in a Cockcroft-Walton accelerator to a kinetic energy of about 750 KeV. The Cockcroft-Walton is an electrostatic accelerator. The current of the beam was between 50 and 60 mA at that point. This beam was injected into a linear accelerator (LINAC) where it traveled down a series of long straight chambers. An RF field accelerated the beam to an energy of 200 MeV. The frequency of the RF field was 201 MHz. The beam was carrying 35 to 40 mA. The beam was passed through a carbon foil to strip the electrons from the ions, turning them into protons. It was then injected into the booster ring. The booster ring accelerated the beam to 8 GeV. In the booster, the beam was accelerated by an RF field that varied between 38 and 51.8 MHz as the energy of the beam increased.

The largest tunnel ring on site contained two accelerator rings, one on top of the other. One was called the Main Ring and the other was called the Tevatron. The booster injected the beam into the Main Ring. The Main Ring accelerated the

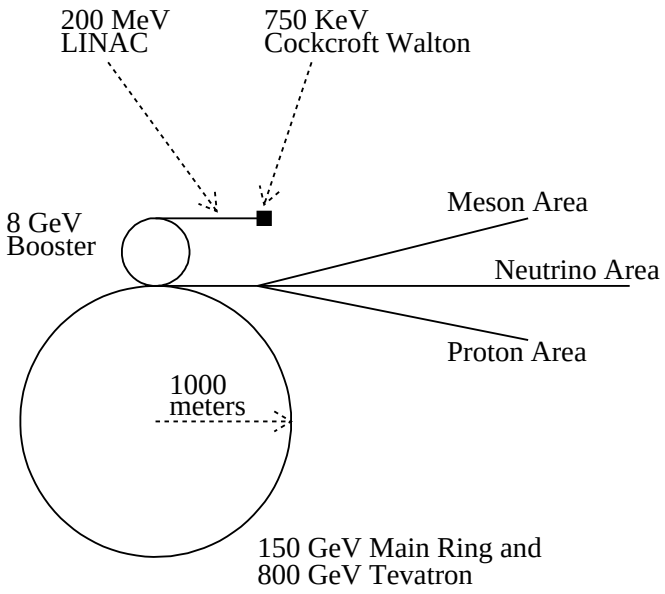

Figure 4.2: A view of the accelerator and fixed target areas. The components in this figure are not drawn to scale.

beam to about 150 GeV. Then it was injected into the Tevatron, which accelerated the beam to 800 GeV. All three rings were synchrotrons. In the booster ring and Main Ring, conventional iron core magnets were used to bend the beam into a circular orbit. In the Tevatron, superconducting magnets were used to get a stronger magnetic field. These magnets were cooled by liquid helium.

In the Main Ring and Tevatron, the beam was accelerated using 53 MHz RF fields. These fields gave the beam a bunch structure with a period of 19 ns. Every 19 ns, there were protons grouped together in what was called a bucket. A bucket was roughly 2 ns long and there were no beam particles between buckets.

Every minute, there was a period of about 22 seconds where beam particles were extracted from the Tevatron and sent toward the fixed target areas. The particles extracted in this 22 second interval formed a spill. After leaving the Tevatron,

the beam was split into three separate beams that went to the Proton Area, the Neutrino Area, and the Meson Area. Each of these three beams was split again to go to different fixed target detectors. The TPS used by E769 was in the Proton East Area at Fermilab. A spill contained roughly 10^{13} protons. Usually, between 10^{11} and 10^{12} of those were sent to the Proton East area.

At the Proton East area, the beam struck a 30 cm long beryllium target. There were magnets and collimators after this target that selected negative particles produced in the beryllium with a momentum of 250 GeV/c. These particles formed a beam of 250 GeV/c π^-'s, antiprotons, and K^-'s. This 250 GeV/c beam was then directed at the main target of the experiment. The spectrometer was used to study interactions between the 250 GeV/c beam and the target. This negative beam had an average flux of about 0.5 x 10^6 particles per second, although the instantaneous flux varied widely. There was also a period of time when a positive beam impacted on the target, but data from this period was not used in this analysis.

4.2 Beam Identification

The first detector element the beam hit was the DISC. The DISC identified kaons based upon Cerenkov radiation. A particle moving faster than the speed of light in a material emits Cerenkov radiation peaked in a cone at an angle θ_c centered on the direction of motion. The angle is determined by the relation

$$\cos\theta_c = \frac{1}{\beta \mathrm{n}} \ ,$$

where β is the velocity of the particle and n is the index of refraction of the material. The DISC contained mirrors, lenses, and slits that directed light emitted at an angle of 24.5 mrad onto a set of photomultiplier tubes. Light emitted at other angles would not hit the phototubes. The DISC was filled with helium and the pressure could be controlled. Since the index of refraction depends on the pressure, the index of refraction could be controlled. During most of the negative beam run, the pressure

Beam Particle	Raw	After Removal of DISC tagged K^-
π^-	93 %	95 %
K^-	5 %	3 %
$\overline{p}$	1.5 %	2 %

Table 4.2: Measured negative beam composition [39].

was set so that K^- beam particles emitted radiation at 24.5 mrad. The masses of the π^- and antiproton are different, so particles having the same momentum have a different β and do not emit radiation at 24.5 mrad. If a beam particle caused a response in the phototubes over a set threshold, then the particle was tagged as a K^- in the final dataset and the information was passed to the trigger.

During test runs, the pressure of the DISC was swept over a large range. Each different beam particle emits radiation at 24.5 mrad at different pressures. By studying the response as a function of pressure, one can measure the fraction of each type of particle in the beam. Table 4.2 shows the composition of the beam measured using the DISC.

4.3 The Minimum Bias Trigger

Only about 1 in 100 buckets contained a beam particle in the negative beam running, and it was pretty random as to which did and which did not. Most beam particles did not interact in the target. A series of scintillation counters was used to determine when a beam particle interacted in the target. Figure 4.3 shows some of these scintillation counters. The line in the figure represents the beam which travels from left to right. It first strikes the beam spot scintillator and then passes through the beam halo scintillator. The cube represents the target assembly which will be discussed in the next section. To the right of the cube is the interaction scintillator. Out of the figure, very far to the left (roughly 35 meters upstream), there are two more scintillators similar to the beam spot scintillator. If there is a signal from

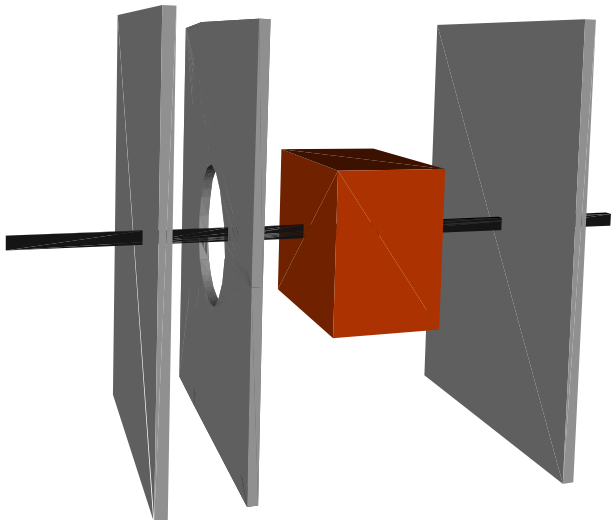

Figure 4.3: A view of the scintillation counters near the target used in the minimum bias trigger [50]. The components in this figure are not drawn to scale.

these two scintillators and the beam spot scintillator at the same time (allowing for the time of flight of the beam particle), then that signals a beam particle. The experiment was only interested in beam particles that hit near the center of the target. The beam halo counter has a hole of radius 9.5 mm near its center. If there was a signal from the beam halo scintillator the event was vetoed and no data recorded.

If the beam particle interacted inelastically in the target, then many new particles would exit the target volume. The interaction scintillator had a threshold that required at least the light produced by five minimum ionizing particles be detected. If the signal was above the threshhold, then there was an interaction in the target. Otherwise, it was assumed there was no interaction. In summary, the minimum bias trigger required a coincidence of three scintillators with a signal, the beam halo with no signal, and the interaction scintillator with a signal produced by five or more particles.

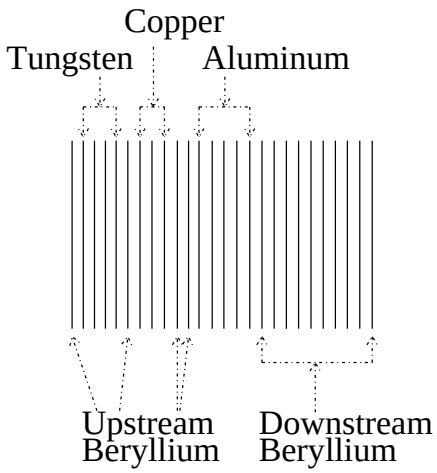

Figure 4.4: The target assembly. The figure shows the actual size and separation of the target foils. Only the thickness is not to scale. As shown by the arrows, foils 1, 6, 10, 11, and 17 to 26 are beryllium. Foils 2 to 5 are tungsten. Foils 7 to 9 are copper. Foils 12 to 16 are aluminum. This is a view from the side. The beam would travel from left to right in this figure.

4.4 The Target

The target was composed of 26 foils as shown in Figure 4.4. Each foil was a square with dimensions 2.5 cm x 2.5 cm. The assembly that contained them extended over a range of 4 cm. The thickness of the foils ranged from 94 to 276 μm. The average separation between the foils was approximately 1.37 mm. A beam particle traversing the target region went through about 2% of an interaction length of material.

The reason that there are 26 thin closely spaced foils is related to charm physics. In charm studies, one looks for two closely spaced vertices: the primary vertex and the vertex from charm decay (a vertex is a point where charged tracks intersect). The designers of the target believed one could identify the foil of primary interaction. The reconstructed position of the primary vertex would be corrected to lie in the nearest foil. This would reduce the error on its position. Unfortunately, the error on the position of the vertices was too large and this did not work. In fact, it took some care to determine the material of the primary interaction. This is discussed in

detail in a later chapter.

The order of chambers is significant. The tungsten foils are farther upstream. When the primary interaction occurs in the tungsten foils, the secondary particles have to travel through all the other target foils. Sometimes they interact again and this increases the multiplicity (total number of charged particles) in the event. The multiplicity affects the acceptance. This is discussed in detail in a later chapter.

4.5 Silicon Microstrip Detectors

The positions of the elements of the downstream silicon microstrip detector (SMD) are shown in Table 4.3. They are all located within 25 cm of the target. They are designed to give precise tracking near the target. The precision is needed to determine the location of the primary vertex and any secondary vertices formed by charm particle decay. In this analysis, secondary vertices from charm decays are not a concern, but the location of the primary vertex is important. It gives the material where the primary interaction occurred.

In the table, the view is the direction of the measurement. X means horizontal, Y means vertical, and V refers to a direction rotated 20.5 degrees from the X axis. The strips are oriented perpendicular to the direction of measurement. The pitch is the distance between the centers of adjacent strips. The resolution on hit position measured from the data is about 21 μm for the 50 μm pitch strips [51].

The SMD planes are constructed from silicon wafers about 300 μm thick. Arsenic is implanted into one side of the wafer to form a thin n-type layer. An aluminum coating is deposited over the n-type layer. This side of the wafer is connected to ground through a voltage source of about 90 volts. A positive voltage (reverse bias) is applied to draw electrons out of the n-type material. The other side of the material has strips where boron is implanted in the wafer to form p-type material. These strips are coated with aluminum electrodes that are attached through preamplifiers

Z Coordinate (cm)	View	Pitch (μm)	Instrumented Channels
0.202	Y	25	386
		50	304
0.605	X	25	386
		50	304
1.931	X	50	512
2.934	Y	50	512
6.658	V	50	512
10.977	Y	50	768
11.328	X	50	768
14.937	V	50	768
19.853	X	50	1000
20.202	Y	50	1000
23.825	V	50	1000

Table 4.3: Positions of the downstream Silicon Microstrip Detectors [50].

to the data acquisition system.

Semiconductors have electron energy levels with bands and with gaps between the bands. The highest populated band (the valence band) is nearly full and does not conduct much electricity. The next higher band (the conduction band) is nearly empty and also does not conduct much. Doping the faces of the wafer and applying a reverse bias potential almost completely depletes the few charge carriers in the wafer. Very little current normally flows through the wafer. Charged particles passing through the wafer excite the electrons in the silicon wafer and create electron-hole pairs. This causes a current to flow to the preamplifiers. The low energy gap between the valence and conduction bands is the reason silicon is used. Because the gap is so small (3.6 eV), 20,000 to 30,000 electron-hole pairs are created when a minimum ionizing particle passes through the wafer.

4.6 Drift Chambers and Proportional Wire Chambers

The drift chambers are particularly important in this analysis. The results of the analysis are based on detection of Ξ^-'s that decayed downstream of the SMD. The tracks of the decay products of the Ξ^-'s are located using only the drift chambers. The drift chambers are also used to measure the momentum of the particles.

There were 35 drift chamber planes downstream of the target. Table 4.4 shows the position and some performance characteristics of those planes. There were four groups of chambers labeled D1, D2, D3, and D4. The D1 planes were located upstream of the first magnet. There were two subassemblies of four planes each in D1. The four planes in each subassembly measured position in the U, V, X, and X' directions. The U and V directions are offset ± 20.5 degrees from the X direction. The X and X' views are in the same direction, but the sense wires were offset by half a cell width. D2, D3, and D4 all contained subassemblies which had three planes each. These three planes were oriented in the U, X, and V directions. D2 was located between the first and second magnets and had four subassemblies. D3 and D4 were located after the second magnet. D3 had four subassemblies. D4 was very far downstream and had one subassembly. The sense wires were oriented perpendicular to the direction of measurement. The multiple views allowed a measurement of the X and Y coordinates at each assembly.

The drift chambers detected charged particles using the trail of ionization left when the particles traversed the gas in the chambers. The gas was a 50/50 argon-ethane mixture with about 1% ethanol added. The gas was contained in boxes that contained several wire planes. There were alternating sense wire planes and high voltage planes. The high voltage planes were typically held at -2.4 kV. Electrons ionized in the gas would drift toward the sense wire planes. In the sense wire plane, there were two types of wires. Every other wire was a field shaping wire held

	Assembly and View	Z (cm)	Sense Wire Separation (cm)	Number of Sense Wires	Efficiency	Resolution (μm)
1	D1-1U	153.6	0.4763	192	0.925	390
2	D1-1V	154.6	0.4763	192	0.925	380
3	D1-1X	158.7	0.4461	192	0.910	390
4	D1-1X'	159.6	0.4461	96	0.908	390
5	D1-2U	188.7	0.4763	256	0.918	440
6	D1-2V	189.7	0.4763	256	0.927	400
7	D1-2X	193.8	0.4461	256	0.890	450
8	D1-2X'	194.7	0.4461	96	0.854	430
9	D2-1U	382.4	0.8922	176	0.828	340
10	D2-1X	384.0	0.9525	192	0.874	310
11	D2-1V	385.5	0.8922	176	0.899	350
12	D2-2U	424.9	0.8922	176	0.831	370
13	D2-2X	426.5	0.9525	192	0.782	350
14	D2-2V	428.1	0.8922	176	0.776	360
15	D2-3U	466.6	0.8922	208	0.799	370
16	D2-3X	468.2	0.9525	224	0.850	350
17	D2-3V	469.8	0.8922	208	0.826	380
18	D2-4U	497.7	0.8922	208	0.906	330
19	D2-4X	499.3	0.9525	240	0.879	350
20	D2-4V	500.9	0.8922	208	0.916	350
21	D3-1U	928.3	1.4870	160	0.872	310
22	D3-1X	929.9	1.5875	160	0.869	330
23	D3-1V	931.5	1.4870	160	0.876	320
24	D3-2U	970.8	1.4870	160	0.890	300
25	D3-2X	972.4	1.5875	160	0.886	290
26	D3-2V	974.0	1.4870	160	0.862	300
27	D3-3U	1012	1.4870	160	0.765	360
28	D3-3X	1014	1.5875	160	0.887	360
29	D3-3V	1016	1.4870	160	0.906	410
30	D3-4U	1044	1.4870	160	0.924	280
31	D3-4X	1046	1.5875	192	0.864	280
32	D3-4V	1048	1.4870	160	0.900	330
33	D4U	1738	2.974	128	0.701	1190
34	D4X	1744	3.175	160	0.681	1220
35	D4V	1749	2.974	128	0.684	1180

Table 4.4: Drift chamber plane configuration and performance. The efficiency and resolutions were measured using data [51].

at typically -2.0 kV. The other wires were the sense wires. The electric field was designed so that ionized electrons drifted at a near constant rate towards the sense wire. By measuring the time between the passage of the charged particle and the arrival of the electrons at the sense wire, one could estimate the distance between the sense wire and the charged track. The drift velocity in these tubes was of order 50 μm per nanosecond.

Near the center of the drift chamber planes, there was an area called the drift chamber hole. This area had been damaged in earlier experimental runs by the high flux of particles in and near the beam. In the hole, the efficiency of the chambers was much lower.

There were also two proportional wire chambers near the D1 drift chambers. These worked on a similar principle, except there was no effort to measure the drift time or distance. Position was simply approximated to be at the nearest sense wire.

4.7 Magnets

The drift chambers were used to measure the change in direction of tracks of charged particles as they passed through two large magnets. The momentum could be calculated directly from the change in direction. The change in angle is

$$\Delta\theta = \Delta p_T / p \ ,$$

where $\Delta\theta$ is the change in direction of the track, Δp_T is the change in transverse momentum, and p is the total momentum. The change in tranverse momentum is

$$\Delta p_T = q \int B_y dl \ ,$$

where B_y is the magnetic field strength and dl is a small distance along the path of the particle. $\Delta p_T = 213$ MeV/c for the first magnet and $\Delta p_T = 321$ MeV/c for the second magnet. Actually, the equation above is an approximation. It would be more accurate to put the equation in vector form, given the large size of the magnets.

The resolution was [49]

$$\frac{\sigma_p}{p} = \sqrt{(0.1\%p)^2 + (0.5\%)^2} \text{ (first magnet)} ,$$

$$\frac{\sigma_p}{p} = \sqrt{(0.05\%p)^2 + (0.5\%)^2} \text{ (two magnets)} ,$$

where p is in GeV/c. The first term in the expressions relates to error on the measurement of $\Delta\theta$. The second relates to multiple scattering. The error on the momentum measurement was the dominant error on the measurement of the Ξ^- mass and determined the width of the peak in the Ξ^- mass distribution.

4.8 Calorimeters

The electromagnetic calorimeter had 60 layers. Each layer contained a 0.37 cm lead radiator and a 1.27 cm liquid scintillator. A particle traveling through it passed through 20 radiation lengths and 1.5 absorption lengths of material. The scintillator was in channels that were 3.2 cm wide so that one could measure the position of showers. The channels were oriented in different directions in different layers. One could measure in U, V, and Y directions. The aperture was ± 66 mrad in the vertical direction and ± 133 mrad in the horizontal direction. The energy resolution was

$$\frac{\Delta E}{E} = \frac{21\%}{\sqrt{E}} .$$

More information on the electromagnetic calorimeter can be found in [55, 56].

The hadronic calorimeter had 36 layers. Each layer contained a 2.54 cm steel radiator and a 0.95 cm plastic scintillator. The scintillators were in strips 14.3 cm wide that were alternately in X and Y directions. The hadronic calorimeter was 6 absorption lengths deep. The energy resolution was

$$\frac{\Delta E}{E} = \frac{75\%}{\sqrt{E}} .$$

More information on the hadronic calorimeter can be found in [57].

In this analysis, the calorimeters were only used for the ET trigger. The ET trigger enriched the data for charm physics studies, but created problems for Ξ^- studies. The method of combining the results from the ET trigger and the minimum bias trigger will be described later. The end result is that the calorimeters have no effect on the physics results other than to substantially increase the statistical errors.

4.9 Data Acquisition

The data acquisition for Fermilab E769 was significantly improved compared to its predecessor at TPS, Fermilab E691. The rate of data acquisition was increased by a factor of 10.

The drift chambers, SMD's, and other detector components generated data in roughly 20,000 channels. They sent their data to 7 CAMAC (Computer Automated Measurement and Control [58]) crates for digitization. Although one CAMAC crate was added for E769, the others were the same as used in E691. The information in the CAMAC crates was read out in parallel into several 32 kByte buffers in a VME crate. In E691, the readout was serial. Parallel readout increased the speed of the system by a factor of 5. The modules responsible for reading out the data were new and twice as fast as the E691 modules. The information in the buffers was copied into the memory of ACP (Fermilab's Advanced Computer Projects) processors. There were 17 ACP processors that processed events in parallel. The data acquistion system could process 1.8 Mbytes/sec (450 events/second). The dead time of the system was approximately 25%. During the spill and time between spills, the event records were copied from ACP memory to tape by one of three available 6250 bpi, 100 ips, STC 2925 tape drives. The numbers in this section come from Ref. [49]. Also see Ref. [59] and Ref. [60] for a more detailed description of the data acquisition system.

Chapter 5

Preliminary Data Analysis

This chapter describes the first few stages of the data analysis: event reconstruction, the Ξ^- strip, and weeding. Event reconstruction was complete before I started working in the Fermilab E769 collaboration. My work started with the Λ strip and Ξ^- strip.

5.1 Reconstruction

Reconstruction was a major task; it took the collaboration years to prepare the software and then another year to process the data. The original data reconstruction was run on a farm of processors offline. The farm consisted of a combination of 16 dedicated Silicon Graphics processors and a pool of ACP processors. The ACP processors were shared with other experiments at Fermilab. This multiprocessor system was run in parallel using the CPS software system to manage all the processes and I/O. The reconstructed information was written to 8 mm data summary tapes (DST's), and these tapes were used for subsequent analysis. See Ref. [61] for a detailed description of the software and hardware used to reconstruct the data.

The reconstruction performed many tasks. Tracks were created from hits, calorimeter information was converted to shower locations, particle identification was per-

formed, vertices were found, the data format was compressed, and many other tasks were performed. Actually, the only reconstruction task critical for this analysis is the track reconstruction. The calorimeter, muon, and downstream Cerenkov information is not used in this analysis. The vertex positions are recalculated later.

Tracking started in the silicon microstrip detector (SMD). Tracks found in the silicon were extrapolated to the drift chambers. Hits associated with these tracks were marked as used. These tracks were used to find the primary vertex. They were also used to look for charm signals. After the SMD tracking was complete, tracks were formed from the unused hits in the drift chambers. The drift chamber tracks were used in this analysis to reconstruct Ξ^-'s.

5.2 Ξ^- Strip

A strip is a selection of events. A strip is made to reduce the size of a dataset, but retain most of the events of interest. The criteria used in the selection are commonly called cuts. The cuts used to make a strip are looser than the final analysis cuts. The Ξ^- strip was created in two stages. In the first stage, events with tracks resembling the decay products of a Λ were selected. This was called the Λ strip. Then the Ξ^- strip was made using the Λ strip as input.

Events were selected from region 2 of the experimental run. Region 2 contained only 250 GeV/c negative beam data. Events were selected from tapes created in the original reconstruction. E769 "rereconstructed" pair strip tapes were not used.

132,028,566 events were examined in the search for Ξ^-'s. Ref. [3] contains a list of the data summary tapes (DST's). The search included 266 8mm tapes, more than 95% of the 250 GeV/c negative beam data. Λ candidate events were selected from these tapes and written to 14 new tapes (the Λ strip). These tapes contained 12,735,294 candidate Λ events. In turn, Ξ^- candidate events were selected from the Λ strip and written to 1 tape containing 678,731 candidate Ξ^- events.

5.3 Weeding

The Ξ^- strip contains duplicate events and bad events. Both types of events were removed (weeded) from the final dataset. Two Ξ^- candidates were considered duplicates if they had the same run number, logical record number, and Ξ^- mass. Approximately 2.2% of the Ξ^- candidates were duplicates. Bad events are on the bad PASS0 list. The bad PASS0 list was formulated for charm studies based on several factors. A tape was put on the bad PASS0 list if [51]:

1. Less than 90% of the events on the tape were reconstructible
2. Greater than 10% of the events had too many SMD hits
3. Greater than 6% of the events had too many fatal drift chamber unpacking problems
4. Average E_T of events was greater than 9 GeV

The PASS0 list is based on studies that did not include the entire dataset, but only about 60% of it. In addition, runs 1258, 1259, 1402, and 1403 were identified as bad in the study described in the next paragraph. Approximately 1.5% of the Ξ^- candidates were weeded because they were from bad tapes or runs.

Concurrent with making the Λ strip, a few elements of the data from all minimum bias trigger events were put into ntuples. Several histograms of different quantities versus run were made from the minimum bias trigger ntuples: the fraction of events where no tracks were reconstructed, the average number of reconstructed tracks, the average number of reconstructed tracks with silicon detector hits, the average of the total reconstructed track transverse momentum, the ratio of tungsten events to beryllium events, and the fraction of minimum bias events passing the transverse energy triggger requirement. Two of these are shown in Figures 5.1 and 5.2. Four additional bad runs were identified from the histograms and removed from the dataset.

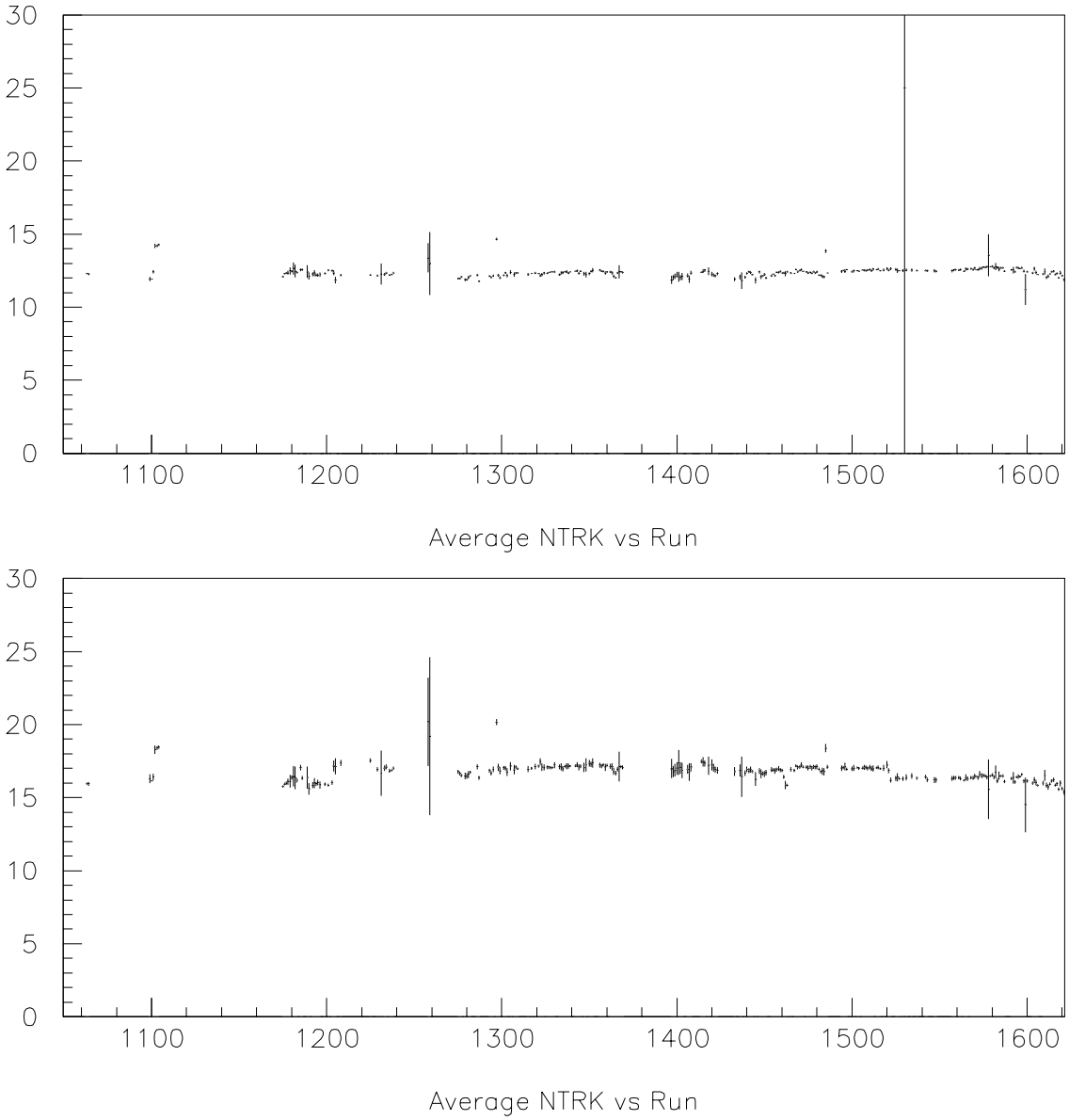

Figure 5.1: These histograms show the average value of NTRK (number of reconstructed tracks in an event) versus run number. Events with NTRK = 0 are excluded from the average. Both histograms are made from the ntuple of all minimum bias trigger events. The top plot is made from all the events in the ntuple. The bottom plot is made using only events that also pass the trigger transverse energy requirement (no requirement for the prescaler).

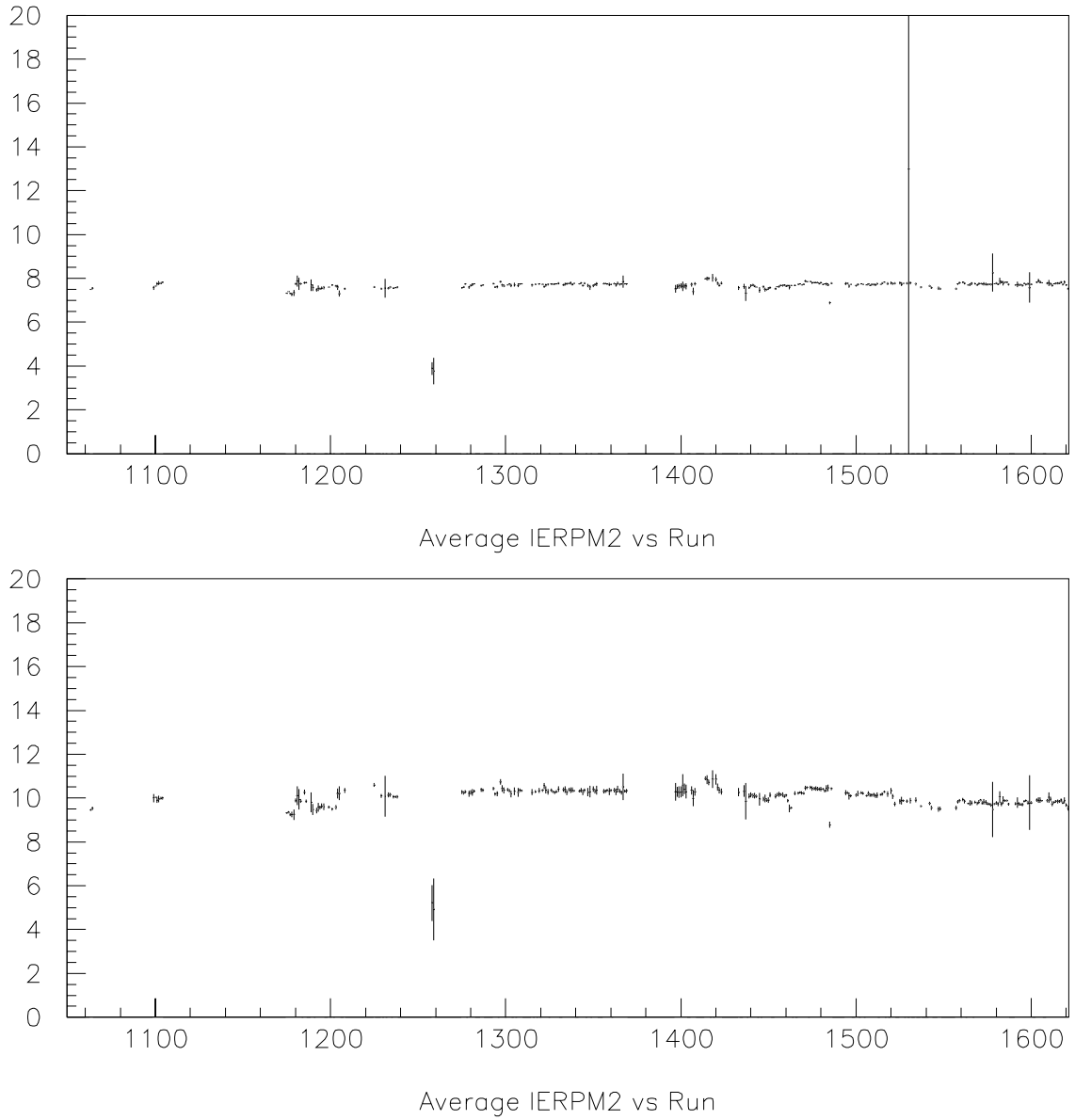

Figure 5.2: These histograms show the average value of IERPM2 (number of reconstructed tracks with silicon detector hits) versus run number. Events with NTRK = 0 are excluded from the average. Both histograms are made from the ntuple of all minimum bias trigger events. The top plot is made from all the events in the ntuple. The bottom plot is made using only events that also pass the trigger transverse energy requirement (no requirement for the prescaler). Runs 1258 and 1259 were weeded out based on these plots.

Chapter 6

Deriving the Data Signals

This chapter describes the analysis steps necessary to calculate the raw data signal for each target material. Acceptance corrections and the presentation of the results are the subjects of later chapters.

6.1 Triggers

This analysis used data from two triggers: the minimum bias trigger and the ET trigger. The scintillators in the minimum bias trigger were described in Section 4.3. In addition, this trigger included a prescaler that randomly passed a fraction of events to control the data rate. The prescaler was typically set at roughly 100 or 200 (1 out of 100 or 200 events passed). The ET trigger included all the requirements of the minimum bias trigger, except the ET trigger had a separate prescaler (typically set near 5 or 10). The ET trigger also had a requirement that 5.5 GeV of tranverse energy be detected in the calorimeter.

There were other triggers in the experiment: a trigger with a higher transverse energy requirement, a kaon trigger, and an electron trigger. These were not used for this analysis and will not be mentioned again in this document.

Data events from the two triggers are used together. The events are given dif-

ferent weights to get the correct answer. The ET trigger events are given a weight of 1.0. The minimum bias trigger events with less than 5.5 GeV of tranverse energy (measured online for the trigger) are given a

$$\text{weight} = \frac{\text{minimum bias prescaler}}{\text{ET trigger prescaler}} \ .$$

To determine a signal, one sums the weights. To determine the Poisson error on the signal, one sums the weights in quadrature. The weights on the minimum bias events with less than 5.5 GeV are typically around 20. There are more than 20 times more ET trigger events, so the ET trigger events contribute more to the totals. But because the weights are added in quadrature, the minimum bias events with less than 5.5 GeV dominate the statistical error.

A few runs are weighted differently. For most runs the ratio of prescalers is about 20, but for some runs it is significantly higher. It would be undesirable to give events very large weights. Then statistical fluctuations in these runs could affect the result. There are 13 runs where the ratio of prescalers is greater than 25. All the events in these runs are given an additional weighting factor. The additional weighting factor is either 0.2, 0.25, or 0.5. It is selected so that no event gets a weight greater than 25. It is important that this additional weighting factor multiplies the weight for all events in these runs, both ET and minimum bias events. The ratio between the weights given the ET events and the minimum bias events remains constant.

There is a second exception to the formula given above. There are a few runs where nearly all the events are minimum bias trigger events. In these cases, the weighted combination does not make sense. For these runs, all the minimum bias trigger events are used. They are all given the same weight, ignoring the ET transverse energy requirement. The weight for events in these runs is 8.0. This is a value between 1.0 and 20.0, where 1.0 is a typical weight for events that pass the tranverse energy requirement and 20.0 is a typical weight for events failing the transverse energy requirement. Runs 1100, 1183, and 1516 were minimum bias trigger runs.

The prescalers used in the weights are calculated from the data. A set of minimum bias trigger events is used to calculate the ET prescaler for each run. A set of ET trigger events is used to calculate the minimum bias prescaler for each run.

6.2 The Primary Vertex

6.2.1 The Method for Determining the Primary Vertex

The primary vertex location is critical to this analysis. Each Ξ^- is assumed to be produced in the target foil nearest the primary vertex. The vertex position is calculated using a modified version of the algorithm used in the original event reconstruction. The algorithm goes through a complex series of steps to select a set of tracks with SMD hits that all come close to a common point. A χ^2 fit is performed to determine the location of the primary vertex.

The original vertex algorithm is modified, because it was tuned to resolve two closely spaced vertices characteristic of charm particle decay. The Ξ^- has a much longer lifetime, and does not usually produce two closely spaced decay vertices. The modifications are as follows:

1. The χ^2 cut for vertices is modified. The cut for the first two tracks in a vertex was 2.0 and is now 2.5. For additional tracks, the cut was 2.0. Now the cut ranges from 2.5 to 1.5. It gets tighter with each added track.

2. The cuts on track quality are loosened. The cut on the χ^2 of the track is loosened from 5.0 to 6.0. The cut on the number of degrees of freedom is loosened from 2 to 1. The cut requiring drift chamber hits beyond the first magnet is eliminated.

3. If the pion from the Ξ^- decay has an SMD track, that track is excluded from the primary vertex.

4. If an SMD track is found for the Ξ^-, it is forced to be in the vertex.

5. The primary vertex is still the vertex with the most tracks, but there is a slight modification when more than one vertex has the same number of tracks. The tiebreaker in the past was the more upstream vertex was selected. Here, if one vertex has a χ^2 worse than 1.8 and the difference between the χ^2 of the vertices is more than 0.4, then the vertex with the lower χ^2 is selected as the primary. Otherwise, the most upstream vertex is selected.

6. If the new algorithm fails to find a primary vertex, the primary vertex from the original reconstruction is used.

The modifications and parameters described above were determined using simulation ("monte carlo") studies. These studies make use of information saved from the event generation process ("truth table" information). It is compared to information reconstructed using the data reconstruction codes. In one study, it was found that:

- For the vertex from the original reconstruction, $95.3\% \pm 0.2\%$ were assigned the correct material, and $4.7\% \pm 0.2\%$ were assigned the wrong material type.

- For the vertex derived for this analysis, $96.3\% \pm 0.2\%$ were assigned the correct material, and $3.7\% \pm 0.2\%$ were assigned the wrong material.

- The new method finds a vertex 3.1% more often than the original method. Of the 3.1%, 2.6% are in the correct material; 0.5% are not.

Another study compares the z coordinates of the primary vertex from the two methods with the truth table z coordinate and with each other (see Figure 6.1). These studies show that the new method of finding the primary vertex is better than the old method.

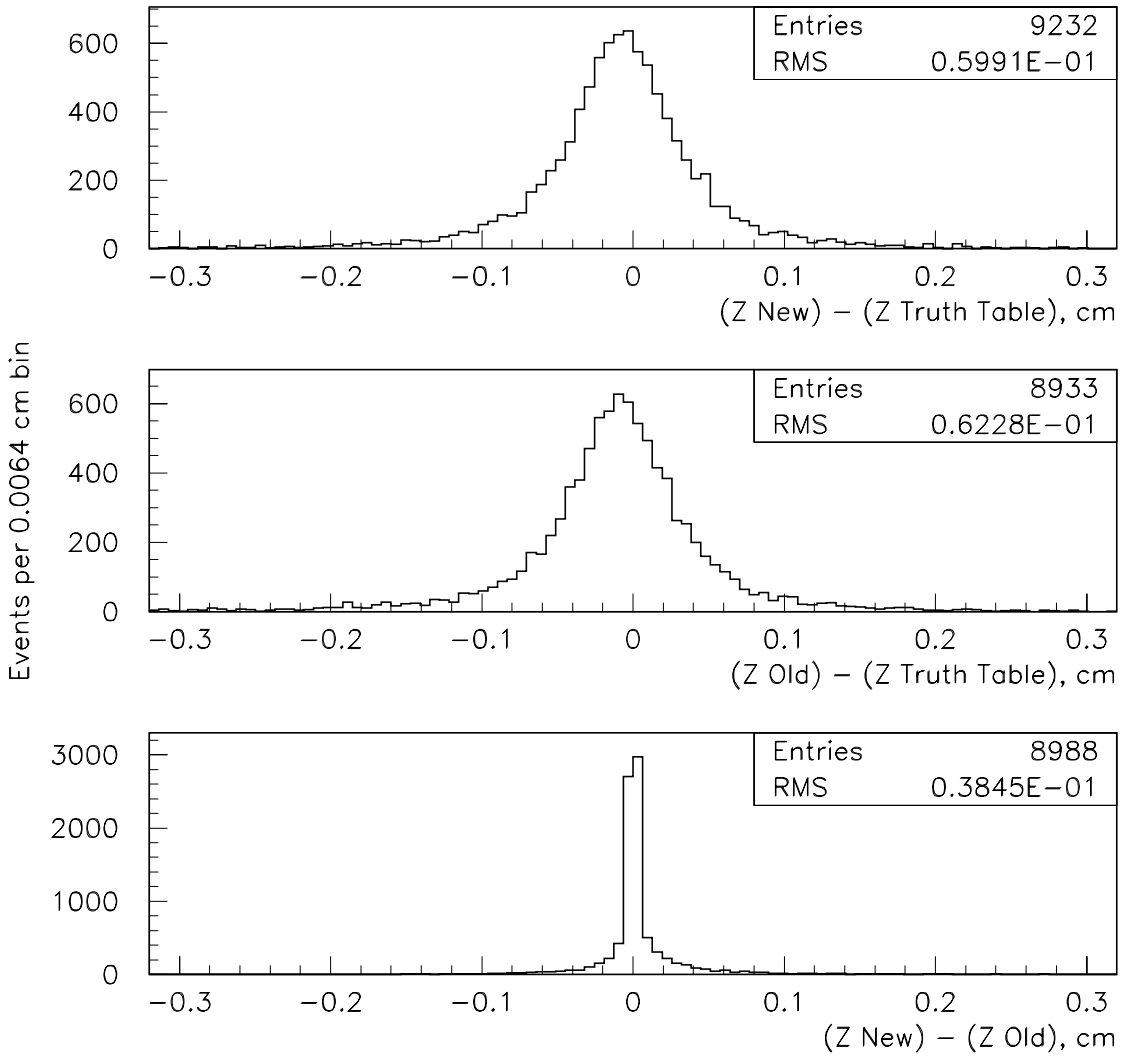

Figure 6.1: Primary vertex Z coordinate errors in the simulation. All three plots show the distribution of the difference between Z coordinates of different vertex locations. The top plot is the difference between the truth table and the new vertex algorithm used in this analysis. The middle plot is the difference between the truth table and the old vertex algorithm used in the original reconstruction. The last plot shows the difference for the two reconstruction algorithms. These plots are made from events that pass the analysis cuts, except the cut on the impact parameter to the primary vertex divided by the distance traveled by the Ξ^-. There are additional cuts. The primary must be in the target region. In all three cases, the difference must be less than 0.32 cm (average separation between foils is 0.16 cm). In the top plot the number of entries is higher. More events pass the 0.32 cm cut. The RMS value is smaller in the top plot.

6.2.2 Systematic Errors Related to the Primary Vertex

On the following page, Table 6.1 compares the numbers of events in each material for truth table vertices and reconstructed vertices. The number shifts by as much as 5% due to errors on the z coordinate of primary vertices. The copper and tungsten signals decrease roughly 4% or 5%. The aluminum and beryllium signals stay relatively constant. Physically, this is plausible. Losses are less for materials that have consecutive foils spread out over a larger distance (see Figure 4.4). Contamination depends on the number, thickness, and density of adjacent foils. Vertex errors are substantially larger for foils farther from the SMD. These trends are automatically modeled in the acceptances measured using the simulation. Vertex position errors cause the acceptances for beryllium and aluminum to be higher than the acceptances for copper and tungsten.

Two quick conclusions can be drawn from Table 6.1. First, the contamination in the upstream beryllium foils is near 34%, too high to be useful. Events with a primary vertex assigned to these target foils are not used in the calculation of the atomic mass dependence of the Ξ^- cross section. Only the downstream beryllium foils are used. Second, only 5 events that were generated outside the target foils passed the cuts and had a vertex assigned to a target foil. The events from interactions outside the target are a negligible part of the signal.

One might think there would be a systematic error related to the atomic mass dependence of the cross section assumed in the simulation event generator. If the relative size of signals were incorrect, then the contamination of a signal in a material from adjacent materials would be wrong. Actually, the relative normalization of the signals from different materials has been corrected by the weighting procedure described in a later chapter. The weights match the simulation signal size in the different materials to the data (see Figure 7.4). The error on this normalization is about 10%. The contamination of one material on the next ranges between 0% and 3%. Since the contamination changes in proportion to the relative signals, the error

	Truth Table	Gained	Lost	Reconstructed
Tungsten	2932	67	167	2832
Copper	3126	51	197	2980
Aluminum	1803	51	51	1803
Downstream Beryllium	2558	22	41	2538
Upstream Beryllium	942	317	131	1128
Everything Else	3607	84	5	3686
Tungsten		2.3%	5.7%	96.6%
Copper		1.6%	6.3%	95.3%
Aluminum		2.8%	2.8%	100%
Downstream Beryllium		0.9%	1.6%	99.2%
Upstream Beryllium		33.7%	13.8%	120%
Everything Else		2.3%	0.1%	102.2%

Table 6.1: Target material distributions of events, truth table versus reconstruction. The Z coordinates of the truth table and reconstructed primary vertices determine the material. The top half of the table shows the number of events by material. The bottom half of the table shows percentages (of the truth table number). Truth table column is the number of events assigned to each material by the truth table. The gained column shows the number assigned to that material by the reconstructed vertex, but not the truth table vertex. The lost column is the number of events that are assigned to that material by the truth table vertex, but not the reconstructed vertex. The events are the ones that passed the primary analysis cuts from the first 800,000 monte carlo events generated. They are weighted.

on the Ξ^- cross sections cannot be more than $.03 * 0.10 = .003$, or 0.3%. This is negligible.

Table 6.1 includes only events that have a primary vertex. The fraction of events where the vertex algorithm fails to find a vertex is:

Tungsten	$0.7\% \pm 0.2\%$
Copper	$0.7\% \pm 0.2\%$
Aluminum	$1.3\% \pm 0.3\%$
Beryllium	$0.6\% \pm 0.2\%$
(Downstream Be foils only)	

The fraction that have no vertex is small and there is no clear trend as a function of material. The systematic error related to this must be negligible.

There is one source of systematic error that is significant. It is related to a discrepancy between the simulation and data in the vertex position errors. One can see the discrepancy clearly if one compares distributions of the z coordinate of the primary vertex for data and simulation. On average, the errors are larger in data.

A method was developed to study these effects using only data. Figure 6.2 shows a distribution of data events versus the reconstructed z coordinate of the primary vertex. A complicated function is fit to the distribution. The function is a sum of 26 separate peaks. Each peak models events from one foil. The location of each peak is fixed in the fit. The shape of each peak is the same, except the width is multiplied by a factor related to fit parameters. The areas are also related to fit parameters.

After the fit is completed, one can calculate the sum of the areas of the peaks associated with each material. This quantity is analogous to the simulation truth table number of events shown in Table 6.1. Alternatively, one can take the function and integrate over regions corresponding to each material. This is the number of events the reconstruction will assign each material. This is analogous to the number

of reconstructed events in Table 6.1. One can take the ratio of these two numbers and find a quantity analogous to the percentages in Table 6.1 (last column, bottom half). The atomic mass dependence of the Ξ^- cross section is only affected by the difference in the ratios for different materials. The most important difference is the one between the ratio for beryllium and the ratio for tungsten. The areas, ratios, and difference are shown in Table 6.2.

The systematic error is studied by varying the function. First, the shape of the peaks is changed by reducing the size of the tails. Instead, a constant term is added to the function. It represents background unassociated with any foil and prevents the fit from becoming poor. Second, the peak widths for the upstream beryllium foils are increased. See Table 6.2 for the results. The variations change the difference in the ratios by 0.9% in both cases. There are many other ways one could vary the function. There are many parameters. But the other parameters are better determined by the data and have less impact on the final result.

In order to get large statistics, this data study uses all events that pass the Ξ^- strip with no background subtraction or trigger weighting. There could be differences between this sample and the weighted data signals passing all the cuts. If one compares z distributions, one can estimate that there is about a 1% discrepancy in the amount of signal lost from all foils due to vertex errors.

One can compare the results of the simulation study and the data study. For the simulation (Table 6.1), the reconstructed signal is 96.6% of the truth table signal for tungsten, 99.2% for beryllium. $99.2 - 96.6 = 2.6$. Using the analogous quantities from Table 6.2, the difference is 3.7%. The difference between 2.6% and 3.7% is 1.1%. Take this as an additional error on the relative signals.

Four independent sources of systematic error have been identified and estimated to be: 0.9%, 0.9%, 1.0%, and 1.1%. Adding these in quadrature gives 2.0%. 2.0% is the estimate for the overall systematic error on the relative signals due to vertex errors.

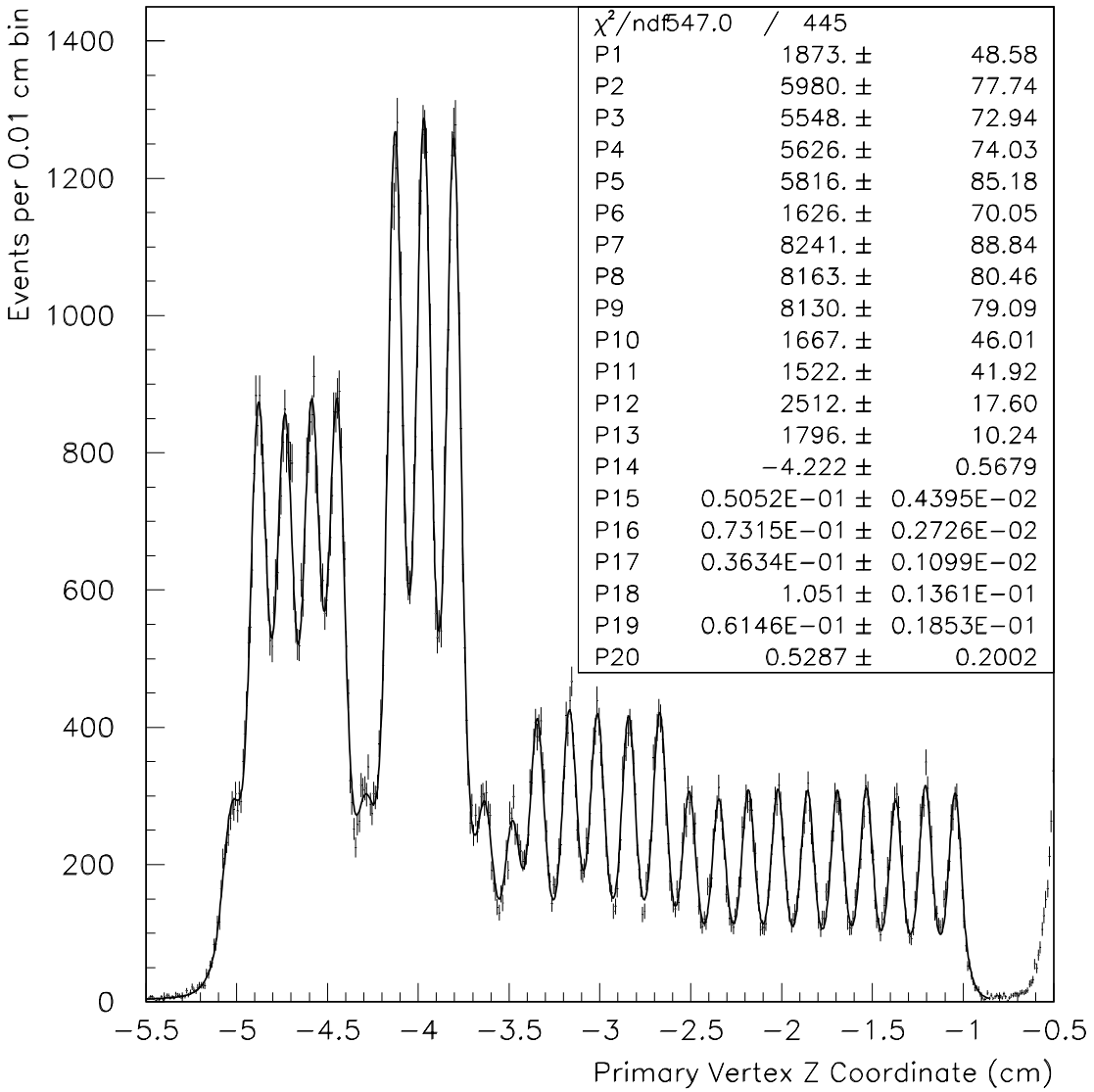

Figure 6.2: Distribution of the Z coordinate of the primary vertex in data. All events that pass the Ξ^- strip are included with no weighting. The fit is used to approximate the effect of vertex errors on the assignment of material to each event.

	Areas of Peaks Calculated from the Function (Analogous to Truth Table)	Areas Integrated Over a Range of Z (Analogous to Reconstructed)	Ratio Integrated Divided by Actual Areas	Difference in Ratios Be − W
Best Fit				
Tungsten	42053	40385	0.960	
Copper	44916	42530	0.947	
Aluminum	23290	22867	0.982	
Downstream Beryllium	32189	32083	0.997	0.037
Vary Functional Form, Repeat Fit				
Tungsten	41251	40376	0.979	
Copper	44151	42525	0.963	
Aluminum	22948	22865	0.996	
Downstream Beryllium	31280	32051	1.025	0.046
Vary Width of Foils 1 and 6, Repeat Fit				
Tungsten	41665	40384	0.969	
Copper	44596	42528	0.954	
Aluminum	23327	22872	0.980	
Downstream Beryllium	32171	32069	0.997	0.028

Table 6.2: This table shows the results of a study of the effect of vertex errors on the assignment of target material to each event. This study is based only on data, not simulation. The ratios in the next to last column can be compared to the simulation results in the bottom half of the last column of Table 6.1.

6.3 Mass Plots, Signal and Background

Figure 6.3 is a histogram of the Ξ^- mass for candidates that pass the primary analysis cuts and have a primary vertex near a target foil. Events are weighted for triggers as described in Section 6.1. The histogram has a sharp peak and a linear background.

The Ξ^- signal is calculated using sideband subtraction. The procedure for sideband subtraction is simple. There are four regions identified in Figure 6.3. B1, B2, and B3 are regions of background. Region S is the Ξ^- signal. $B1$, $(B2+S)$, and $B3$ are measured by summing all the entries in the respective regions of the histogram. $B2$ and S cannot be separately measured this way, because they share the same range of Ξ^- mass. The entries are weights, that means the weights are added. The errors are calculated by adding the weights in quadrature. The signal and error are calculated using the formulas:

$$\text{signal} = (B2 + S) - \frac{B1 + B3}{2} \ ,$$

$$\sigma_{\text{signal}} = \sqrt{\sigma^2_{(B2+S)} + \frac{\sigma^2_{B1}}{4} + \frac{\sigma^2_{B3}}{4}} \ .$$

An alternate method of quantifying the signal was considered. Figure 6.3 shows a curve fit to the histogram. The curve is the sum of two gaussians plus a linear background. One gaussian has its center fixed at 1.3211 GeV/c^2 with σ fixed at 2.04 MeV/c^2, the other has its center fixed at 1.3219 GeV/c^2 with the σ fixed at 4.09 MeV/c^2. The area of the first gaussian is fixed to be 0.6334 of the total area under the peak. Parameter 1 is the total area under the peak, parameter 2 is the height of the background in the center of the plot, and parameter 3 is the slope of the background.

The shape of the central peak is complex. It is determined by the errors on reconstructed track momenta and track directions. The peak is asymmetric. It has a larger tail on the high mass side. A gaussian gives a poor fit. The peak is sharper than a gaussian in the middle, but wider than a gaussian at the edges.

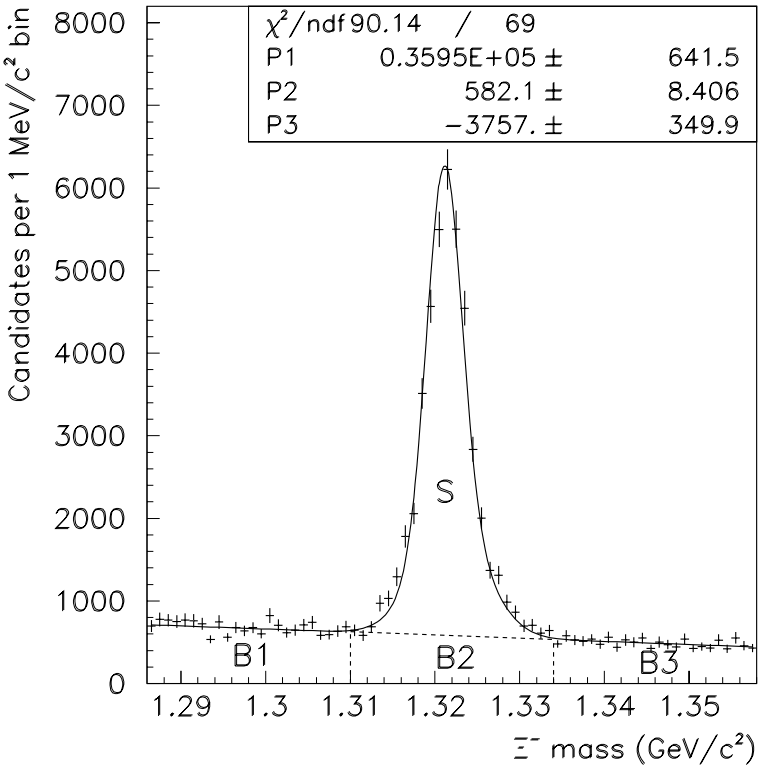

Figure 6.3: This is a histogram of the Ξ^- mass for candidates passing all the analysis cuts with a primary vertex near a target foil. The three large regions are all the same width, 24 MeV/c^2. The boundaries of the three regions are at 1.286 GeV/c^2, 1.310 GeV/c^2, 1.334 GeV/c^2, and 1.358 GeV/c^2. They are slightly offset from the Ξ^- mass, because the peak is asymmetric. Candidates are weighted based on trigger prescalers. The average weight is 1.56.

The sideband subtraction method gives a signal of 36830 ± 710. The fit to a double gaussian function gives a signal of 35950 ± 640. The two methods agree within about 2.4%. The advantage of using the fit is that information on the shape of the curve is used to improve the signal estimate and decrease the statistical errors. But in this case, the shape of the peak is not known. Even the double gaussian is not exactly right. Further, the peak shape changes in different x_F and p_T regions. There would be a systematic error based on the shape of the peak used. This would nullify the advantage of using the fits. For this reason, the sideband subtraction method is used. The sideband subtraction method has other advantages. Sideband subtraction is easy to implement, executes fast, and is easy to explain. The only

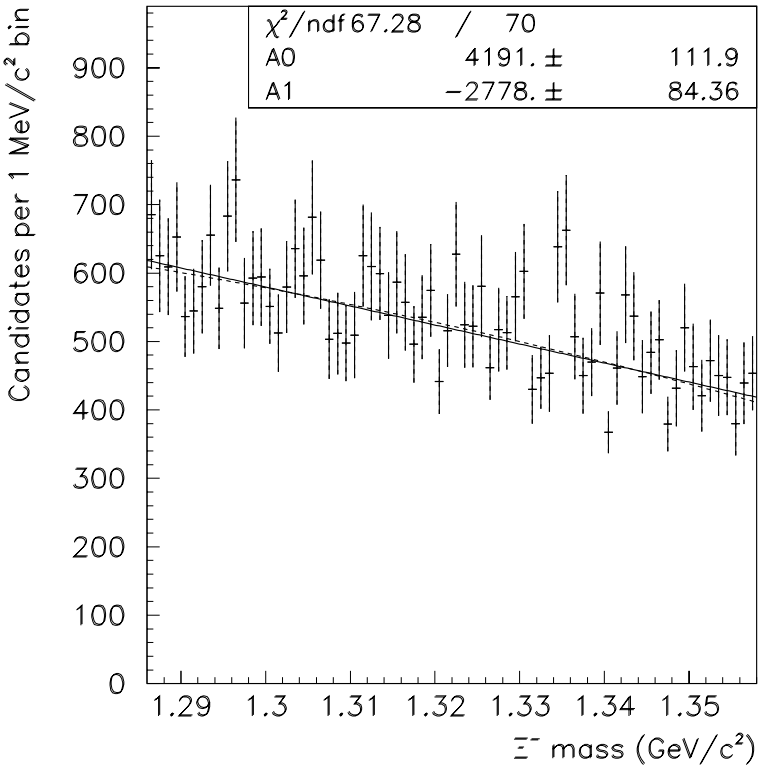

Figure 6.4: This is a histogram of the Ξ^- mass for candidates with the wrong sign combination. There are two curves superimposed on the plot. One is a fit to a linear background (fit parameters shown, solid line). The other is a fit to a quadratic background (dotted line, $\chi^2 = 63.88$). Candidates are weighted.

assumption about the peak shape is that it fits within the region identified as B2 and S on Figure 6.3. The background must be linear for sideband subtraction.

A good way to study the background is to plot Ξ^- candidate events with the wrong sign combination for the decay products. Figure 6.4 shows candidate events where the pion from the Ξ^- decay has the same sign as the proton from the Λ decay. Ξ^-'s cannot decay with this charge combination. All the events in the plot are background. All the other cuts are identical to the cuts used for Figure 6.3. There are two curves fit to this plot, one linear and the other quadratic. The two fits are so close that is difficult to tell them apart. Based on the fits in Figure 6.3 and Figure 6.4, one concludes that the systematic error related to the sideband subtraction method is negligible.

6.4 Analysis Cuts

This section describes three different sets of analysis cuts. The primary set of cuts is described first. These cuts are used to find Ξ^-'s using tracks with only drift chamber hits. The published results are based only on candidates passing the primary cuts. The other two sets of cuts use SMD tracks.

6.4.1 Primary Analysis Cuts

Ξ^-'s are identified through the following decays:

$$\Xi^- \rightarrow \Lambda + \pi^-$$

$$\Lambda \rightarrow p + \pi^-$$

The proton and the two pions leave tracks in the detector which are used to identify Ξ^-'s. The search procedure is simple.

Three tracks are selected. One is assumed to be the proton track. One is assumed to be the track of the π^- from the Λ decay. One is assumed to be the track of the π^- from the Ξ^- decay. There is one line perpendicular to the tracks of the Λ daughters that intersects both tracks. The point on this line midway between the two tracks is set as the Λ decay vertex. The Λ momentum is set equal to the sum of the momenta of the two tracks. This establishes a Λ track. The process is repeated with the Λ track and the other π^- track to establish a Ξ^- decay vertex, Ξ^- momentum, and a Ξ^- track. The masses of the Λ and Ξ^- are calculated from the momenta of their daughters and the known masses of their daughters. This is repeated for every permutation of three tracks in every event.

Each candidate Ξ^- decay must pass the following analysis cuts:

1. All three tracks must be reconstructed from drift chamber hits only, no silicon microstrip detector (SMD) hits. This eliminates a lot of combinatoric background.

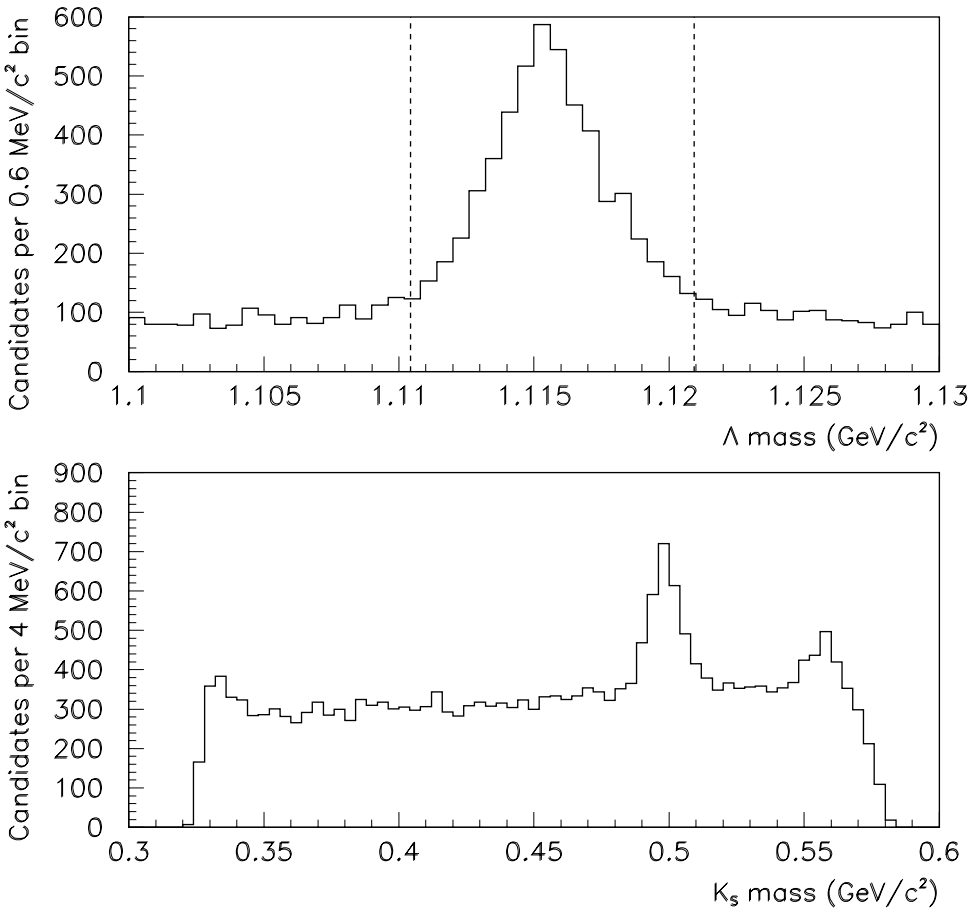

Figure 6.5: These are histograms of the mass calculated for the Λ and recalculated for the Λ as a K_S. The dotted lines indicate the cut region. The Λ mass must be in the region. The K_S plot includes only events where the mass of the Ξ^- is outside the central mass peak, and in the background sidebands. The K_S mass is 0.497 GeV/c^2.

2. The ratio between the impact parameter of the Ξ^- to the primary vertex and the distance the Ξ^- travels in the z direction must be less than 0.012.

3. The distance between the tracks of the Ξ^- daughters must be less than 0.66 cm.

4. The distance between the tracks of the Λ daughters must be less than 0.7 cm.

5. The Λ mass must lie within .00525 GeV/c^2 of 1.115684 GeV/c^2 (see Figure 6.5).

6. The Λ must decay between z = 20 cm and z = 230 cm.

7. The Ξ^- must decay after z = 7 cm, after the primary vertex, and no more than 5 cm beyond the Λ decay point. The 5 cm allows for vertex position errors.

8. There must be at least one primary vertex.

9. The two π's must have the same charge, while the proton (or anti-proton) must have a charge opposite that of the π's.

10. The event must have passed the minimum bias trigger or the standard ET trigger.

11. All three tracks must have hits in the first set of drift chambers (D1) and at least one additional drift chamber. This ensures tracks have a good momentum measurement.

12. The x and y intercepts at z = 0 of all three tracks must be less than 7.999 cm. Few tracks fail this cut. It is included because the reconstruction process assigns all tracks with an intercept larger than 8 cm an intercept of 8 cm. The purpose was to save space in the output DST's.

13. The sum of the chi squared per degree of freedom of the tracks of the Λ daughters must be less than 7.0. This cut is very loose and has no significant effect.

14. The momentum of the proton must be 2.5 times greater than the momentum of the pion from the Λ. Kinematics require this to be true.

15. The absolute value of the cosine of the angle between momentum of the Λ in the lab frame and the momentum of the proton track in the Λ rest frame must be less than 0.99. This is a loose cut that removes a small amount of signal.

16. x_F of the Ξ^- must be between -0.09 and 0.15

17. Only Ξ^- candidates with mass between 1.286 GeV/c^2 and 1.358 GeV/c^2 are used in the signal and background calculation.

18. The beam probability must be greater than 90% for pion beam.

19. The two pion tracks must be different. They are considered the same if they have the same total momentum within 0.4 GeV/c and make an angle of less than 7.7 mrad (cosine 0.99997). See Figure 6.6.

20. A reconstructed track cannot be used in more than one Ξ^- candidate. When multiple Ξ^- candidates use the same tracks, the best is selected by the track order. The tracks are quality ordered by reconstruction program. This cut is made last, after all the cuts listed above. See Figure 6.7.

Where appropriate, the cuts were tuned using studies of the statistical significance as a function of the cut level. Figures 6.8, 6.9, and 6.10 show the results of a few of these studies (also see Ref. [3]).

Statistical significance is calculated using the formula

$$\text{significance} = \frac{aS}{\sqrt{aS+B}} \ .$$

S is the monte carlo signal and a is a normalization factor. a is the ratio of data signal to monte carlo signal calculated near the final cut value. B is the background level in the data ($B = 0.75 * (B1 + B3)$, see Section 6.3). Errors on the statistical significance are shown only in Figure 6.8, but they are similar in all cases. The errors are correlated from bin to bin so they do not mean much. All cuts are at their final level except the cut being varied.

Background from K_S and Ω^- particles was studied. The K_S contributes to the background. Figure 6.5 shows the K_S signal in the Ξ^- mass sidebands. We looked at the K_S signal separately in each Ξ^- sideband and the Ξ^- signal region to verify that the K_S signal is smeared out over all three regions in the Ξ^- mass distribution. Sideband subtraction should account for the background. Figure 6.11 shows that a

cut on the K_S mass would decrease statistical significance. The cut was not made. The Ω^- background was negligible.

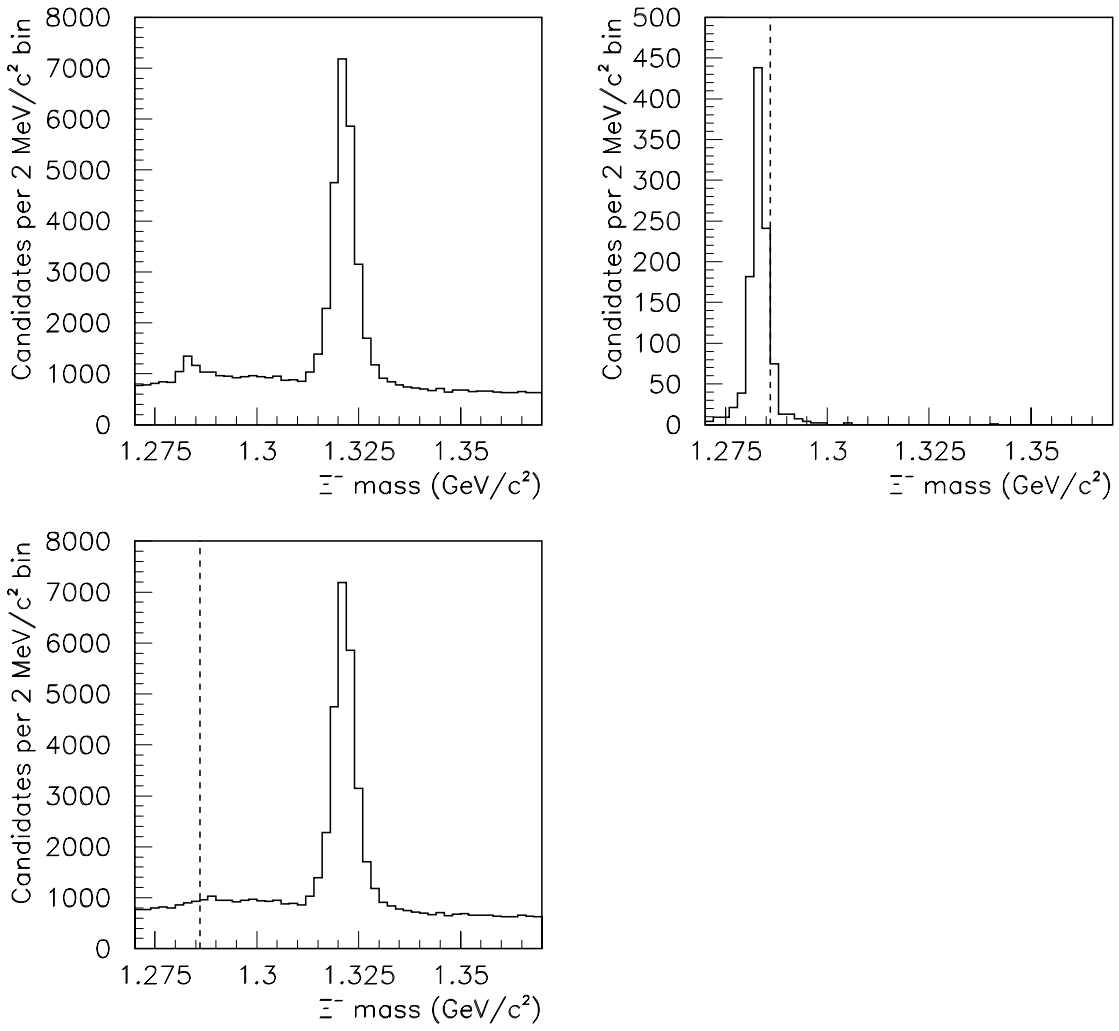

Figure 6.6: Effect of the duplicate pion cut. Sometimes one real track will be reconstructed twice. When this happens for the π^- from the Λ decay, a false mass peak at 1.284 GeV/c^2 is created. These plots study the cut that removes this background. In the top left plot, no cut is made requiring the tracks be distinct. In the top right plot, the false mass peak is selected by requiring the 2 pion tracks have momenta within 0.4 GeV/c and make an angle less than 7.7 mrad. No genuine Ξ^- signal at 1.321 GeV/c^2 passes this cut. In the bottom plot, the cut removing the false mass peak is made. The dotted lines show the lower edge of the lowest bin used in the signal calculation. The entries in the histograms are unweighted.

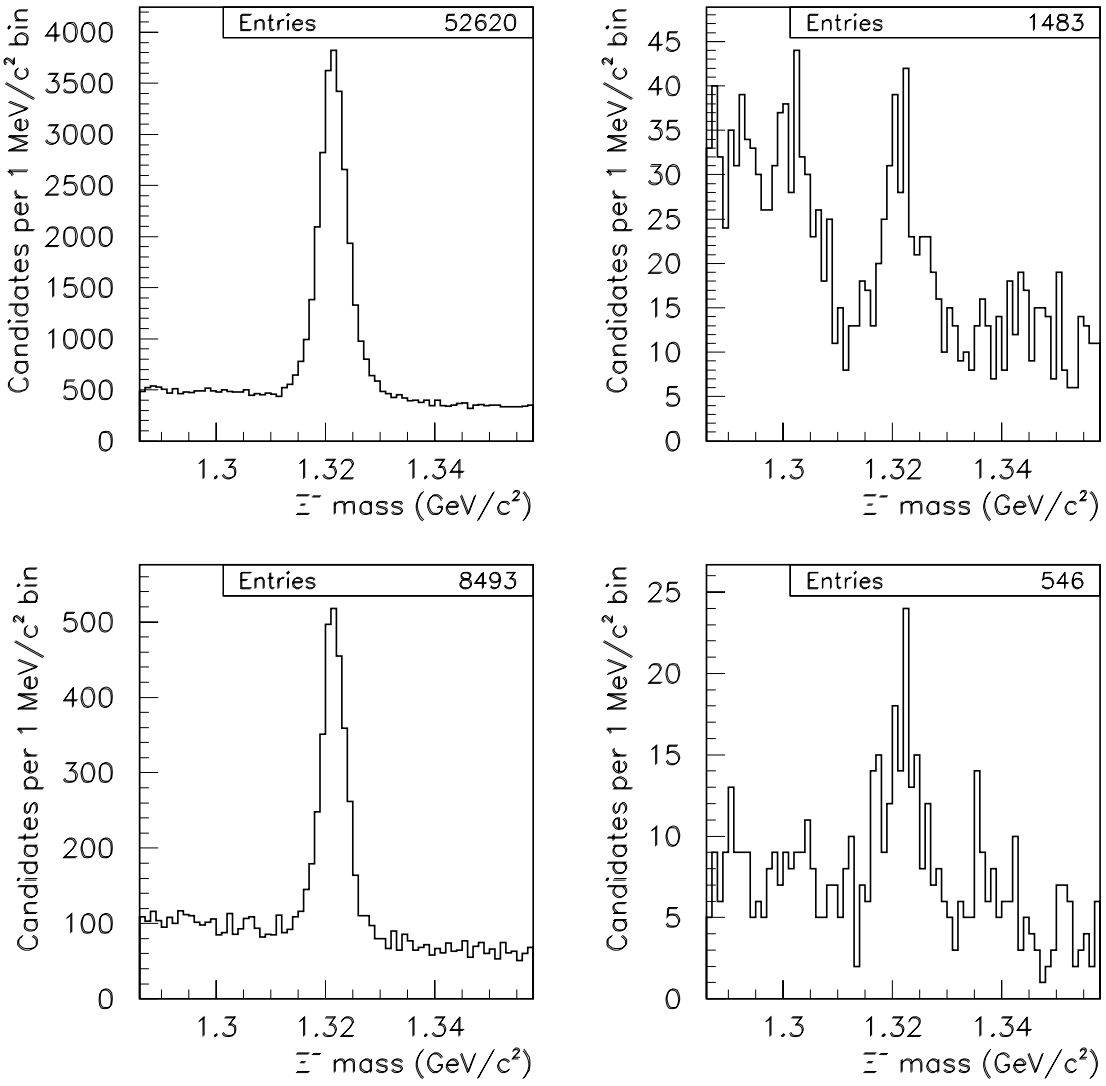

Figure 6.7: Effect of the duplicate track cut. Each reconstructed track may be used in only one Ξ^- candidate. The primary purpose of this cut is to remove duplicate Ξ^- candidates that are created when the tracks of the three Ξ^- decay products reconstruct multiple times. The top plots are for 3 DC track candidates. The bottom plots are for candidates with an SMD track used for the pion from the Ξ^- decay. The left plots are made with all the final analysis cuts applied. The right plots show the events removed by the cut that allows reconstructed tracks to be used only once. The entries in the histograms are unweighted. From these plots, one can see the number of duplicates is small. The cut removes all the duplicates and gets some background as a side benefit.

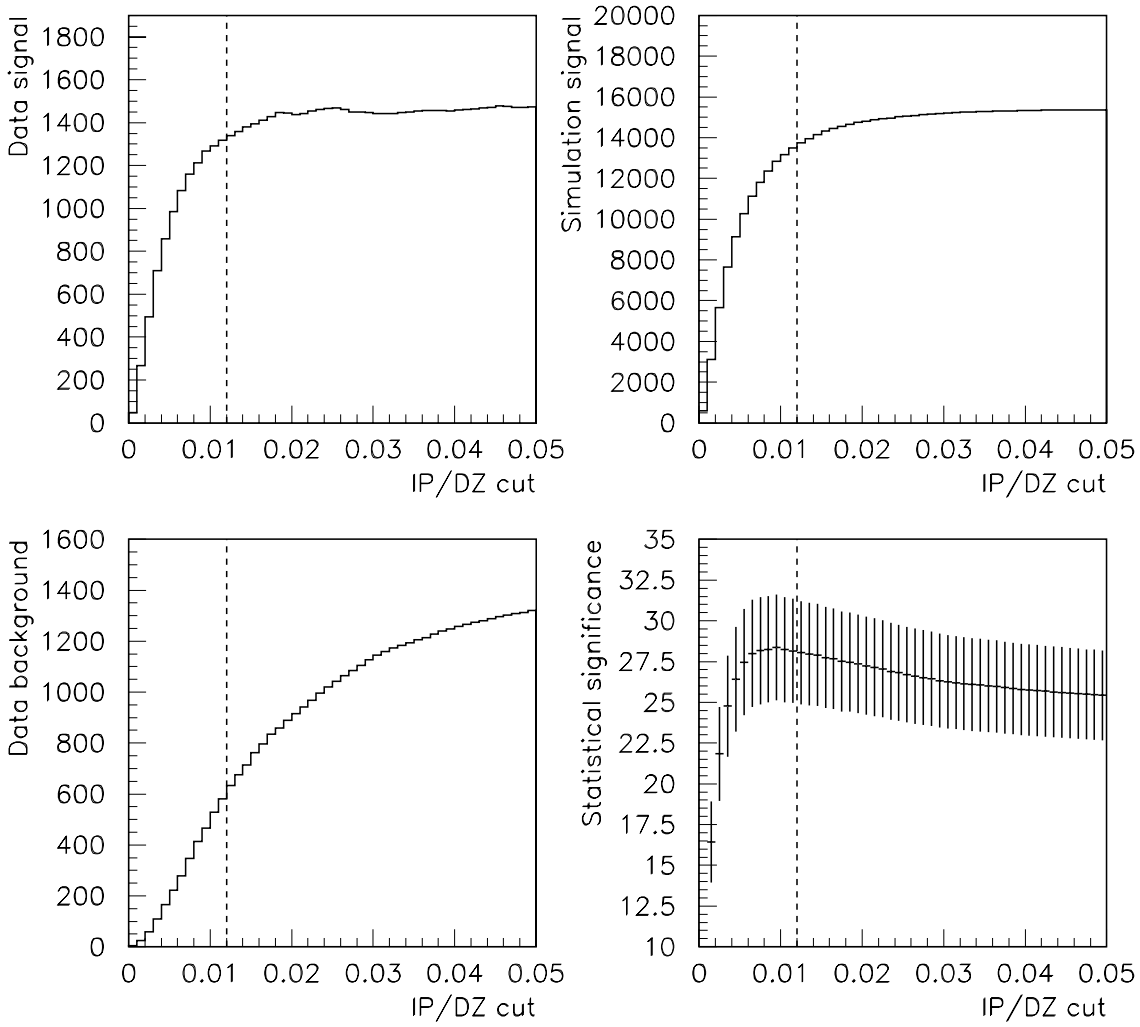

Figure 6.8: Statistical significance of the IP/DZ cut. IP is the impact parameter of the Ξ^- track to the primary vertex. DZ is the distance in the z direction between the primary vertex and the Ξ^- decay point. IP/DZ is the ratio (IP divided by DZ). The cut is the maximum allowed value of IP/DZ. The dotted line indicates the cut used in the analysis.

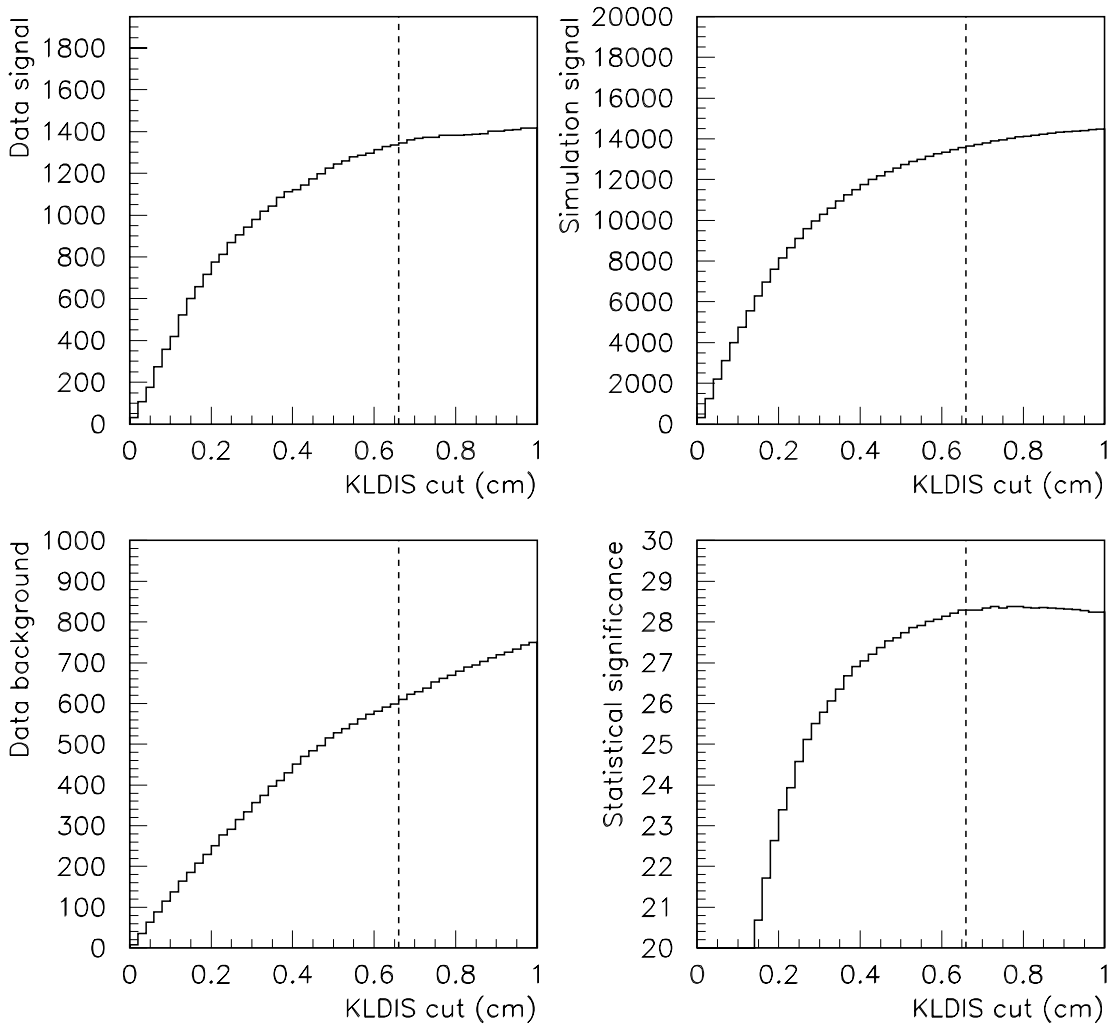

Figure 6.9: Statistical significance of the KLDIS cut. KLDIS is the shortest perpendicular distance between the Λ track and the track of the pion from the Ξ^- decay. The cut is the maximum allowed value of KLDIS. The dotted line indicates the cut used in the analysis.

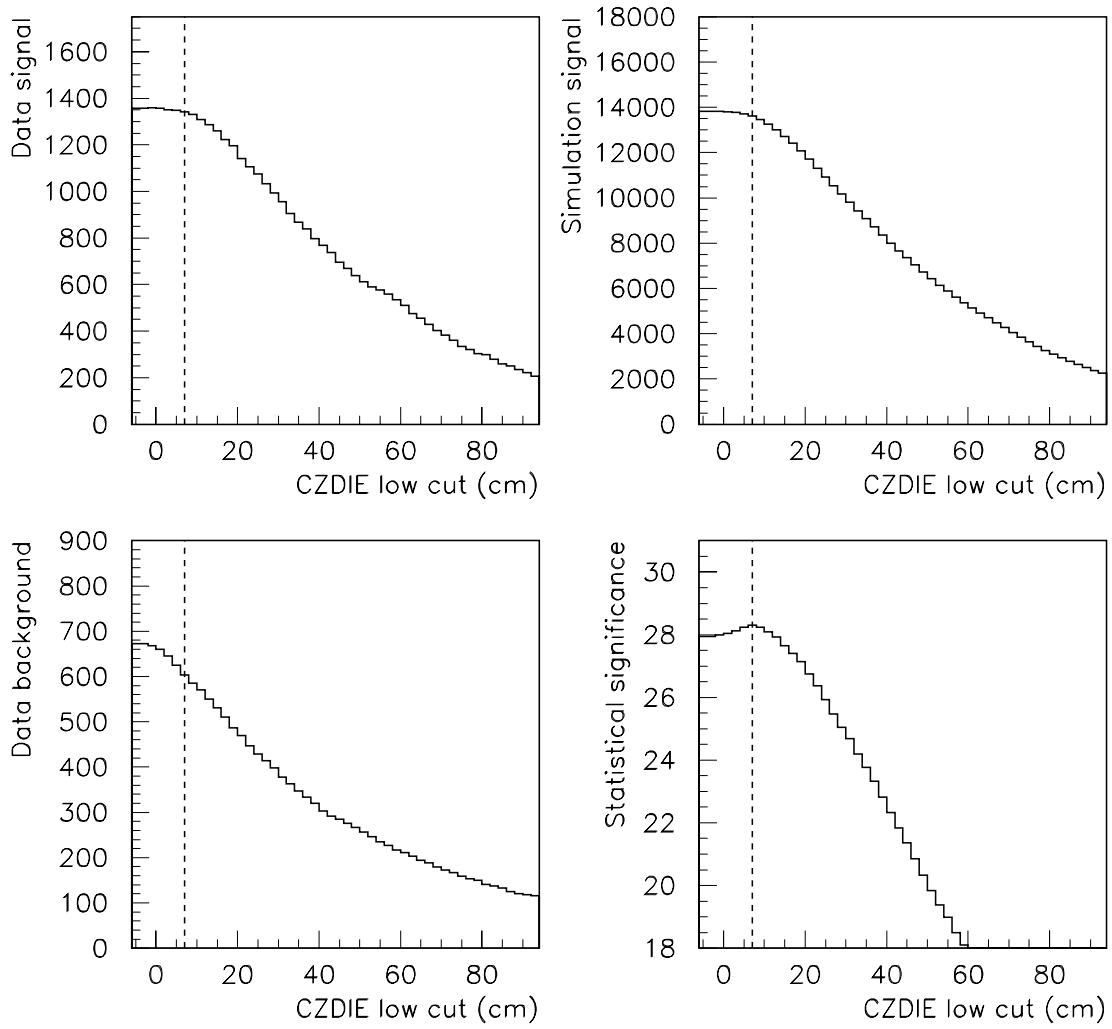

Figure 6.10: Statistical significance of the CZDIE low cut. CZDIE is the Z coordinate of the position of the Ξ^- decay. The cut is the minimum allowed Z coordinate for the decay. The dotted line indicates the cut used in the analysis.

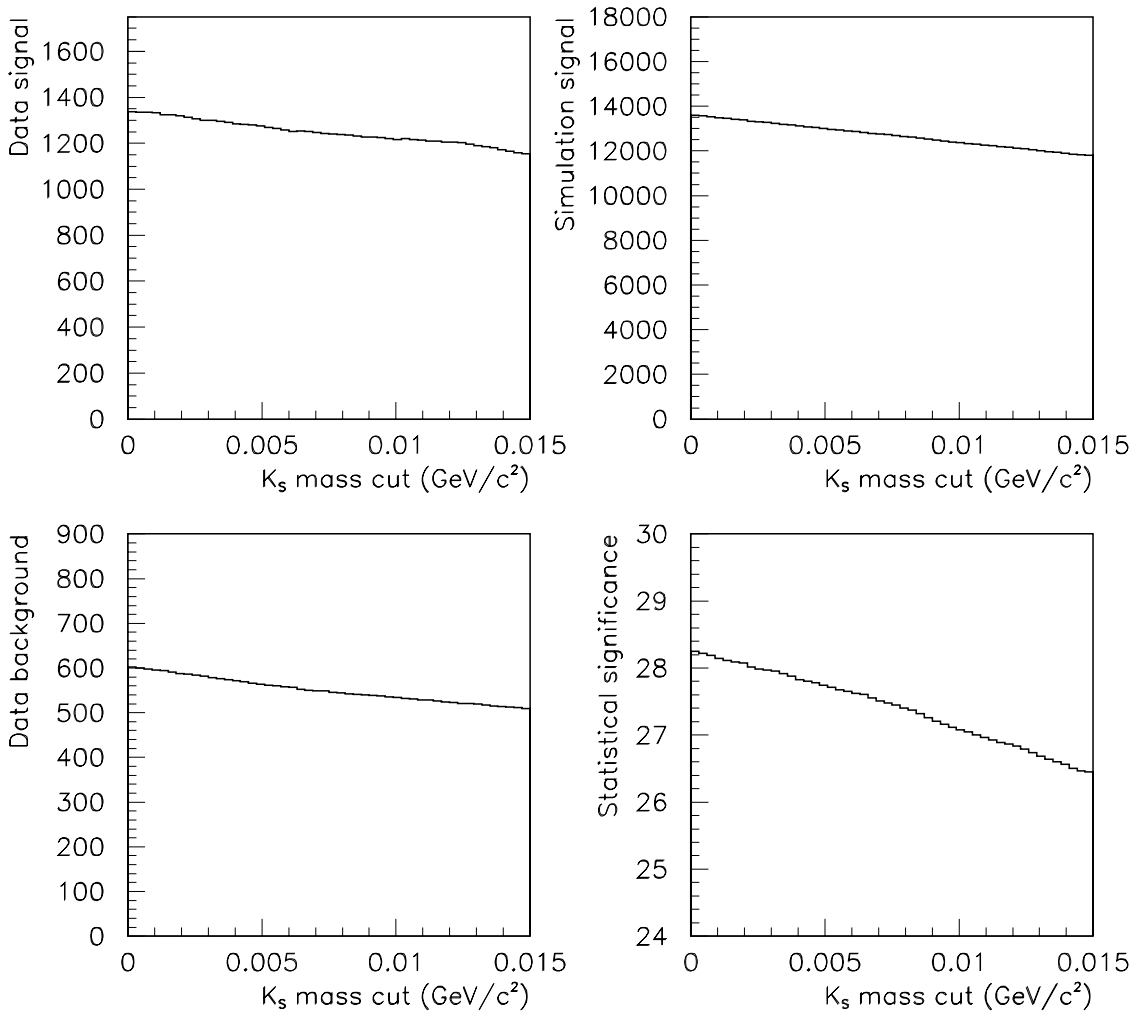

Figure 6.11: Statistical significance of the K_S mass cut. Some of the Ξ^- background comes from events where particles from K_S decay and another random particle have momentum like particles from Ξ^- decay. One studies this by recalculating the mass from the two tracks assumed to be from Λ decay and assuming they are from K_S decay. The cut requires the absolute value of (K_S mass - 0.497 GeV/c^2) be greater than the cut value. Based on this plot, the cut was not made.

6.4.2 SMD Tracks for the Ξ^-

In a little more than a third of the signal events, one can find an SMD track for the Ξ^-. In these special cases, one can identify *additional* Ξ^-'s above and beyond those identified in the primary cuts. The cuts for these events are the same as the cuts described in the previous section with the following exceptions:

1. The SMD track list is searched for the track that makes the smallest angle with the Ξ^- track reconstructed from the three drift chamber tracks. The cut requires the cosine of this angle to be greater than 0.9999984 (angle less than about 2 mrad). Only SMD tracks with no hits in drift chamber assemblies D2, D3, and D4 are considered.

2. The cut on the distance between the tracks of the Ξ^- daughters is eliminated.

3. The cut on the ratio between the impact parameter of the Ξ^- to the primary vertex and the distance the Ξ^- travels in the z direction is eliminated.

4. The cut on the Λ mass is loosened. The Λ mass must be within .01 GeV/c^2 (changed from 0.00525 GeV/c^2 in primary cuts) of 1.115684 GeV/c^2.

The original tracking reconstruction did a poor job of finding the SMD tracks for the Ξ^-. If it had been tuned to find them, the vast majority of the candidates would have an associated Ξ^- track. The systematic effects related to this are not understood. For this reason, this approach is not used to derive the final published results. In a later chapter, atomic mass dependence results will be shown for the *additional* events found with the cuts above. It is only a consistency check. No systematic error is associated with the result.

6.4.3 SMD Tracks for the π^- Created in the Ξ^- Decay

One can also find a significant signal using SMD tracks for the π^- created in the Ξ^- decay. The cuts for these Ξ^-'s are identical to the primary set of cuts, with the following exceptions.

1. The track for the pion from the Ξ^- must be an SMD track.

2. The impact parameter of the SMD pion track to the primary vertex must be greater than .05 cm. This is a new cut that is very effective for SMD tracks, but useless for drift chamber tracks.

3. The Ξ^- must decay between the primary vertex and z = 15 cm.

4. The distance between the tracks of the daughters of the Ξ^- must be less than 0.3 cm.

5. The ratio between the impact parameter of the Ξ^- to the primary vertex and the distance the Ξ^- travels in the z direction must be less than 0.014.

6. A reconstructed track cannot be used in more than one Ξ^- candidate. When multiple Ξ^- candidates use the same track, the best is selected by the track order. The tracks are quality ordered by the reconstruction program. There is an exception made here. 3 DC track Ξ^- candidates are done first. SMD tracks are last, even though they are first in the tracks arrays.

There is one difference in the procedure for finding the Ξ^- vertex when the pion has an SMD track. Normally, the vertex is set halfway between the Λ track and the π^- track. In this case, the vertex is set closer to the π^- track (91% of the way from the Λ track to the π^- track).

One might also consider looking for the daughters of the Λ with SMD tracks, but this is hopeless. Less than 2% of the Λ's decay before the SMD, and there is a tremendous amount of combinatoric background.

Chapter 7

Simulation

Monte Carlo techniques were used to simulate Ξ^- production and the behavior of the Fermilab E769 detector. The simulation was used to calculate acceptances and study systematic errors. The last two sections of this chapter discuss the acceptances.

The event generator simulated the primary interaction between a beam particle and a nucleus in the target. The event generator used in this analysis was different from the generator used for E769 charm studies. The event generator is discussed in detail in the next section.

The detector simulation used for E769 charm studies was used for this analysis. The detector simulation was not significantly modified. It extrapolated particle trajectories through the detector. It simulated the response of the drift chambers, silicon microstrips, and other components of the detector. It also modeled the magnetic field, secondary interactions, pair production, and many other things. The output of the detector simulation was processed by the same reconstruction and analysis codes used for data.

7.1 Event Generator

The original idea was to use the PYTHIA [62, 63, 64] generator with all its options and parameters set at the default values. This failed. The Ξ^- momentum distributions and event multiplicities in the reconstructed data and reconstructed simulation were very different. The new version of the FRITIOF [65] generator and 10 year old versions of PYTHIA and FRITIOF were tried, but also produced poor results. The E769 generator used for charm studies also produced poor results.

In the end, PYTHIA was used to generate events. PYTHIA was tuned (modified) to make the Ξ^- momentum distributions and event multiplicities similar in data and simulation. The next section discusses the Ξ^- momentum distributions. Section A.3 discusses the match between multiplicities for data and simulation.

Version 5.6 of PYTHIA was used with the following settings and modifications:

1. The generator was initialized for a 250 GeV π^- beam on a fixed target. The target was a proton half the time and a neutron the other half.

2. The default list of hadron-hadron processes was selected (MSEL = 1). This includes six processes. The two that produce the most events in this PYTHIA model are the gluon-gluon to gluon-gluon process and the quark-gluon to quark-gluon process.

3. The transverse momentum (p_T) of the hard scattering process was required to be at least 1.451 GeV (CKIN(3)=1.451). This eliminated the PYTHIA process for generating low p_T events. The low p_T process produced events that did not match our data at all.

4. The parameters in the fragmentation function were modified to increase the average multiplicity of events (PARJ(42) changed from 0.9 to 0.65).

5. The parameters setting the transverse momentum distribution inside the hadron before the interaction were changed to increase the transverse momentum in

the event (gaussian width PARP(91) changed from .44 GeV to .59 GeV, upper cutoff PARP(93) changed from 2.0 GeV to 2.8 GeV).

6. Two corrections were applied after generation of the particles that come directly from fragmentation, but before any particles decayed. The transverse momentum of every particle was multiplied by a factor of 1.2. Also, the Ξ^- was given an additional 0.150 GeV of longitudinal momentum in the center of momentum frame of the beam and target.

7. Events that did not have Ξ^-'s were rejected.

8. Λ particles from Ξ^- decay were forced to decay to proton and pion.

9. In the first 800,000 events generated and saved, interactions were generated in the upstream beam detectors and the interaction scintillator. These events added a negligible amount to the acceptance for Ξ^-'s produced in the target foils (13 out of 37550 reconstructed Ξ^-'s). Events with a primary interaction in the upstream beam detectors or the interaction scintillator were not generated for the last 1,000,000 simulation events. In the first 800,000 events generated, Ξ^-'s were generated with all Feynman x (x_F) values allowed. The x_F range where the analysis will give a result is -0.09 to 0.15. Ξ^-'s almost never had an error on x_F greater than 0.015. For the last 1,000,000 simulated events, Ξ^-'s with x_F outside the range -0.105 to 0.165 were rejected and not saved. These two changes resulted in an increase of a factor of 2.3 in the number of useful events generated and saved.

In addition to all the changes listed above, the output format of PYTHIA had to be converted to match the format used by the E769 detector simulation.

7.2 x_F and p_T^2 Weighting Functions

Even after a great deal of effort tuning the generator, Ξ^- momentum distributions for data and simulation did not match exactly. This section describes weighting functions derived to correct the simulation and eliminate the differences. The weighting functions are applied to the simulation by weighting entries in the Ξ^- mass histograms. The weight is the product of the two weighting functions, one to correct the x_F distribution and one to correct the p_T^2 distribution. The weights are used in the acceptance calculation. Figure 7.1 compares data distributions with simulation distributions that have been corrected with the weights. The distributions are consistent.

The procedure for calculating the weighting function involves several steps. Distributions are calculated as a function of x_F (Feynman x of the Ξ^-), and p_T^2 (squared transverse momentum of the Ξ^-). In each bin of the distributions, the Ξ^- signal is calculated using sideband subtraction. The data are the weighted combination of minimum bias and ET trigger events. The distributions are calculated from all available data and all generated simulation. The events in the distributions pass the primary set of analysis cuts. Only events with the primary vertex near a target foil are included.

Figure 7.2 shows the result of dividing the data x_F distributions by the simulation x_F distributions bin by bin. In this figure, the simulation is not weighted. Weighting functions are derived by fitting functions to the points. The x_F weighting functions have the form:

$$\text{weight} = P1 * (1 + P2 * x_F + P3 * x_F^2) \ .$$

Figure 7.3 shows the result of dividing the data p_T^2 distributions by the simulation p_T^2 distributions bin by bin. In this figure, the simulation is weighted by the x_F weighting functions. Weighting functions are derived by fitting functions to the

points. The p_T^2 weighting functions have the form:

$$\text{weight} = P1 * (1 + P2 * p_T^2) \ .$$

The variables $P1$, $P2$, and $P3$ refer to fit parameters. Later in Section A.2, the errors on the parameters from the fit will be used to estimate systematic errors on the atomic mass dependence related to the generated Ξ^- momentum distributions.

Finally, the x_F weighting functions are recalculated with the x_F and p_T^2 weights already applied. This is a check to see if the weighting functions are doing the right thing. It would show errors in the calculation. It would also show the effect of bad correlations between the different functions. These are shown in Figure 7.4. Ideally, these should be flat lines at 1.0.

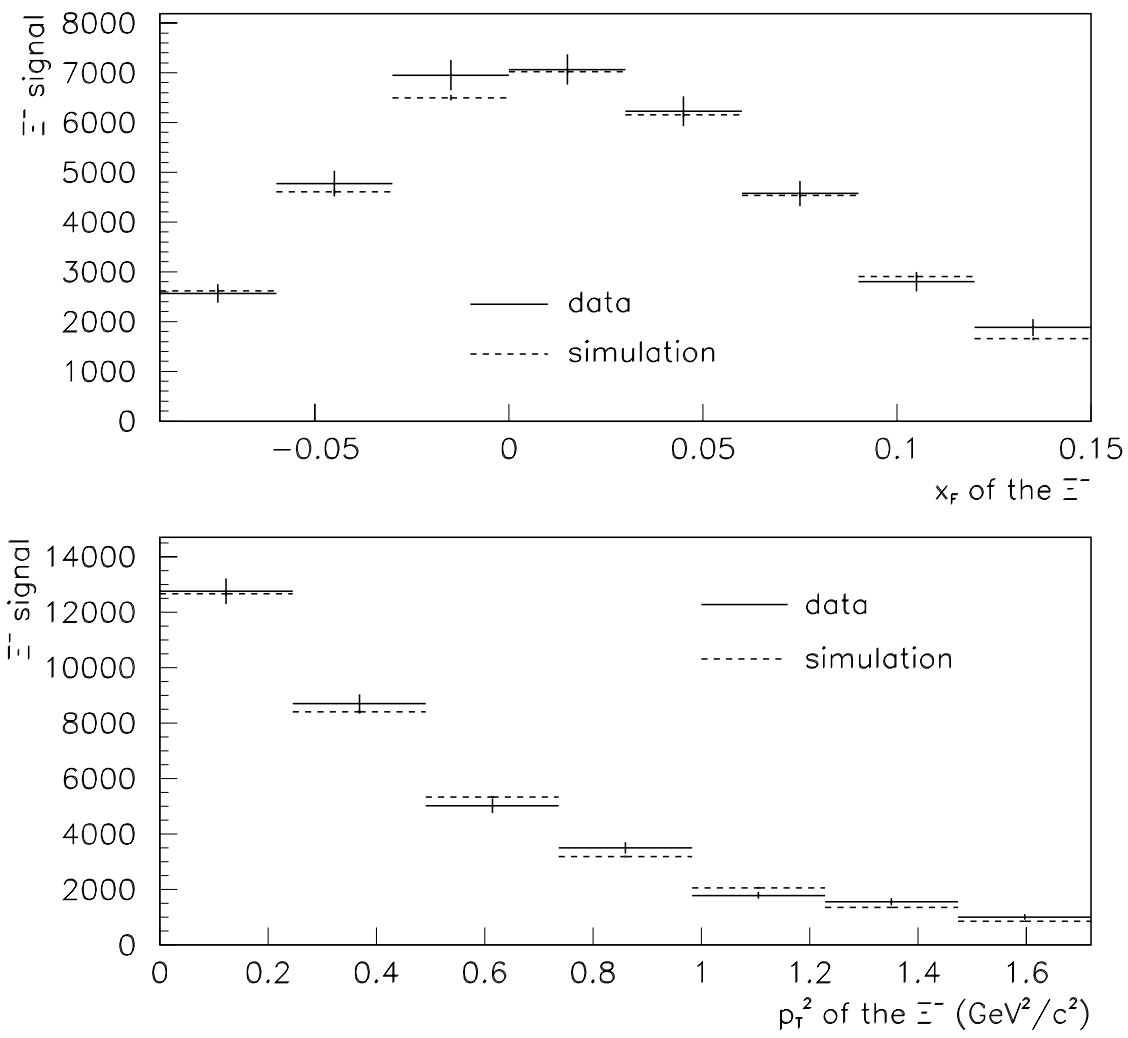

Figure 7.1: These show that the Ξ^- momentum distributions for data and simulation are consistent. x_F and p_T^2 distributions are shown. The data are not acceptance corrected, but they are weighted based on the trigger prescalers. The simulation has been weighted. In addition to correcting the x_F and p_T^2 distributions, simulation weighting also normalizes the simulation signal so that it is the same size as the data signal. For these plots, all four target materials are combined together.

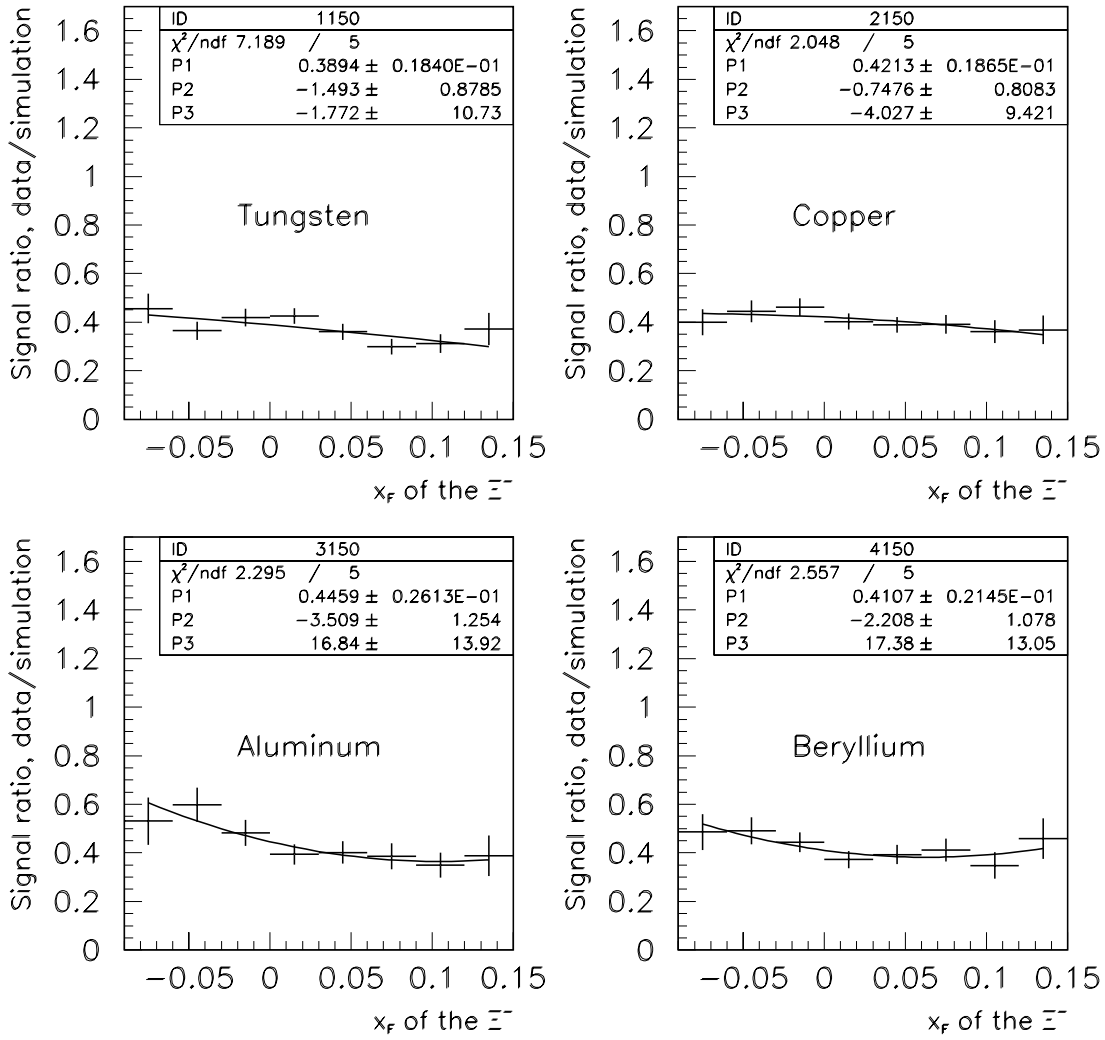

Figure 7.2: Ratio of the data signal to the simulation signal in bins of x_F for each target material. The simulation is unweighted. x_F weighting functions are derived by fitting a second order polynomial to each histogram.

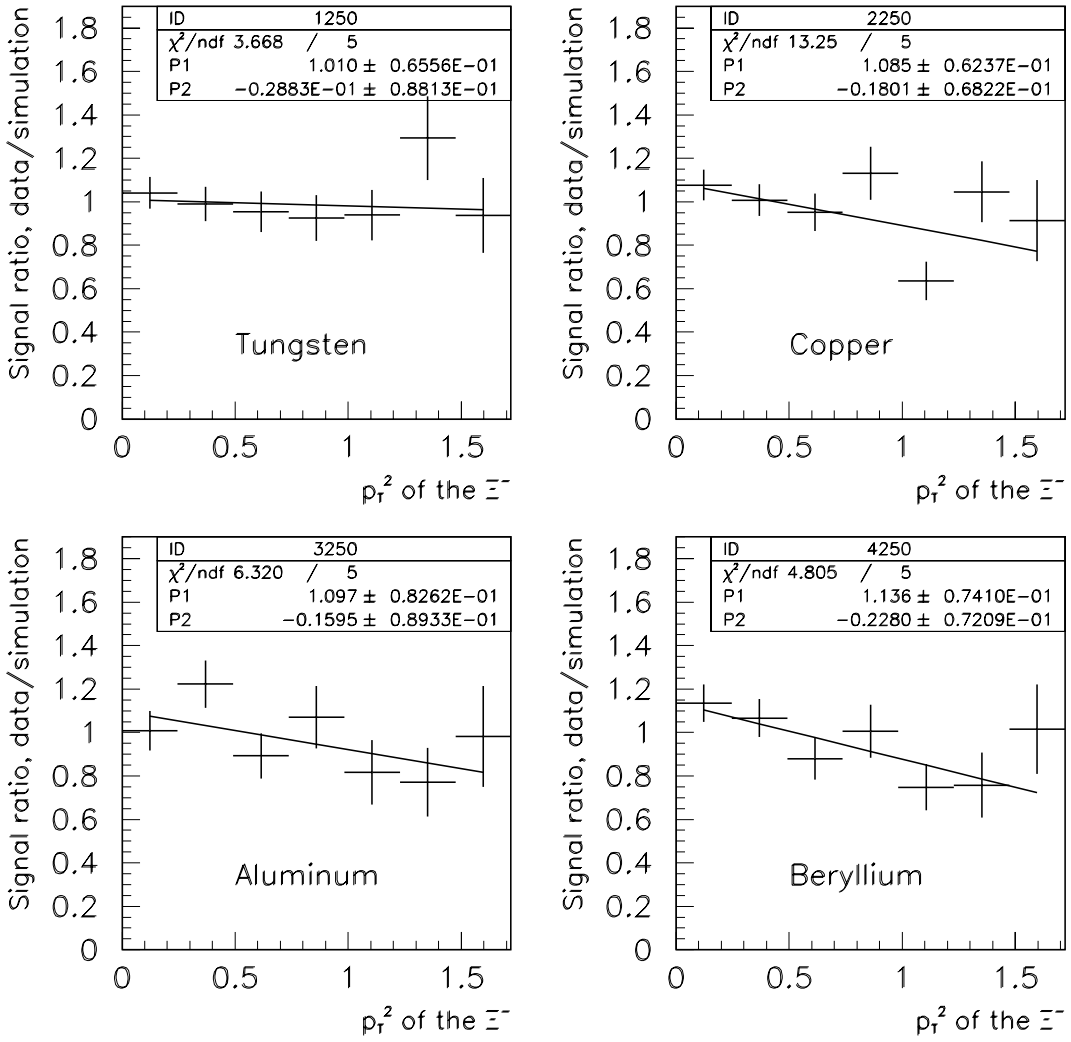

Figure 7.3: Ratio of the data signal to the simulation signal in bins of p_T^2 for each target material. The simulation is weighted by the x_F weighting functions. p_T^2 weighting functions are derived by fitting a first order polynomial to each histogram.

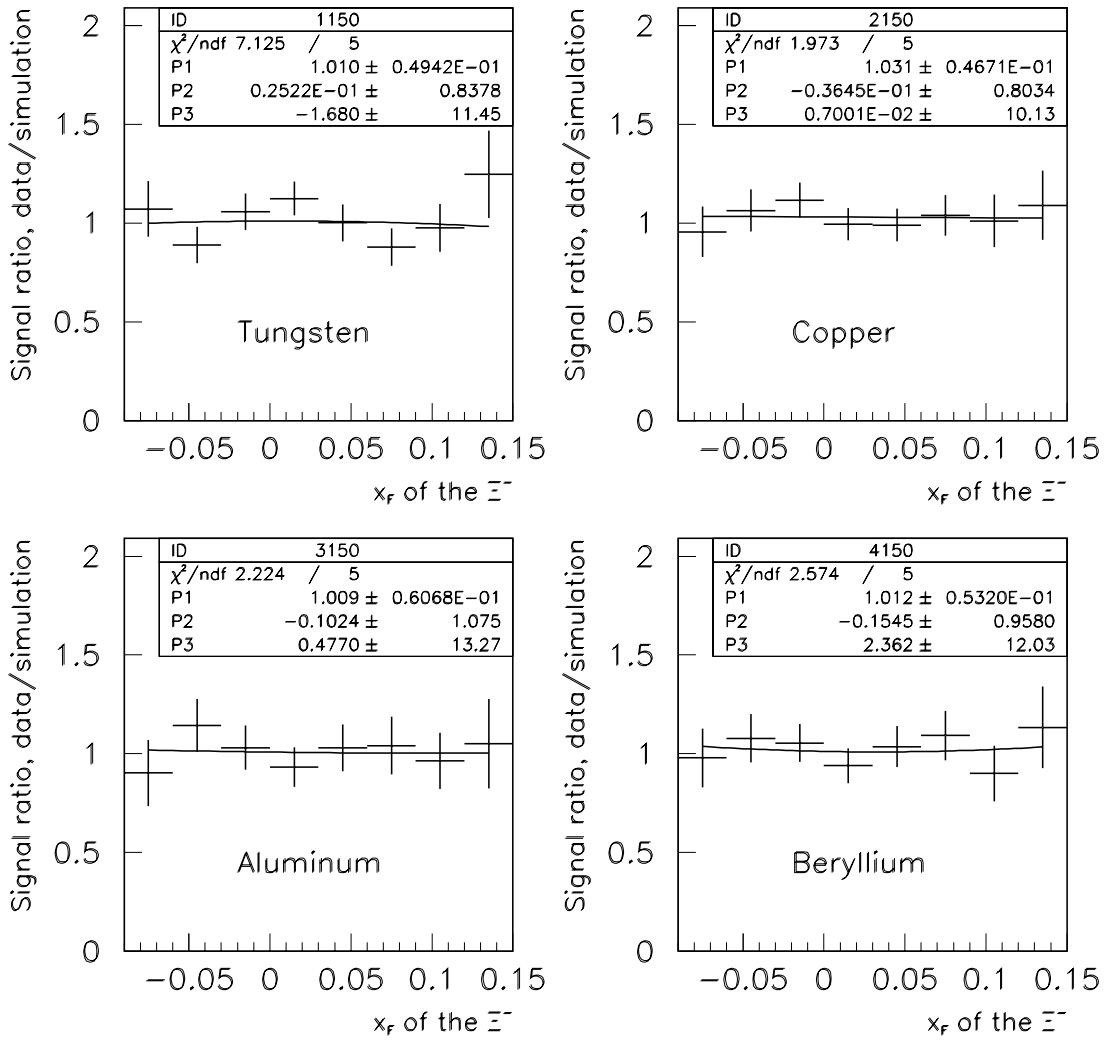

Figure 7.4: Ratio of the data signal to the simulation signal in bins of x_F for each target material. The simulation is weighted by the x_F and p_T^2 weighting functions. This is a check to make sure the weighting functions are correct and have no bad correlations. A second order polynomial is fit to each histogram. The functions should be consistent with a flat line at 1.0. They are.

7.3 Acceptances

The simulation is used to calculate the acceptances. The acceptances are calculated in bins of x_F separately for each material. In each bin, acceptance is given by the formula:

$$\text{Acceptance} = \frac{\Xi^- \text{ Signal}}{\text{Number of } \Xi^-\text{'s Generated}} \ .$$

The statistical error on the acceptance related to the number of events generated is calculated with the formula:

$$\text{Statistical Error on Acceptance} = \frac{\text{Error on } \Xi^- \text{ Signal}}{\text{Number of } \Xi^-\text{'s Generated}} \ .$$

When calculating the number of Ξ^-'s generated, the events are weighted. The weight is calculated as described in the previous section based on the truth table x_F, truth table p_T^2, and truth table material. The weighting function derived for downstream beryllium events is used for upstream beryllium events.

$$\text{Number of } \Xi^-\text{'s Generated} = \sum \text{Weights} \ .$$

The sum is over all Ξ^- particles generated with truth table x_F and truth table material within the bin limits.

The Ξ^- signal is calculated from the candidate Ξ^-'s that pass the cuts. The acceptances are calculated for each set of cuts. The cuts used to derive the acceptances must be identical to the cuts used on the data. The Ξ^- signal and error are calculated like the data signal and error (see Section 6.3 for a description of sideband subtraction). The simulation is weighted by the functions described in the previous section. The weights are calculated based on the reconstructed x_F, reconstructed p_T^2, and truth table material type. Upstream beryllium events are weighted with the weighting function derived for downstream beryllium events. An acceptance is calculated in each bin of x_F and material. Events are placed in bins based on reconstructed material and reconstructed x_F. This automatically includes a correction for vertex errors and x_F errors in the acceptances.

The acceptances for the largest set of events (x_F from -0.09 to 0.15, all p_T, both charges) are shown in Figure 7.5. These are the acceptances used to determine the atomic mass dependence. The tungsten acceptances are lower than the beryllium acceptances for all x_F bins. This can be seen more clearly in a plot that averages the acceptances over all x_F. Figure 7.6 shows the acceptances as a function of material (averaged over all x_F bins).

Figure 7.7 shows acceptance as a function of p_T. The acceptance is slightly smaller at low p_T.

Figure 7.8 shows acceptance as a function of NTRKD23. NTRKD23 is defined as the number of charged tracks that exist at any point in the second or third drift chamber assemblies (D2 or D3). This is based on the truth table. It excludes Ξ^- tracks and any tracks that come from Ξ^- decay. The acceptance has a strong dependence on multiplicity.

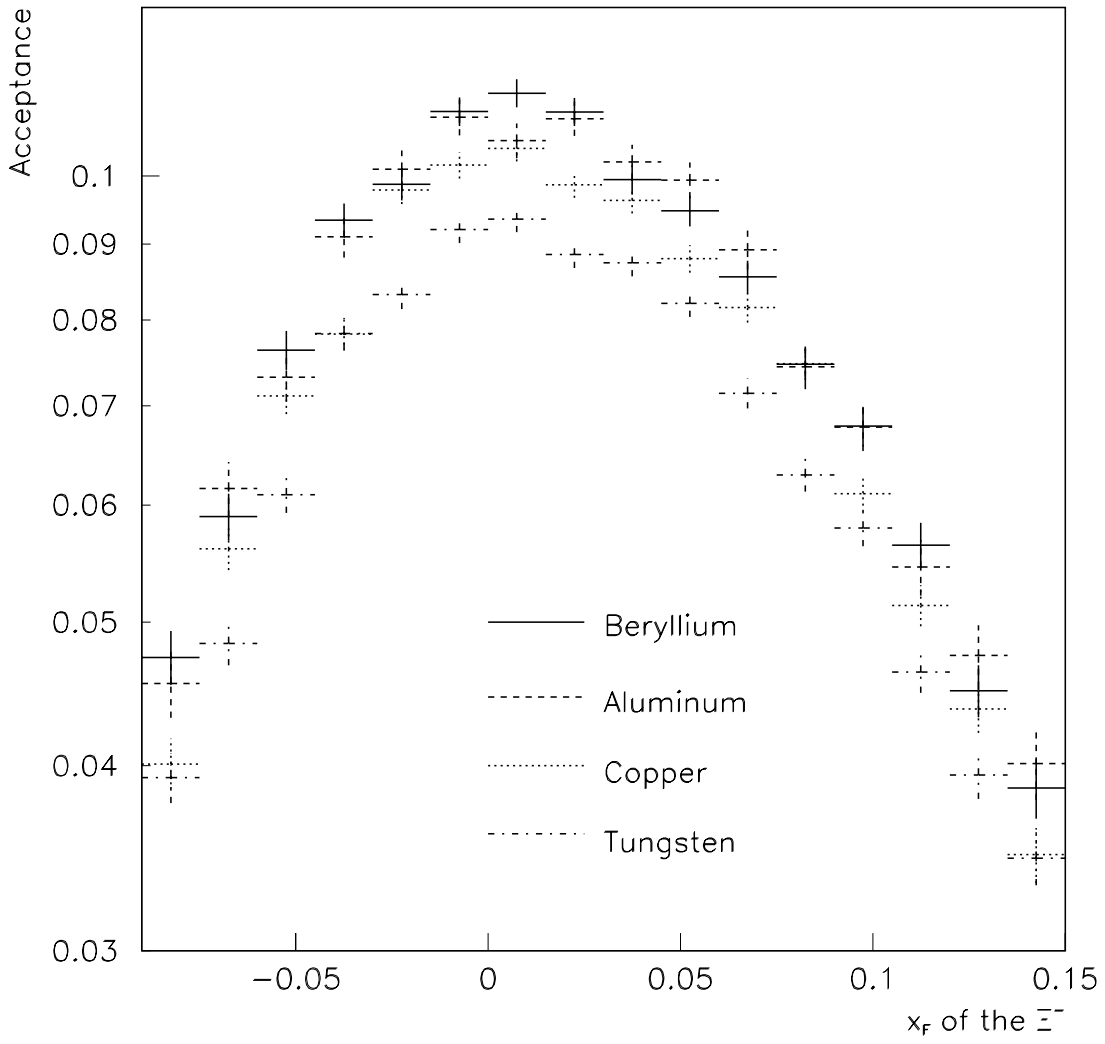

Figure 7.5: Acceptances used in the atomic mass dependence calculation. The acceptances are calculated separately for each target material in x_F bins of width 0.015.

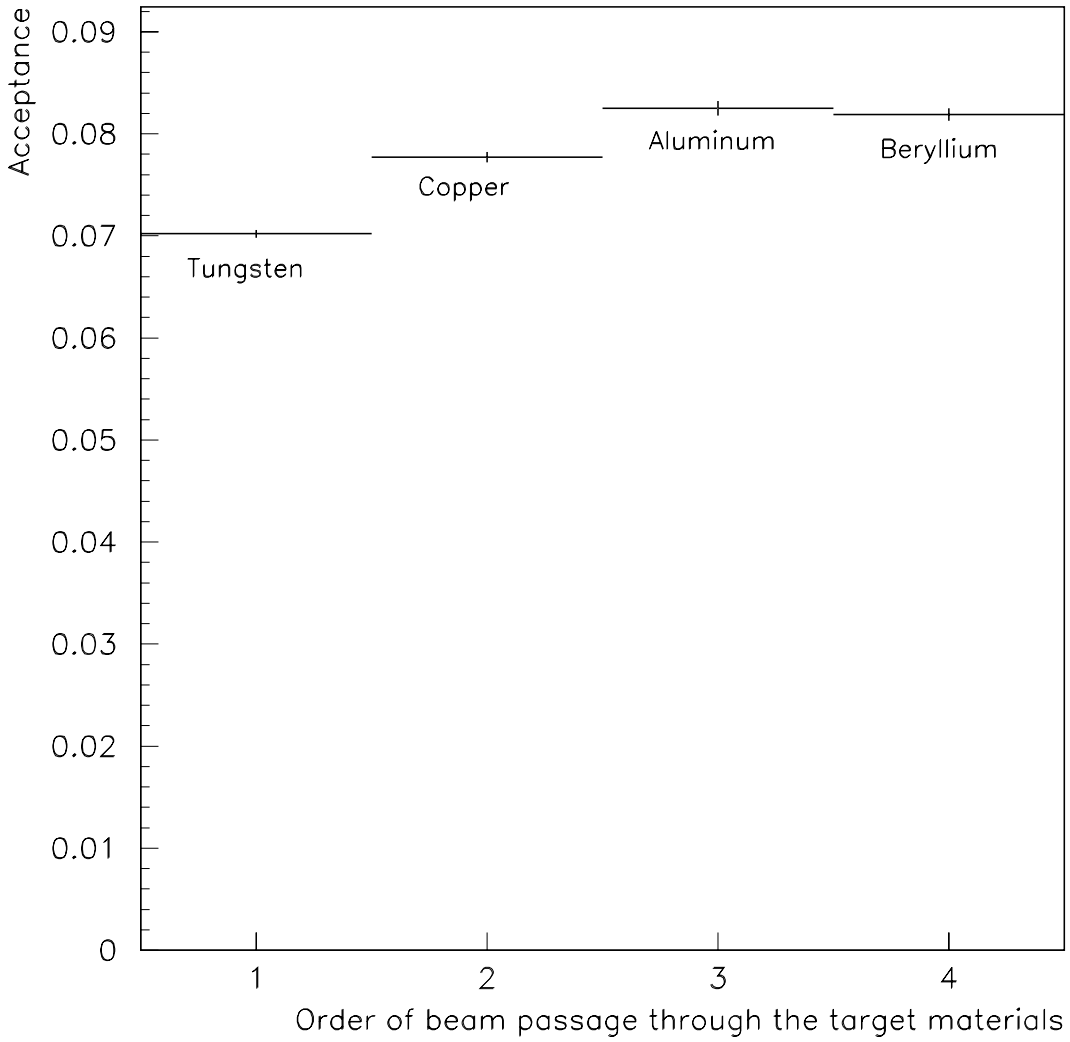

Figure 7.6: Acceptance as a function of target material (averaged over all bins of x_F).

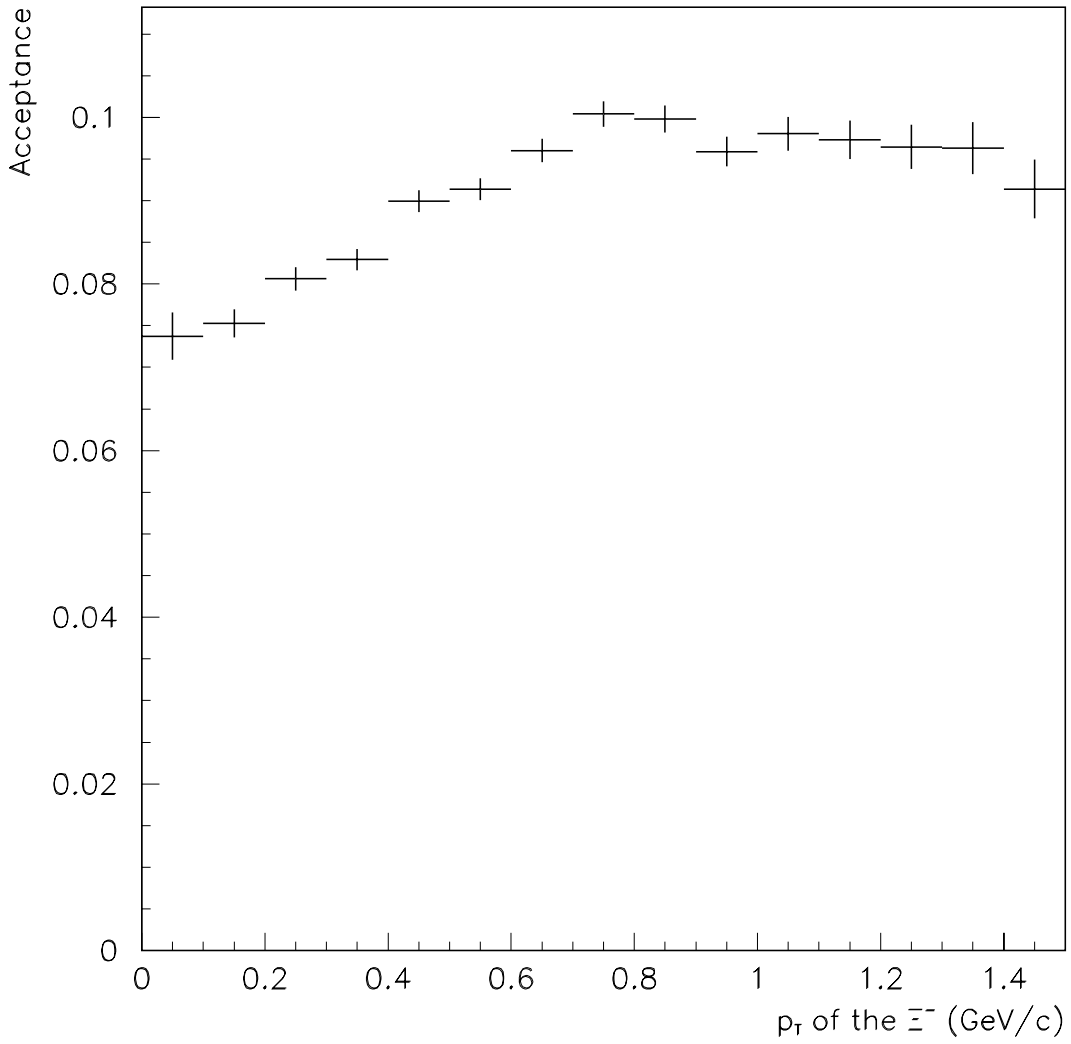

Figure 7.7: Acceptance as a function of p_T (transverse momentum of the Ξ^-). Acceptances are averaged over all bins of x_F.

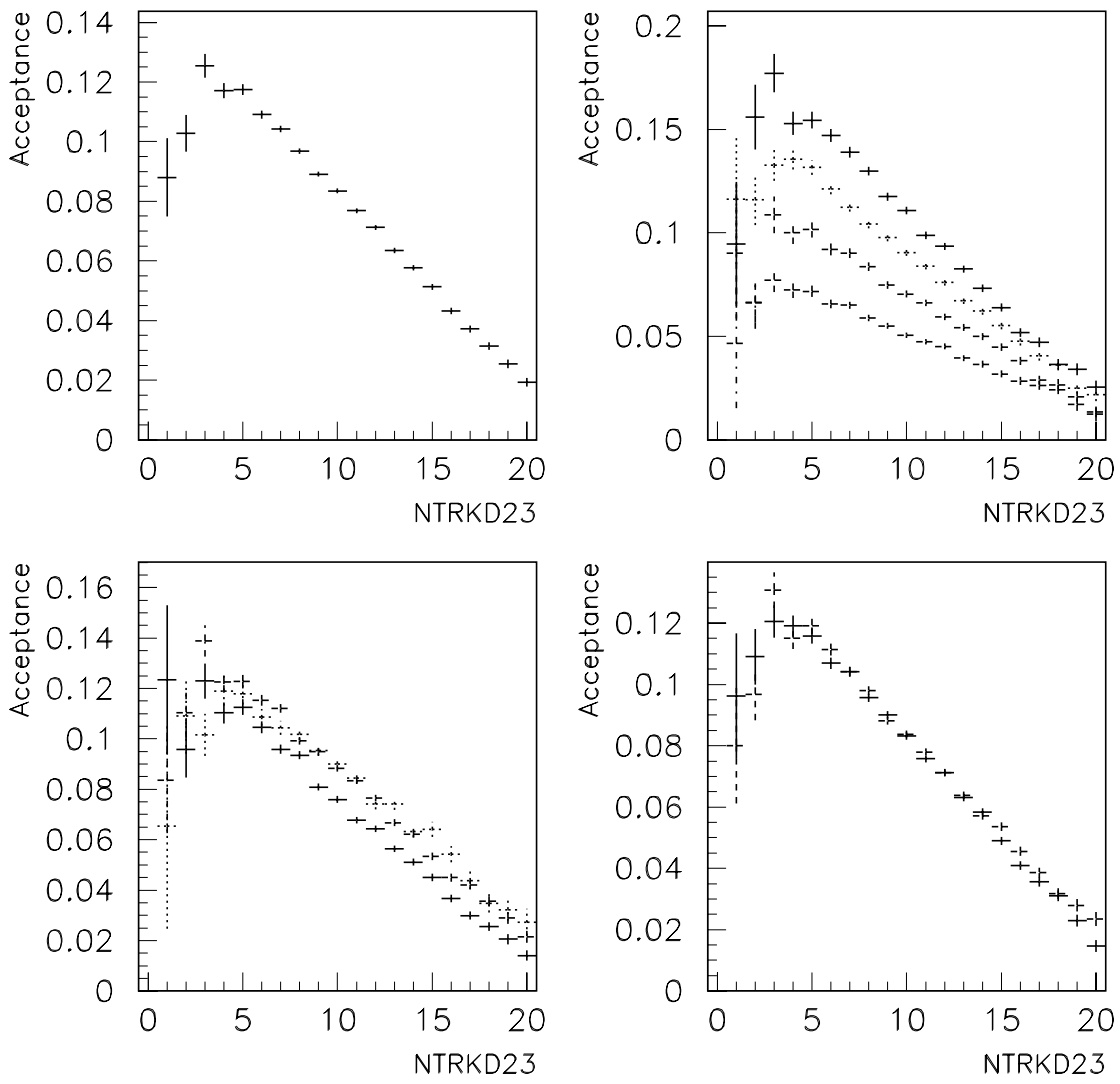

Figure 7.8: All of the plots show acceptance as a function of NTRKD23. NTRKD23 is defined as the number of charged truth table tracks that pass through drift chamber assemblies D2 and/or D3. The Ξ^- track and the tracks of all particles resulting from Ξ^- decay are excluded from the total. The top left plot includes events for x_F from -0.09 to 0.15 and all p_T. The top right plot shows the same function calculated in four different bins of x_F. The bottom left shows the same function for three different bins of p_T. The bottom right shows the same function separately for the Ξ^- and $\overline{\Xi}^+$. The trend is the same in every subsample. The acceptance decreases rapidly as the multiplicity increases.

7.4 Why Acceptance Varies as a Function of Target Material

There are four significant factors that cause the acceptance to vary as a function of target material.

1. The Geometry of the Detector
2. Primary Vertex Errors
3. Events Failing to Reconstruct
4. Variations in Tracking Efficiency in Reconstruction

All four of these factors lower the acceptance of tungsten target events relative to the acceptance of beryllium target events.

Table 7.1 shows quantitative estimates of the impact of each factor on the acceptance. It shows the fractional difference between the tungsten and beryllium acceptances. The text of this section gives detail about the sources for the estimates in the Table 7.1.

The studies related to detector geometry are discussed in detail in Section A.4. The most important geometric feature is the requirement that the Ξ^- decay occur downstream of the silicon microstrip detector. This is necessary, because the track of the pion from Ξ^- decay is required to be a drift chamber track. From the table, one can see that the geometric effect is more significant at lower x_F.

The primary vertex errors are discussed in Section 6.2.2. The vertex effects are about the same in all the different subsamples.

Reconstruction fails when a fatal error occurs in the reconstruction program. When a fatal error occurs, NTRK is set to zero and processing for the event stops. In the simulation, almost all failures were caused by triplet array overflows (not true for data). The fraction of events that failed to reconstruct is:

1. Tungsten 5.16%

2. Copper 2.88%

3. Aluminum 2.12%

4. Beryllium 1.93%

Statistical errors for these values are of the order of $\pm 0.03\%$. These are the fractions of generated events. I assume this percentage affects the acceptance by the same percentage. These failures will cause roughly a 3% fractional difference between the acceptance for tungsten and the acceptance for beryllium (5.16 - 1.93 = 3, approximately). The numbers quoted above are for the dataset with x_F from -0.09 to 0.15 and all p_T. This study was repeated in bins of x_F, bins of p_T, for $\overline{\Xi}^+$'s, and for Ξ^-'s.

Tracking efficiency causes the largest change in acceptance. A detailed study of tracking efficiency is described in Section A.3.3. One can see from Table 7.1 that the effect is most significant at low p_T. This is because the track densities are higher near the beamline.

One additional study was done. 400,000 events were generated with the simulation modified so that the events from all target materials had the same average multiplicity. For this simulation, the variation in acceptance related to tracking efficiencies and events failing to reconstruct vanishes. These two factors are driven solely by the multiplicity of the events in the simulation.

Table 7.1 is based solely on the simulation. It does not consider that the simulation is not perfect. One needs to use data and make comparisons to determine the systematic errors on the acceptances. The next chapter describes how the acceptances are used on the data to derive the atomic mass dependence results. Then the first appendix discusses systematic errors on the acceptances.

Dataset	Complete Simulation	Geometry	Vertex Errors	Reconstruction Failure	Tracking Efficiency
x_F -0.09 to 0.15	17%	5%	3%	3%	8%
x_F -0.09 to -0.03	20%	7%	4%	3%	10%
x_F -0.03 to 0.03	21%	7%	2%	4%	8%
x_F 0.03 to 0.09	16%	3%	3%	3%	7%
x_F 0.09 to 0.15	15%	1%	1%	2%	9%
p_T 0.0 to 0.5 GeV	20%	4%	2%	4%	11%
p_T 0.5 to 1.0 GeV	17%	7%	3%	3%	7%
p_T 1.0 to 1.5 GeV	13%	6%	4%	3%	4%
$\overline{\Xi}^+$'s only	17%	5%	3%	3%	9%
Ξ^-'s only	17%	5%	2%	3%	7%

Table 7.1: Study of the variation of acceptance for different target materials. Each row refers to a different dataset. Every entry gives a *fractional* difference in acceptance from tungsten to beryllium. For example, if the tungsten acceptance was 0.08 and the beryllium acceptance 0.10, then the fractional difference would be 25% $((0.10 - 0.08)/0.08)$. The second column is fractional difference calculated by the full simulation. The last four columns show the expected shift from each of the four factors that cause the acceptance to vary. The last four columns are based on approximations as described in the text. These approximations ignore correlations between the different factors. The second column should be a sum of the other four columns. The sum is not exactly equal because of correlations, approximations, and statistical errors. Statistical errors on the quantities are typically $\pm 1\%$ or $\pm 2\%$.

Chapter 8

Atomic Mass Dependence

This chapter ends with the atomic mass dependence results that were published. The body of the chapter describes the last few steps in the calculation.

8.1 Converting Signals to Cross Sections

The formula for the cross section per atom is:

$$\sigma = \frac{(\text{Signal})}{(\text{Acceptance})} \cdot \frac{(\text{Atomic Mass})}{(\text{Density})(\text{Thickness})(N_A)} \cdot \frac{1}{N_{beam}} ,$$

where N_A is Avogadro's number and N_{beam} is the number of beam particles that pass through the target. For the purpose of measuring the atomic mass dependence, one can arbitrarily normalize the cross sections as long as the normalization is consistent for all four materials. In everything that follows, the cross sections are normalized so that the beryllium cross section equals its atomic mass (9.01).

The thickness and density of each target foil were taken from Professor Milburn's original note documenting the target [66]. The beryllium thickness includes only the downstream beryllium foils. The upstream beryllium foils are not used in this analysis. The error on the thickness is taken from the same source. The error on the density is negligible. The atomic mass of each target material is taken from the Particle Data Group [25]. The error on the atomic mass is negligible. See Table 8.1.

	Atomic Mass	Density (g/cc)	Thickness (mm) (summed over all foils of a material)
Tungsten	183.85	19.3	0.383 ± 0.008
Copper	63.55	8.96	0.761 ± 0.003
Aluminum	26.98	2.70	1.261 ± 0.005
Downstream Beryllium	9.01	1.848	2.604 ± 0.025

Table 8.1: Atomic mass, density, and thickness for each target material.

Because the cross sections are all normalized, the absolute value of N_{beam} is not important. The variation of N_{beam} from one target material to the next is important. For a given foil, N_{beam} is proportional to the probability that a beam particle will not have an absorption interaction in any preceding foil. The probability that a beam particle suffers an absorption collision in a foil is

$$\text{Probability} = \sigma_{\text{a}} \cdot \frac{(\text{Density})(\text{Thickness})(N_A)}{(\text{Atomic Mass})} \ ,$$

where N_A is Avogadro's number and σ_{a} is the absorption cross section. The absorption cross sections are interpolated from values in [28] and are listed in Table 8.2. The absorption correction factor used to calculate N_{beam} in the n^{th} foil is defined by:

$$(N_{beam})_n = (N_{beam})_1 \cdot (\text{Factor})_n = (N_{beam})_1 \cdot \prod_{i=1}^{n-1} (1 - \text{Probability}_i) \ .$$

N_{beam} for a given material is approximated as the average of N_{beam} for the foils of that material. The average correction factor for each material is shown in Table 8.2.

The difference in N_{beam} between beryllium and tungsten is only 0.0118 or 1%. It is not necessary to do a detailed error calculation on this. The errors in the

	Absorption Cross Section (mb)	N_{beam} Absorption Correction Factor
Tungsten	1364	0.9983
Copper	624	0.9945
Aluminum	326	0.9899
Downstream Beryllium	140	0.9865

Table 8.2: Absorption cross section and average correction factor for each target material.

calculation are of the order of 10% or less. The error on the cross sections would be 10% times the 1% correction. This is negligible.

There is a second source of systematic error. The particles created in the absorption collisions could interact again and produce Ξ^-'s. The size of this error is a little more difficult to estimate. Ξ^-'s with less than about 8 GeV are outside the x_F range measured in this analysis. Considering this fact and kinematics you come to a conclusion that secondaries with less than roughly 50 GeV are irrelevant. This eliminates the vast majority of particles produced in absorption collisions. π^0's are irrelevant and should carry a substantial fraction of the momentum on average. Even considering these factors, there should be a substantial number of high momentum charged pions that could produce Ξ^-'s. The Ξ^- cross section does not decrease rapidly with momentum (like the charm cross section). A 150 GeV pion could easily produce a Ξ^- in the x_F range. The systematic error is conservatively estimated to be the size of the N_{beam} correction, 1%. In what follows, this is usually called the systematic error related to the flux.

8.2 Signals and Statistical Errors

Table 8.3 shows the Ξ^- signals with no weighting and no acceptance correction. These are shown separately for the minimum bias trigger events and the ET trigger events. One can see the statistical errors on each subsample before the trigger weighted combination is formed. For example, for tungsten in the largest dataset, the statistical error is $29/533 = 0.054 = 5.4\%$ for the minimum bias trigger events. For the ET trigger events, the statistical error is $101/5848 = 0.017 = 1.7\%$.

Table 8.4 shows signals calculated using a weighted combination of minimum bias trigger events and ET trigger events. The top half of the table shows the signals before the acceptance correction. For tungsten in the largest dataset, the statistical error is $362/10038 = 0.036 = 3.6\%$.

The bottom half of Table 8.4 shows the signals after the acceptance correction. The signals are acceptance corrected in bins of x_F of width 0.015. After the acceptance correction, they are summed over an appropriate range of x_F. The errors on the acceptance due to simulation statistics are calculated in each bin of x_F. These errors are then carried through the acceptance correction procedure by standard formulas for propagation of errors. The fractional data and simulation statistical errors are added in quadrature for the division in each bin of x_F, and then the absolute statistical errors on each bin are added in quadrature when the x_F bins are summed. The statistical errors in the bottom half of Table 8.4 include both data and simulation statistical errors. For tungsten in the largest dataset, the statistical error is $5600/142900 = 0.039 = 3.9\%$. The simulation statistical errors increased the error from 3.6% to 3.9%. The error due to simulation statistics is

$$\sqrt{0.039^2 - 0.036^2} = 0.015 = 1.5\% \ .$$

The worst statistics are in the highest x_F bin for aluminum. In that bin, the data statistical error is 12.2% and the overall statistical error is 13.2%. The simulation statistical error is 5.0%.

One can also get the average acceptances from Table 8.4 by dividing an entry in the top half of the table by the corresponding entry in the bottom half. For the largest dataset, the average acceptances are:

Tungsten	7.02%
Copper	7.75%
Aluminum	8.33%
Beryllium	8.17%

Table 8.5 shows the cross sections calculated using the formula discussed in the previous section. They are normalized so that the beryllium cross section is 9.01.

	Tungsten	Copper	Aluminum	Downstream Beryllium
Minimum Bias Trigger				
Largest Dataset	533 ± 29	630 ± 31	348 ± 23	469 ± 27
$\overline{\Xi}^+$ only	212 ± 19	229 ± 19	160 ± 15	195 ± 18
Ξ^- only	321 ± 23	401 ± 24	192 ± 17	274 ± 21
p_T 0.0 to 0.5 GeV	185 ± 18	213 ± 19	127 ± 15	184 ± 18
p_T 0.5 to 1.0 GeV	237 ± 19	293 ± 21	171 ± 15	210 ± 18
p_T 1.0 to 1.5 GeV	94 ± 12	107 ± 12	41 ± 9	61 ± 10
x_F -0.09 to -0.03	95 ± 12	118 ± 13	82 ± 10	96 ± 12
x_F -0.03 to 0.03	225 ± 18	248 ± 19	125 ± 14	168 ± 16
x_F 0.03 to 0.09	145 ± 16	193 ± 17	103 ± 13	139 ± 16
x_F 0.09 to 0.15	69 ± 11	71 ± 11	39 ± 9	67 ± 11
ET Trigger				
Largest Dataset	5848 ± 101	6238 ± 103	3565 ± 77	4828 ± 90
$\overline{\Xi}^+$ only	2520 ± 66	2692 ± 68	1541 ± 51	2117 ± 59
Ξ^- only	3328 ± 76	3546 ± 78	2024 ± 58	2711 ± 68
p_T 0.0 to 0.5 GeV	1721 ± 59	1955 ± 62	1080 ± 46	1600 ± 56
p_T 0.5 to 1.0 GeV	2663 ± 67	2899 ± 69	1717 ± 52	2249 ± 60
p_T 1.0 to 1.5 GeV	1110 ± 41	1086 ± 41	610 ± 30	783 ± 34
x_F -0.09 to -0.03	1034 ± 41	1100 ± 41	634 ± 31	777 ± 34
x_F -0.03 to 0.03	2254 ± 61	2374 ± 62	1277 ± 45	1801 ± 53
x_F 0.03 to 0.09	1768 ± 56	1881 ± 59	1134 ± 44	1566 ± 52
x_F 0.09 to 0.15	792 ± 39	882 ± 40	520 ± 31	683 ± 37

Table 8.3: Raw signals. The signals shown here are not weighted for triggers and not acceptance corrected. The background has been subtracted and accounted for in the statistical error. Only statistical errors are shown. The top half of the table is for minimum bias trigger events and the bottom half is for ET trigger events. The largest dataset contains Ξ^-'s and $\overline{\Xi}^+$'s with x_F between -0.09 and 0.15 and all values of p_T. The other lines show subsets of the largest dataset with the additional cut specified in the first column.

	Tungsten	Copper	Aluminum	Downstream Beryllium
Before Acceptance Correction				
Largest Dataset	10038 ± 362	10884 ± 378	6631 ± 305	9277 ± 375
$\overline{\Xi}^+$ only	4133 ± 230	4421 ± 237	2894 ± 200	4032 ± 253
Ξ^- only	5905 ± 280	6463 ± 294	3737 ± 230	5245 ± 276
p_T 0 to 0.5 GeV	3366 ± 233	3881 ± 249	2182 ± 193	3534 ± 259
p_T 0.5 to 1 GeV	4480 ± 238	5133 ± 253	3342 ± 207	4181 ± 241
p_T 1 to 1.5 GeV	1807 ± 133	1532 ± 122	849 ± 95	1293 ± 111
x_F -0.09 to -0.03	1849 ± 148	1962 ± 156	1560 ± 152	1966 ± 176
x_F -0.03 to 0.03	4089 ± 232	4235 ± 236	2380 ± 181	3311 ± 213
x_F 0.03 to 0.09	2812 ± 196	3317 ± 210	1903 ± 167	2765 ± 207
x_F 0.09 to 0.15	1286 ± 131	1370 ± 137	787 ± 96	1235 ± 146
After Acceptance Correction				
Largest Dataset	142900 ± 5600	140500 ± 5200	79600 ± 3900	113600 ± 5000
$\overline{\Xi}^+$ only	58900 ± 3500	57000 ± 3200	36100 ± 2700	48500 ± 3200
Ξ^- only	84000 ± 4300	83600 ± 4100	43600 ± 2800	65000 ± 3800
p_T 0 to 0.5 GeV	55200 ± 4300	54000 ± 3600	29300 ± 2800	46900 ± 3800
p_T 0.5 to 1 GeV	60100 ± 3400	62600 ± 3400	37900 ± 2500	48700 ± 3200
p_T 1 to 1.5 GeV	22400 ± 1700	18500 ± 1700	9500 ± 1100	14900 ± 1300
x_F -0.09 to -0.03	32100 ± 2700	31100 ± 2600	21900 ± 2300	28100 ± 2600
x_F -0.03 to 0.03	45600 ± 2600	42100 ± 2400	22400 ± 1700	30700 ± 2000
x_F 0.03 to 0.09	36500 ± 2600	38800 ± 2500	20600 ± 1900	30900 ± 2400
x_F 0.09 to 0.15	28600 ± 3100	28400 ± 2900	14600 ± 1900	23900 ± 2900

Table 8.4: Signals before and after acceptance correction. The signals are the weighted combination of minimum bias trigger events and ET trigger events. The top half of the table shows signals that are not acceptance corrected. The bottom half shows signals that are acceptance corrected. These signals are all summed over appropriate x_F bins, but the acceptances are applied to signals in narrow bins of x_F (0.015 wide) before the summation over x_F occurs. The background has been subtracted in bins of x_F before the summation over x_F. Only statistical errors are shown. The largest dataset contains Ξ^-'s and $\overline{\Xi}^+$'s with x_F between -0.09 and 0.15 and all values of p_T. The other lines show subsets of the largest dataset with the additional cut specified in the first column.

	Downstream Beryllium	Aluminum	Copper	Tungsten
Largest Dataset	9.01 ± 0.40	26.6 ± 1.3	55.0 ± 2.0	148.8 ± 5.8
$\overline{\Xi}^+$ only	9.01 ± 0.61	28.2 ± 2.1	52.2 ± 2.9	143.4 ± 8.6
Ξ^- only	9.01 ± 0.53	25.5 ± 1.7	57.2 ± 2.8	153.0 ± 7.9
p_T 0.0 to 0.5 GeV	9.01 ± 0.72	23.7 ± 2.3	51.2 ± 3.4	139.2 ± 10.9
p_T 0.5 to 1.0 GeV	9.01 ± 0.59	29.6 ± 2.0	57.2 ± 3.1	145.9 ± 8.3
p_T 1.0 to 1.5 GeV	9.01 ± 0.80	24.2 ± 2.8	55.1 ± 4.9	176.9 ± 13.5
x_F -0.09 to -0.03	9.01 ± 0.85	29.7 ± 3.1	49.3 ± 4.0	135.1 ± 11.5
x_F -0.03 to 0.03	9.01 ± 0.59	27.8 ± 2.1	61.1 ± 3.5	175.9 ± 10.2
x_F 0.03 to 0.09	9.01 ± 0.69	25.3 ± 2.3	55.8 ± 3.6	139.7 ± 9.9
x_F 0.09 to 0.15	9.01 ± 1.11	23.2 ± 3.0	52.9 ± 5.5	141.7 ± 15.6

Table 8.5: Cross sections. These are arbitrarily normalized so that the cross section of beryllium is 9.01. The largest dataset contains Ξ^-'s and $\overline{\Xi}^+$'s with x_F between -0.09 and 0.15 and all values of p_T. The other lines show subsets of the largest dataset with the additional cut specified in the first column.

8.3 Atomic Mass Dependence Results

Once the cross sections are calculated, they are plotted as a function of the atomic mass of each target. MINUIT is used to fit the function $\sigma_0 A^\alpha$ to the data points. The statistical errors on the cross sections are input to the fitter. The error on the parameter α returned from the fitter is the statistical error on the atomic mass dependence.

Figure 8.1 is a plot of the cross sections versus target atomic mass for the largest dataset. The function $\sigma_0 A^\alpha$ is fit to the data. It is a two parameter fit; the second parameter is α. The result is $\alpha = 0.924 \pm 0.020$ (statistical error only).

The procedure described above was repeated to determine α and the statistical error in all the different subsets of data. Table 8.6 shows the results. It also shows the systematic errors which will be discussed in the first appendix. The table shows the results derived separately for the Ξ^- and $\overline{\Xi}^+$. It shows results derived as a function of x_F and p_T. These results were published. Figure 8.2 shows α as a function of x_F. Figure 8.3 shows α as a function of p_T. Both of these figures compare the results from this analysis with other published results for the Ξ^0 at higher x_F.

When this analysis was started, there were no published measurements of the atomic mass dependence of the Ξ^- cross section. The results from this analysis and a result from WA89 [41] at CERN were published at about the same time. The WA89 results were briefly discussed in Section 3.3. The results reported in this analysis are consistent with the results reported by WA89. In this analysis, α was measured to be $0.924 \pm 0.020 \pm 0.025$. This agrees with WA89 result, 0.931 ± 0.046. One has to add that WA89 had data from $x_F = 0.05$ to $x_F = 0.6$. They extrapolated to calculate α for all $x_F > 0.0$. This analysis measures in the range $-0.09 < x_F < 0.15$. The high x_F data should pull the WA89 data down by a value in the neighborhood of 0.02 or 0.03. Even accounting for this, the results agree within errors.

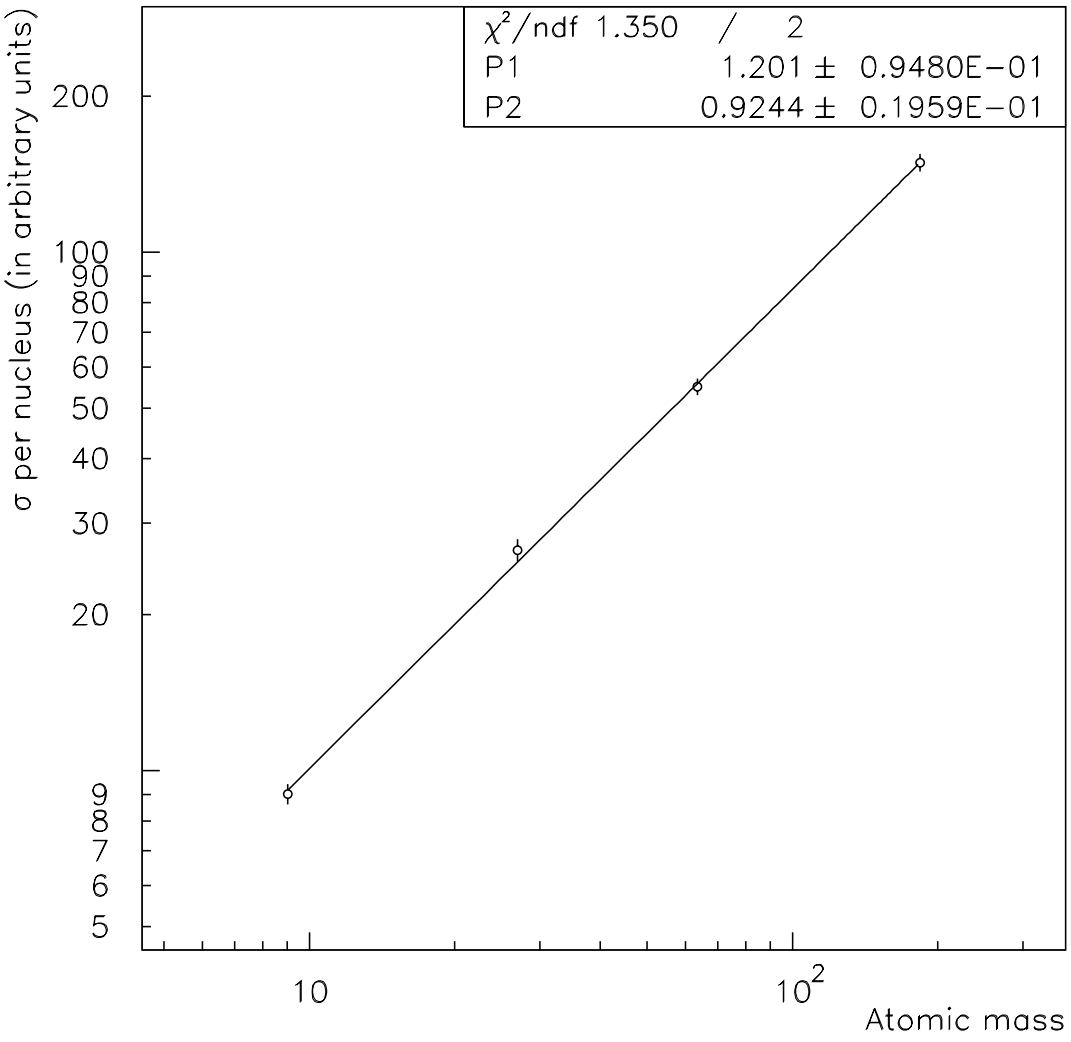

Figure 8.1: The cross sections plotted as a function of the atomic mass of the target nuclei. The cross sections are normalized to force the beryllium cross section to be 9.01. This is for the largest dataset (Ξ^- and $\overline{\Xi}^+$, x_F -0.09 to 0.15, all p_T). The function $\sigma_0 A^\alpha$ is fit to the data. It is a two parameter fit where σ_0 is P1 and α is P2. The fit is done with MINUIT (in manual mode, the fit converged, and HES was called to calculate the errors).

	The Value of α in $\sigma = \sigma_0 A^\alpha$
Largest Dataset	$0.924 \pm 0.020 \pm 0.025$
$\overline{\Xi}^+$ only	$0.905 \pm 0.028 \pm 0.025$
Ξ^- only	$0.939 \pm 0.026 \pm 0.025$
p_T 0.0 to 0.5 GeV	$0.906 \pm 0.041 \pm 0.035$
p_T 0.5 to 1.0 GeV	$0.913 \pm 0.028 \pm 0.022$
p_T 1.0 to 1.5 GeV	$0.988 \pm 0.041 \pm 0.020$
x_F -0.09 to -0.03	$0.881 \pm 0.042 \pm 0.025$
x_F -0.03 to 0.03	$0.981 \pm 0.029 \pm 0.025$
x_F 0.03 to 0.09	$0.910 \pm 0.034 \pm 0.025$
x_F 0.09 to 0.15	$0.918 \pm 0.056 \pm 0.025$
Minimum Bias Triggers Only	$0.942 \pm 0.026 \pm 0.025$
Early runs (before 1451)	$0.941 \pm 0.028 \pm 0.025$
Late runs (after 1450)	$0.909 \pm 0.026 \pm 0.025$
Systematic errors not estimated for the rest.	
ET triggers only	0.97 ± 0.01
Minimum Bias Triggers Failing ET	0.87 ± 0.04
Minimum Bias Triggers Passing ET	1.00 ± 0.03
SMD Pion Events	0.93 ± 0.06
Extra events, SMD $\overline{\Xi}^+/\Xi^-$ track	0.93 ± 0.05
Primary events with SMD $\overline{\Xi}^+/\Xi^-$ track	0.92 ± 0.02

Table 8.6: The atomic mass dependence as measured by α. The largest dataset contains Ξ^-'s and $\overline{\Xi}^+$'s with x_F between -0.09 and 0.15 and all values of p_T. The other lines show subsets of the largest dataset with the additional cut specified in the first column. Except for the last three lines, these are derived from events that pass the primary cuts for 3 drift chamber track candidates. SMD tracks are used in the measurements on the last three lines. For SMD pion events, an SMD track is used for the pion from the Ξ^- decay. Extra events are the one that fail the primary cuts but have an SMD track for the Ξ^- and pass looser cuts. Primary events pass the primary cuts and also have an SMD Ξ^- track. Except where indicated otherwise, these represent the weighted combination of ET and minimum bias trigger events. Statistical errors are shown first, then systematic errors. The systematic errors are not estimated for the last six datasets.

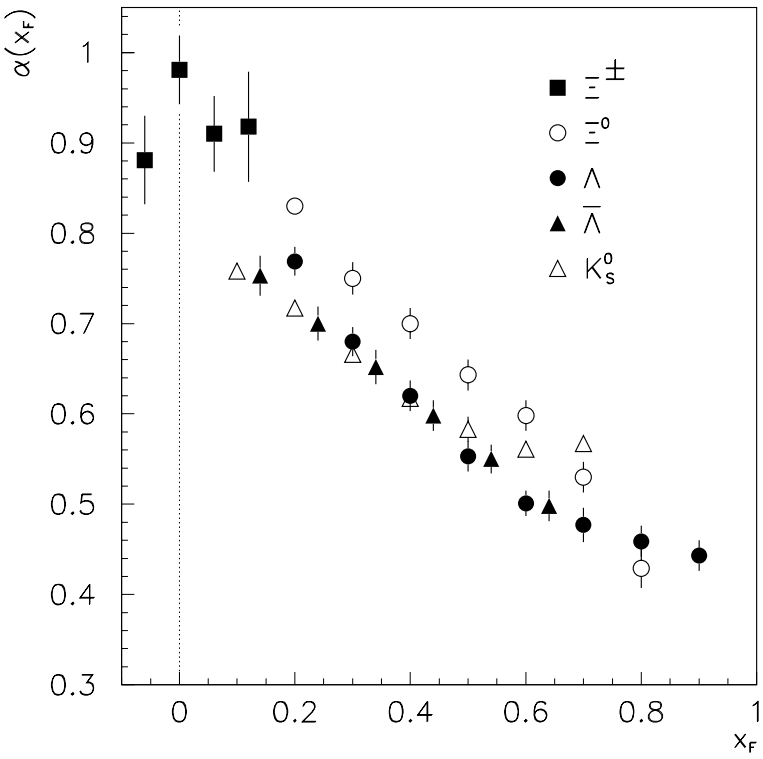

Figure 8.2: The exponent α in $\sigma = \sigma_0 A^\alpha$ as function of x_F. The Ξ^- data are from this analysis. Other data are from Figure 33 in Ref. [34]. The Ξ^- data points line up well with the Ξ^0 data measured previously at higher x_F. One expects $\alpha(x_F)$ to reach a maximum value near the dotted line at $x_F = 0$. Note that the Ξ^- points are based on 250 GeV/c π^- beam data. The Ξ^0 and Λ points are based on 400 GeV/c proton beam data. The $\overline{\Lambda}$ and K^0_S points are based on 300 GeV/c proton beam data.

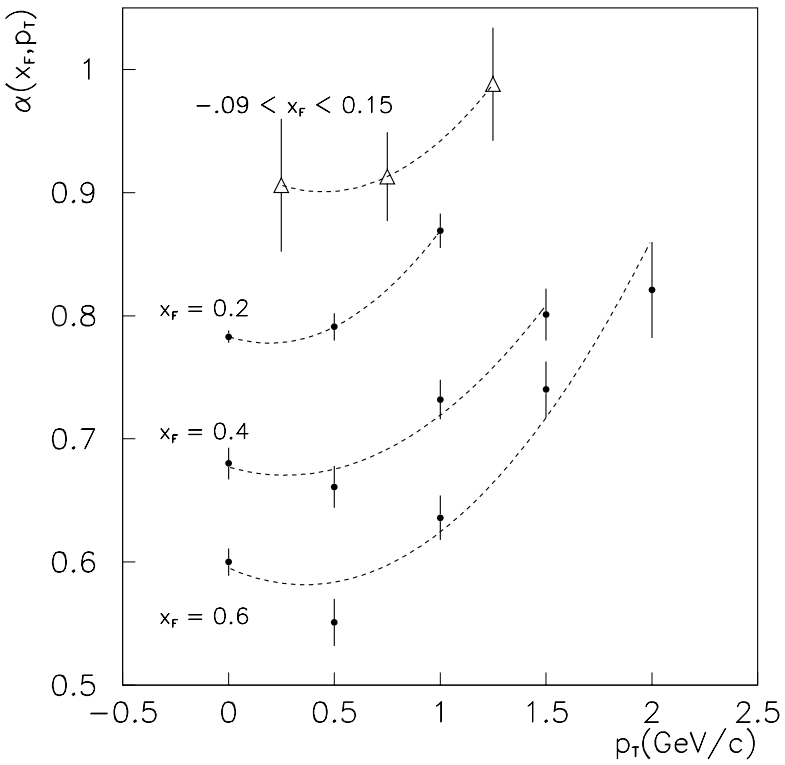

Figure 8.3: The exponent α in $\sigma = \sigma_0 A^\alpha$ as a function of p_T. The triangles show α measured in this analysis for the Ξ^- near $x_F = 0$. The solid dots show α for the Ξ^0 inclusive cross section measurements. The Ξ^0 data are from Figure 31 in Ref. [34]. The lines are drawn to guide the eye to the points corresponding to each value of x_F. The Ξ^- data is consistent with the trend in the Ξ^0 data. Note that the Ξ^- points are based on 250 GeV/c π^- beam data. The Ξ^0 points are based on 400 GeV/c proton beam data.

In addition, the results were derived in several different ways for consistency checks. These results are at the bottom of Table 8.6.

- Results were derived using only minimum bias trigger events with no trigger weighting. This checks the procedure for weighting events based on the trigger. This should give a consistent answer with a larger statistical error. It does.

- Results were derived using data taken chronologically in the first half of the experiment and then separately for the second half. The results are consistent.

- Results were derived using only the ET trigger events, then only using minimum bias events that failed the ET (transverse energy) cut in the ET trigger, and then only using minimum bias events that passed the ET cut in the ET trigger. These results show the bias that the ET cut creates in the ET trigger data. Note that the ET cut is not simulated, so the acceptances used in the these calculations are incorrect. The bias would be larger if the ET cut were properly simulated. These results show the importance of the trigger weighting used to combine the minimum bias and ET trigger events.

- Results were derived using candidates with an SMD (silicon) track for the pion from the Ξ^- decay. Results were also derived for events that had an SMD track that matched the Ξ^- trajectory (separately depending on whether they also passed the primary cuts). The results were all consistent. One might consider combining the signal from the primary cuts with the signal obtained using SMD tracks. The size of the statistical sample could be increased by about 20%. The problem is that the geometrical effects for these SMD tracks are much larger. In addition, there were serious problems reconstructing tracks of particles that decayed before reaching the drift chambers. These problems would add to the systematic error, and they would have to be carefully studied. The small gain in statistics is simply not worth it.

Chapter 9

Conclusion

We have measured the atomic mass dependence of central Ξ^- and $\overline{\Xi}^+$ production using a 250 GeV/c π^- beam. The relative production cross sections for four target materials were fit to the parameterization

$$\sigma = \sigma_0 A^\alpha \ .$$

The result was $\alpha = 0.924 \pm 0.020 \pm 0.025$ in the range $-0.09 < x_F < 0.15$. We find the function fits the data well. α was also measured as a function of x_F and p_T as shown in Figures 8.2 and 8.3.

The results are consistent with the trends seen in other atomic mass dependence experiments. For the dependence of α on x_F, we find that α follows the trend seen in the Ξ^0 data at higher x_F. α continues to increase to a value near 1.0 as x_F approaches 0. For the dependence of α on p_T, we find that α starts a little below 1.0 and starts to rise as p_T rises. This is similar to the behavior for many inclusive cross sections. As discussed at the end of Chapter 3, we expected to find that α had a value between 0.85 and 1.0 for central Ξ^- production. 0.85 is the value of α for central light particle production and 1.0 is the value of α for central charm (D meson) production. This is a measure of the hardness of the production process. This result is expected, because the mass of the Ξ^- is greater than the mass of the

light particles and less than the mass of charm mesons. Our result lies near the center of that range.

The errors on our results and the results from other experiments are large enough that some of the trends are not completely convincing. For example, the difference between α for central charm (D meson) production and α for Ξ^- production is 0.076 ± 0.063 (error is dominated by the error on the charm measurement). Also, the atomic mass dependence for central light particle production is based on extrapolations from limited kinematic regions to the central region. Also, the atomic mass dependence for central light particle production is based on proton beam data, but we compare it to our pion beam data. The errors on the x_F and p_T measurements are also significant (see Figures 8.2 and 8.3). Better measurements for atomic mass dependence for these and other cross sections are needed to make further progress in understanding these trends.

The results presented in this thesis are the first published [1, 2] measurements for the atomic mass dependence of central Ξ^- production. These results will aid in the interpretation of data from experiments using different target materials. We hope that these measurements will also shed light on the behavior of quarks and hadrons inside nuclear matter.

Appendix A

Systematic Errors

This chapter starts by describing the calculation of the systematic error on α from the systematic errors on the cross sections. The second section summarizes the systematic errors on the cross sections. Some of these errors have already been discussed and there are references to the relevant section for each error. Other errors have not been discussed yet. The last sections of this chapter discuss studies which were done to estimate the other errors.

A.1 Converting Errors on the Cross Sections to Errors on the Atomic Mass Dependence

This section describes the last step in the systematic error calculation. Before this step, each source of systematic error has been studied. The error on the tungsten cross section relative to the beryllium cross section has been estimated. It is important to emphasize that this is the relative error. If all the cross sections had the same size error in the same direction, then it would have no effect on the atomic mass dependence parameter α. A good example is the flux. Since all foils lie in the beam simultaneously, the absolute value of the flux is approximately the same in all foils. One does not even need to measure the absolute flux. Errors on the absolute

flux do not contribute to the error on α. On the other hand, interactions in foils cause the flux to vary slightly from one foil to the next. Errors related to this are included in the systematic error estimate.

The systematic errors on the tungsten cross section relative to the beryllium cross section are added in quadrature. In the largest subset of data, the errors are 7.0% (multiplicity), 2.0% (vertex), 2.0% (thickness), 1.0% (flux), and other smaller errors. These are added in quadrature. The overall systematic error on the tungsten cross section relative to the beryllium cross section is 7.6%. An approximation is made that the error in copper is two thirds the error in tungsten (5.1%), and that the error in aluminum is one third the error in tungsten (2.5%). This approximation is reasonable because the average multiplicity of events from copper and aluminum is less than the average multiplicity of tungsten events and closer to the beryllium multiplicity. Therefore, the systematic errors are smaller. To determine the error in α, the cross sections are varied by one sigma and the fit repeated. The cross sections are varied at the same time because the multiplicity errors are correlated. The cross section is varied by 7.6% for tungsten, by 5.1% for copper, and by 2.5% for aluminum. The beryllium cross section is not varied. Figure A.1 shows the fit repeated when the cross sections are increased by these percentages. α is 0.949. Figure A.2 shows the fit repeated when the cross sections are decreased by these percentages. α is 0.898. The systematic error is ± 0.025. The atomic mass dependence is given by $\alpha = 0.924 \pm 0.020 \pm 0.025$ (statistical error then systematic error).

Figures A.1 and A.2 are based on the largest subset of data. For the other subsets of data, the systematic errors are calculated in one of three ways:

- The systematic error is the same as above for the different x_F bins, only $\overline{\Xi}^+$, only Ξ^-, late runs, early runs, and minimum bias trigger events. The error is not recalculated. The systematic errors on the cross sections are the same in all these cases.

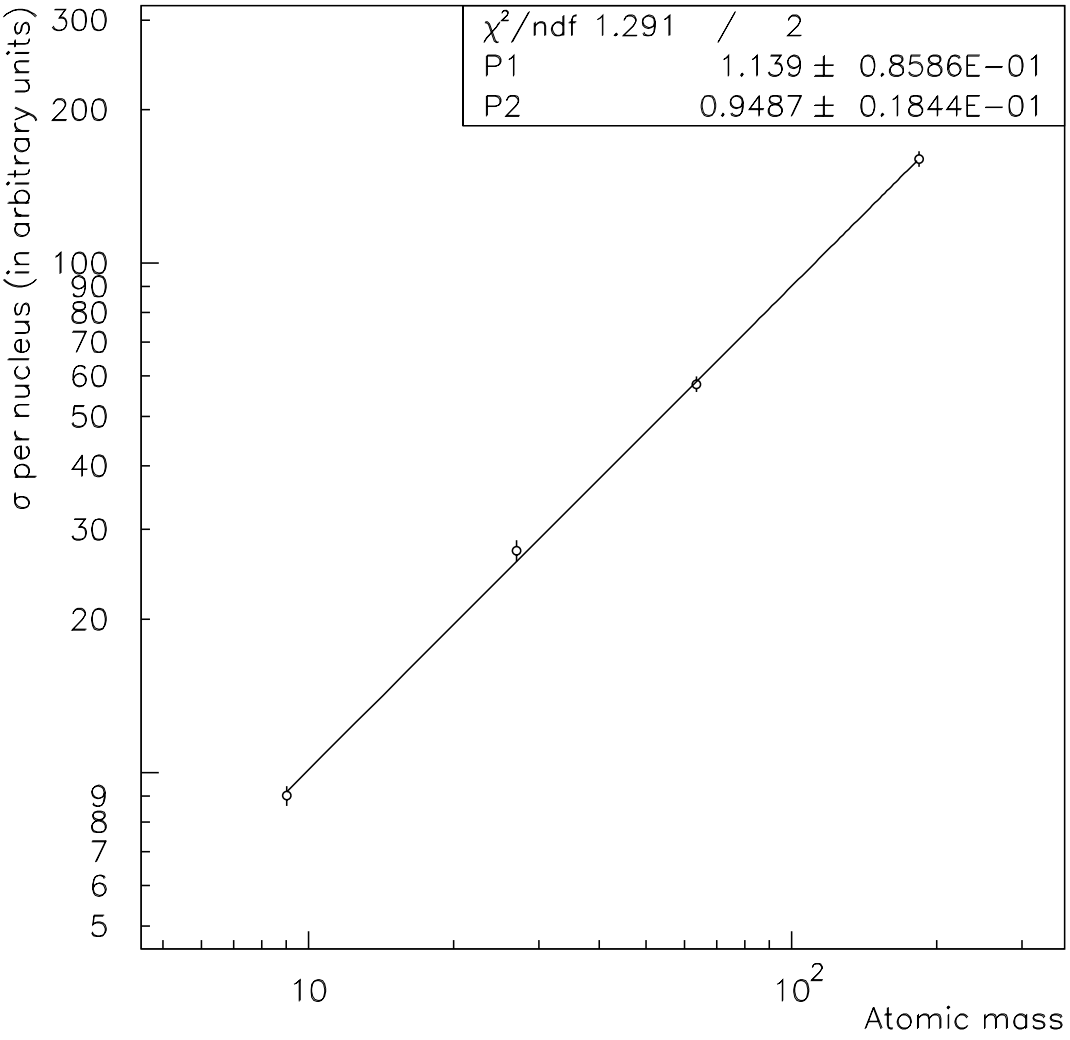

Figure A.1: Repeat of Figure 8.1 with the tungsten cross section increased by 7.6%, the copper cross section increased by 5.1%, and the aluminum cross section increased by 2.5%. This fit is used only for the systematic error calculation.

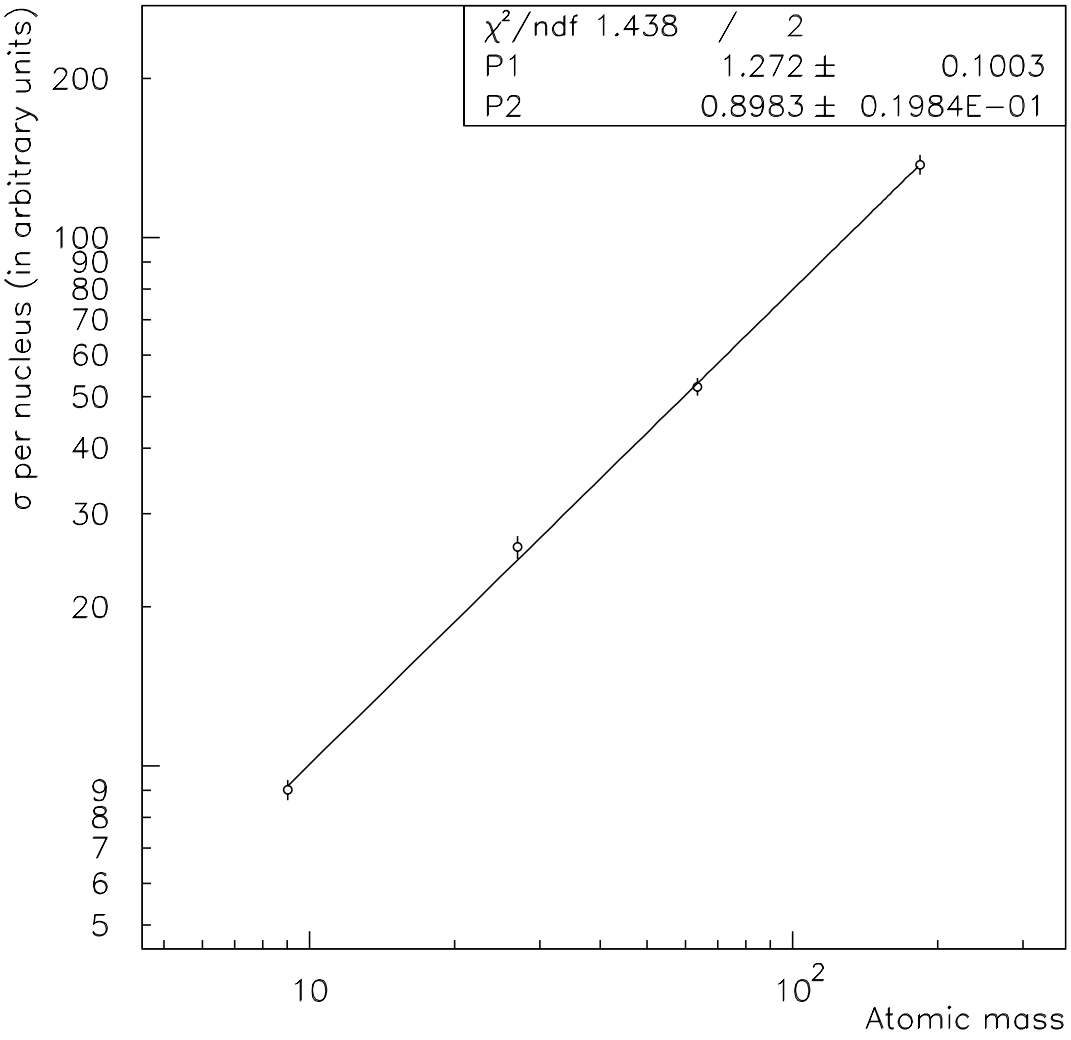

Figure A.2: Repeat of Figure 8.1 with the tungsten cross section decreased by 7.6%, the copper cross section decreased by 5.1%, and the aluminum cross section decreased by 2.5%. This fit is used only for the systematic error calculation.

- For the different p_T bins, the systematic errror is recalculated because the error due to multiplicity is different. For p_T 0.0 to 0.5, the systematic error on the signals due to multiplicity is 9.5%, for p_T from 0.5 to 1.0 it is 6.4%, and for p_T from 1.0 to 1.5 it is 4.5%.

- For the other datasets, no systematic error is quoted. The detailed studies of systematic error were not done for these subsets of the data. None of the results were published. These include datasets with events found using SMD tracks, only ET trigger events, minimum bias trigger events failing ET, and minimum bias trigger events passing ET.

Systematic errors on the atomic mass dependence are shown in Table 8.6 with the results and statistical errors.

A.2 Summary of Errors on the Cross Sections

This section summarizes the errors on the cross sections, not α. The systematic errors listed below were explicitly calculated to be the fractional errors on the tungsten cross section relative to the beryllium cross section. The errors are:

- Multiplicity Effects – 7.0% for most datasets, 9.5% for the set with p_T between 0.0 and 0.5 GeV, 6.4% for the set with p_T between 0.5 and 1.0 GeV, 4.5% for the set with p_T between 1.0 and 1.5 GeV

- Primary Vertex Location – 2.0%

- Target Thickness – 2% for tungsten, less for other materials

- Variation in Flux Due to Inelastic Collisions – 1%

- x_F Weighting – negligible

- p_T Weighting – negligible

- Atomic Mass Dependence Assumed in the Generator – negligible
- Density, Atomic Mass – negligible
- Geometry of Detector – negligible
- Minimum Bias Trigger Correction – negligible
- ET Trigger – zero
- Prescaler Measurement – negligible, included in statistical error
- Errors on the Determination of Signal and Background – negligible

The systematic errors can be compared to the statistical errors which are listed below. These are also fractional errors, but they are not errors on tungsten relative to beryllium. They are simply the fractional statistical errors on the cross sections.

- Data Statistics – 3.5% to 12.2%
- Simulation Statistics – 1.2% to 5.0%
- Combined Statistical Errors – 3.7% to 13.2%

The systematic error related multiplicity for the largest dataset is discussed in Section A.3. For the p_T datasets it is calculated in exactly the same way; the only difference is that the tracking inefficiencies and failure rates are substantially different. Errors related to the location of the primary vertex and the atomic mass dependence assumed in the generator are discussed in Section 6.2.2. Errors related to target thickness and flux are discussed in Section 8.1. Errors related to simulation weighting are discussed on the next page in Table A.1. The triggers and the prescaler measurement are discussed in Section 6.1. The geometry of the detector is discussed in Section A.4. The errors on the determination of signal and background are discussed in Section 6.3.

Simulation Weighting Used to Calculate the Acceptances	Tungsten	Copper	Aluminum	Downstream Beryllium
Normal Weighting	142878	140469	79557	113578
No Weighting	143049	139556	78857	112357
No x_F Weighting	143267	140501	79444	113554
Plus 1 Sigma x_F Weight	142941	140464	79626	113589
Minus 1 Sigma x_F Weight	142748	140475	79409	113563
No p_T Weighting	142657	139525	78969	112380
Plus 1 Sigma p_T Weight	142341	140060	79256	113147
Minus 1 Sigma p_T Weight	143479	140919	79897	114058

Table A.1: The table above is a study of the systematic errors associated with simulation weighting. The values in the table are the acceptance corrected Ξ^- signals. For each line different acceptances are used. The different acceptances are calculated with different weighting functions as noted. The parameters of the different weighting functions have been varied based on the errors on the parameters returned from the fit shown in Figures 7.2 and 7.3. The largest change in the signals as x_F weighting is varied by one sigma is for aluminum with minus one sigma x_F weighting, $(79557 - 79409)/79557 = 0.002 = 0.2\%$, which is negligible. The largest change in signal as p_T weighting is varied by one sigma is for tungsten with minus one sigma p_T weighting, $(143479 - 142878)/142878 = 0.004 = 0.4\%$, which is negligible. These are taken as the systematic errors associated with the weighting functions. These are small compared to other systematic errors and the statistical errors. (A historical note: In early versions of this analysis, the acceptances were calculated in one large x_F bin. This was before anything was ever published. At that time, the systematic error associated with x_F weighting was much larger. Calculating acceptances in x_F bins 0.015 wide eliminated that problem. The error associated with p_T weighting was always small, because the acceptance does not vary much as a function of p_T.)

A.3 Systematic Error Related to Multiplicity

There are two dominant factors that determine the estimate of the systematic error related to multiplicity:

- There is strong evidence that the simulation overestimates multiplicity effects. During reconstruction of simulated data, array bounds overflow much more often than during data reconstruction. There are too many hits, triplets, track segments, and tracks being reconstructed. It is not a small discrepancy, but a large one (see Section A.3.2 for details).

- The distributions in NTRK and IERPM2 indicate that in the data there is a wider gap between the tungsten and beryllium average multiplicities than for the simulation (see Section A.3.1 for details).

These effects are closely related and oppose one another. The two effects are roughly the same size and correlated. For this reason, it makes no sense to try to develop a correction for these problems. The best one can do is to estimate the systematic error.

Table 7.1 details the effects that cause the acceptance to vary as a function of target material. Multiplicity drives the differences related to reconstruction failures and tracking efficiency. The reconstruction failures cause a 3% shift and the tracking efficiency causes an 8% shift. If one just sums the values, the estimate is 11% for multiplicity effects. I should emphasize again, this is the fractional change in the tungsten acceptance relative to the beryllium acceptance.

What is the error on this 11% predicted by the simulation? Three things are known that are relevant. First, it is obvious that the multiplicity must cause the tungsten acceptance to drop compared to the beryllium acceptance. The 11% shift has to be in the right direction. Second, the NTRK and IERPM2 distributions indicate that the difference in multiplicity should be increased by a factor of 2.

Since the acceptance is linear as a function of multiplicity (see Figure 7.8), the difference in acceptance could be twice as large as indicated in the simulation. On the other hand, there is solid evidence that multiplicity effects are overestimated by the simulation.

Unfortunately, this is all that is known for certain. This means we know that the 11% measured in the simulation could really be any value between 0% and 22%. There is no quantitative information to determine where it lies in that range. The rms of this distribution is 22% divided by $\sqrt{12}$. This is 6.4%. For the published paper, a more complicated and less accurate method was used. Instead of dividing by $\sqrt{12}$, a gaussian was fit to the distribution of possible errors. See [3] for a detailed description. This gave an error of 7%, which is what is actually used.

Alternate approaches that involved weighting the simulation to match the data multiplicity and then trying to correct for the discrepancies in the array overflow rates were devised and implemented. These alternate approaches gave roughly the same answer and no real improvement in the systematic error. They just made the analysis complex without delivering any benefits. The information available was simply not adequate to derive reliable corrections.

One might consider other ways to reduce this systematic error. One might go to the raw data and look at the hit information which was not saved on the DST's. Then one might be able to improve the reconstruction algorithms or improve the hit digitization in the simulation. This was not done. It would take many years of effort. Further, it is not clear that one could significantly improve the algorithms the entire collaboration devised for the original reconstruction and digitization.

A.3.1 Comparisons of IERPM2 and NTRK Distributions

NTRK is defined to be the total number of reconstructed tracks. IERPM2 is defined to be the total number of reconstructed tracks with hits in the silicon detector. These are the two best measures of event multiplicity in the reconstructed data. This

section compares the data and simulation using the average values of the variables NTRK and IERPM2.

The average value of IERPM2 is shown in the following table.

	Data	Simulation
Tungsten	9.8 ± 0.16	9.43 ± 0.02
Copper	9.3 ± 0.14	8.85 ± 0.02
Aluminum	8.7 ± 0.18	8.59 ± 0.03
Downstream Beryllium	8.4 ± 0.14	8.70 ± 0.02

The average value of IERPM2 for events generated in tungsten is a little too low, but for beryllium it is a little too high. The difference in average IERPM2 between tungsten and beryllium in the simulation is 9.43 - 8.70 = 0.73. In the data, the difference in IERPM2 is 9.8 - 8.4 = 1.4. The difference in multiplicity is nearly twice as large in the data. The situation is similar for NTRK.

The average value of NTRK is shown in the following table.

	Data	Simulation
Tungsten	19.3 ± 0.3	21.3 ± 0.04
Copper	18.2 ± 0.2	20.4 ± 0.04
Aluminum	17.1 ± 0.3	19.8 ± 0.05
Downstream Beryllium	16.1 ± 0.2	19.8 ± 0.04

The average value of NTRK is significantly higher for the simulation than the data for all materials. This contradicts the information from the IERPM2 averages. It is not known why this is true. One possibility would be that the digitizer is placing the drift chamber hits incorrectly, or maybe the hit clusters are too large. There are a lot of other possibilities. According to IERPM2 the overall multiplicity is about right, but according to NTRK the simulation multiplicity is too high.

The difference in average NTRK for the data between tungsten and beryllium is

$19.3 - 16.1 = 3.2$; for simulation $21.3 - 19.8 = 1.5$. The difference is twice as large in the data (NTRK is similar to IERPM2 in this regard).

The primary reason weighting functions were not used to correct the simulation multiplicity distributions was given in the last section. There is a second reason. The discrepancy between the IERPM2 distributions and the NTRK distributions leaves one suspicious that both are significantly wrong. If the distributions are wrong, weighting could do as much harm as good. Further, it is not clear whether to weight based on NTRK or IERPM2. Both weights have nearly the same effect on the difference between tungsten and beryllium acceptances, but the weights themselves are very different. Weighting both ways was tried, discussed at collaboration meetings and rejected. These studies did yield an additional conclusion. Even with multiplicity weighting applied, the discrepancy between the data and simulation reconstruction error rates was large. These error rates are the subject of the next section.

A.3.2 Reconstruction Errors

There is one other variable saved in the reconstructed data that contains multiplicity information. This variable is called NUMERR. There are 22 bits in NUMERR. Each bit tells whether a certain error occurred while the event was being reconstructed. Most of the errors are related to overflows of the fixed size arrays that hold the information used during track reconstruction and the final track reconstruction results. These errors are strongly related to multiplicity. Table A.2 shows the percentage of Ξ^-'s that come from events with reconstruction errors for both simulation and data.

Errors 1 – 4 and errors 6 – 10 are not shown in Table A.2, because they are always fatal. When a fatal error occurs, NTRK is set to zero and reconstruction stops for that event. Events with NTRK equal to zero never pass the Ξ^- cuts. They could never show up in the table. Event reconstruction continues if a nonfatal error occurs. For example, if the D2 segment array overflows, the reconstruction code

stops making D2 segments and moves on to the next reconstruction step (D2 is the second drift chamber assembly).

Table A.2 shows several discrepancies between data and simulation. The largest discrepancy is for error 17. This error is for overflow of the D2 segment arrays for tracks that originate in D2.

The final reconstructed tracks are loaded into arrays in a specific order. Tracks with hits in D3 and D4 are loaded first. These rarely overflow the track arrays. The track arrays start to overflow when tracks with hits only in D1 and D2 (not D3 or D4) are added. Error 20 show these overflows. Here again, the simulation has more errors than the data.

Error 11 is for triplet array overflows in subassembly 4 of D2. This error also occurs more frequently in the simulation than in the data. If the triplet array overflows in D3 or in the first 3 subassemblies of D2, then error 9 or 10 occurs. These are fatal. It is difficult to study these events, because NTRK is zero. They do not pass Ξ^- cuts.

Table A.3 shows the rates of the errors related to reconstruction failures. The rates are based the set of all minimum bias data events and the set of all simulated events. It is difficult to compare data to simulation, because the simulation does not include background. The minimum bias data does. But this is the only simple way to study fatal errors where NTRK is 0.

The vast majority of the reconstruction failures for simulation are due to error 10. Errors 9, 10, and 11 all relate to overflows of the same array that holds the triplets (position determined from 3 drift chamber planes with U, V, and X views). The triplet array is filled from the D3 subassemblies first, then the first 3 subassemblies of D2, and then the last subassembly of D2. If there is an overflow for the last subassembly of D2 (error 11), it is not fatal. For both data and simulation, error 11 occurs more often than errors 9 and 10 (see Table A.3). Since error 11 is not fatal, it appears in Table A.2 and the comparison of data and simulation is valid. Error

11 occurs much more often in simulation than data. In fact it occurs less than 1% of the time in data. Therefore, the rate of error 10 (the dominant fatal error) is being grossly overestimated by the simulation.

NUMERR bit	Tungsten	Copper	Aluminum	Downstream Beryllium
5. DC Unpack	0.15%/1.2%	0.16%/1.9%	0.23%/2.0%	0.17%/1.5%
11. Triplet Array in D2, Subassembly 4	4.5%/0.5%	3.2%/0.7%	2.5%/0.3%	2.4%/0.0%
Tracking Originating in Drift Chamber 3				
13. D3 Segment Array	0.11%/0.0%	0.08%/0.0%	0.05%/0.0%	0.07%/0.0%
14. D2 Segment Array	0.34%/0.0%	0.27%/0.0%	0.24%/0.0%	0.30%/0.0%
15. D1 Doublet Array	0.54%/0.0%	0.27%/0.2%	0.19%/0.0%	0.15%/0.0%
16. Tracks Array	0.00%/0.0%	0.00%/0.0%	0.00%/0.0%	0.00%/0.0%
Tracking Originating in Drift Chamber 2				
17. D2 Segment Array	25.0%/1.4%	21.3%/1.0%	19.3%/0.9%	19.2%/0.0%
18. D3 Segment Array	1.46%/0.1%	1.57%/0.1%	1.48%/0.1%	1.47%/0.3%
19. Tracks Array with D3/D4 Hits	0.00%/0.0%	0.00%/0.0%	0.01%/0.0%	0.00%/0.0%
20. Tracks Array without D3/D4 Hits	12.6%/10.0%	8.8%/7.2%	7.1%/5.4%	7.1%/4.2%

Table A.2: Percentage of Ξ^-'s from events with reconstruction errors. Except for the top error, all refer to overflow of the array. The percentage to the left of the slash is for simulation. The percentage to the right of the slash is data. This is a comparison of like quantities. The two numbers would be equal if the simulation were perfect. Statistical errors are less than $\pm 0.4\%$ for the simulation and less than $\pm 0.9\%$ for the data.

NUMERR bit	All Events	Events with NTRK = 0
3. Too Many SMD Hits	0.00% / 0.33%	0.00% / 6.73%
5. DC Unpack Errors	0.20% / 2.83%	0.28% / 12.2%
6. Hit Buffer Overflow D1, D2, or D3	0.00% / 0.03%	0.05% / 0.53%
8. Buffer Overflow in REGUN1	0.03% / 0.06%	1.03% / 1.19%
9. Triplet Array Overflow in D3	0.00% / 0.02%	0.32% / 0.32%
10. Triplet Array Overflow in Drift Chamber 2, Assemblies 1–3	2.96% / 0.15%	98.91% / 3.11%
11. Triplet Array Overflow in Drift Chamber 2, Assembly 4	6.17% / 0.30%	

Table A.3: Fraction of events with errors related to reconstruction failure. The middle column is the fraction of all events. The last column is the fraction of events with NTRK equal to zero. The percentage to the left of the slash is for simulation. The percentage to the right of the slash is for data. This is not a comparison of like quantities. If the simulation was perfect, the numbers would still not be equal. For simulation, this is a percentage of all events generated. All events contain a Ξ^-. For data, this is a percentage of all minimum bias events. This is the best one can do, because no tracking is information saved when reconstruction fails. See the text for the conclusions one can reach using the table. The statistical errors on these percentages range from $\pm 0.01\%$ to $\pm 0.12\%$. Note errors $1-4$ and $6-10$ are always fatal. Error 5 is only occasionally fatal. Error 11 is not fatal, but it is shown because it is related to errors 9 and 10. Errors 1, 2, 4, and 7 never occur in the data or simulation.

A.3.3 Track Reconstruction Efficiency

The effect of the tracking efficiency on the acceptances dominates the systematic error estimate (see Section A.3). The result was shown (the last column of Table 7.1), but the calculation of the tracking efficiency was never described. This section describes the details of the measurement of the tracking efficiency.

Start with an ntuple with entries for every Ξ^- generated. Then look in the truth table information and find the tracks of the two pions and the proton that come from Ξ^- decay. Then look in the reconstructed track arrays to see if there are reconstructed tracks that match the truth table tracks.

Tracking efficiency is defined as the fraction of truth table tracks that are reconstructed. Here we want to study only the tracks of the Ξ^- daughters that hit the detector planes. We want to isolate the measurement from other effects so we only look at Ξ^-'s that pass the following requirements.

- The event reconstructs. NTRK is not zero.
- The two pions and the proton have truth table tracks that begin before z = 153 cm and end after z = 500 cm. The tracks exist at D1 and D2.
- The Ξ^- decays after z = 11 cm.
- At Z = 0 cm, the X and Y intercepts of the truth table tracks are less than 7.999 cm.
- The truth table x_F of the Ξ^- is between -0.09 and 0.15.

Unfortunately, the X and Y positions of the tracks at the drift chambers are not saved in the truth table. Otherwise, we would require that the tracks hit the sensitive regions of D1 and D2. This effect was studied separately (not described here). It has no dependence on target material. It does lower the efficiency. Roughly

x_F of Ξ^-	Pion from the Ξ^- (GeV)	Pion from the Λ (GeV)	Proton (GeV)	Angle (milliradians)
-.09 to -.06	.07	.08	.35	7.7
-.06 to -.03	.08	.09	.4	7.1
-.03 to .00	.10	.10	.5	6.3
.00 to .03	.10	.11	.65	5.5
.03 to .06	.11	.14	.9	4.9
.06 to .09	.12	.15	1.3	4.5
.09 to .12	.14	.17	1.5	4.0
.12 to .15	.15	.18	2.0	3.5

Table A.4: Cuts used when matching reconstructed and truth table tracks. The cuts are different in different bins of x_F. The middle three columns show the maximum allowed difference between the total momentum of the truth table track and the reconstructed track. The last column shows the maximum allowed difference in angle, which is the same for all three daughters.

10% of the tracks are outside the sensitive areas of the planes or in the drift chamber hole near the beam.

A reconstructed track matches a truth table track if the following criteria are met.

- The reconstructed track must have only drift chamber hits (no silicon hits). It must include hits in D1 and one drift chamber past D1.
- The two tracks must have the same charge.
- The position of the two tracks at z = 0 must match within 1.4 cm for the pions and 0.9 cm for the proton.
- The total momentum must match within certain values. These values are different for each particle. These values are also different for different bins of x_F of the Ξ^-. See Table A.4.
- The angle between the truth table and reconstructed track must match within the limits shown in Table A.4.

The results of these tracking efficiency studies are shown in Table A.5.

	Tungsten	Copper	Aluminum	Beryllium	Ratio
All 3 Tracks	0.2495	0.2699	0.2722	0.2686	1.077
Λ Pion Track	0.6054	0.6261	0.6267	0.6317	1.043
Proton Track	0.6218	0.6331	0.6420	0.6358	1.023
Ξ^- Pion Track	0.6173	0.6417	0.6362	0.6427	1.041
x_F -0.09 to -0.03	0.2137	0.2343	0.2385	0.2357	1.103
x_F -0.03 to 0.03	0.2838	0.3071	0.3102	0.3074	1.083
x_F 0.03 to 0.09	0.2651	0.2827	0.2905	0.2829	1.067
x_F 0.09 to 0.15	0.1968	0.2103	0.2144	0.2141	1.088
p_T 0.0 to 0.5	0.2281	0.2517	0.2523	0.2525	1.107
p_T 0.5 to 1.0	0.2653	0.2857	0.2900	0.2841	1.071
p_T 1.0 to 1.5	0.2632	0.2781	0.2842	0.2734	1.039
$\overline{\Xi}^+$ only	0.2455	0.2654	0.2712	0.2668	1.087
Ξ^- only	0.2535	0.2746	0.2732	0.2704	1.067

Table A.5: Tracking efficiency. The top four lines of the table are for the dataset with x_F from -0.09 to 0.15 and all p_T. The top line is the efficiency for all three tracks to reconstruct. The next three lines show the efficiencies for the individual tracks. All the rest of the entries in the table are the efficiencies for all three tracks to reconstruct. The efficiencies are calculated from several other subsets of data. Statistical errors on these efficiencies range .0016 to .0064. The last column gives the ratio of the beryllium efficiency to the tungsten efficiency. The ratio gives the effect on the acceptance. For example, if the ratio is 1.077, then the tracking efficiency should make the beryllium acceptances 7.7% higher than the tungsten acceptances. Clearly, this is a rough approximation. Just the statistical errors would be 1% or 2% on the 7.7%.

A.4 Systematic Error Related to Detector Geometry

The next section estimates the effect of geometry on the acceptances. It shows that the geometry causes the tungsten acceptances to be roughly 5% lower than the beryllium acceptances (fractionally lower, the absolute difference equals 0.05 x tungsten acceptance). This is primarily driven by the z coordinate of the position of the decays of the Ξ^- and Λ. The simulation should model this very well. If it is just within 10% of correct, the systematic error would be 0.05 x 0.10 = 0.005. This is negligible. As a check, the lifetimes of the Ξ^- and Λ are calculated from the data and the acceptances. The lifetimes agree with the known values.

A.4.1 Estimate of Acceptance Based on Detector Geometry

The acceptances used for the published atomic mass dependence results were calculated using a full Monte Carlo simulation. In this section, the acceptances are estimated by a separate alternate method. This method uses truth table tracks from the generator, not reconstructed tracks. The method uses only the geometry of the detector, the criteria being all three truth table tracks must hit sensitive areas of the drift chamber planes.

There are many crude approximations made in this section. These approximations could easily create 10% to 20% systematic errors on the estimate of acceptance. It is important to keep this in mind as you read this section.

The purpose of this section is to study how the geometry of the detector affects the acceptance. Each different feature of the geometry is studied separately. This both increases our understanding of the detector and serves as a rough check that the simulation is producing a reasonable result.

The most significant results in this section are the geometric acceptances for each target material. For Ξ^-'s with three drift chamber tracks, they are:

Tungsten	0.261 ± 0.002	(Statistical error only)
Copper	0.264 ± 0.002	
Aluminum	0.272 ± 0.003	
Beryllium	0.275 ± 0.002	
(Downstream Be foils only)		

This is a good estimate of the dependence of acceptance on material due to geometry. The acceptance changes by 0.014 from tungsten to beryllium. 0.014 is 5.4% of 0.261.

Table A.6 gives many more details. The table shows each step in the calculation of the geometric acceptances. The table indicates that the z coordinate of the position of the decays is the most important geometric factor in the material dependence of the acceptance. The first column of the table defines the constraints on each subset of Ξ^-'s that is counted. The first column also gives a precise definition of what is in the numerator and denominator of the fractions in the table and the figures.

Figures A.3, A.4, and A.5 show estimated acceptance as function of x_F of the Ξ^-. The first seven histograms show the effect of each individual constraint. In Figure A.5, the geometric acceptances are shown and then compared to the acceptances calculated from the full simulation. The geometric acceptances are much larger, because tracking efficiency and analysis cuts are not modeled in the geometric acceptances.

	Tungsten	Copper	Aluminum	Beryllium
TOTAL - number of Ξ^-'s generated	89829	81116	42580	62633
L153 - Λ decay before z = 153 cm	42918	38191	20160	29122
C11 - Ξ^- decay after z = 11 cm	71549	65651	35006	52308
DEC - both the above constraints.	29213	26688	14477	21394
D1 - above constraints and all three tracks hit the sensitive area of drift chamber 1.	28422	26032	14124	20883
D12 - above constraints and all three tracks hit the sensitive area of drift chamber 2.	24959	22804	12324	18369
Z0 - above constraints and all three tracks have xy intercepts at z = 0 of less than 8 cm.	23795	21737	11747	17483
HOLE - above constraints and any one track hits the hole in either drift chamber.	305	292	158	242
L153/TOTAL	0.478	0.471	0.473	0.465
C11/TOTAL	0.797	0.809	0.822	0.835
DEC/TOTAL	0.325	0.329	0.340	0.342
D1/DEC	0.973	0.975	0.976	0.976
D12/DEC	0.854	0.854	0.851	0.859
1 − Z0/D12	0.047	0.047	0.047	0.048
HOLE/Z0	0.013	0.013	0.013	0.014
Acceptance = (Z0 − HOLE)/TOTAL	0.261	0.264	0.272	0.275
Statistical Error	0.002	0.002	0.003	0.002

Table A.6: Estimate of the geometric acceptance by material. The top half of the table contains a count of the number of Ξ^-'s that pass the criteria defined in the first column. The bottom half of the table contains fractions defined in the first column. The last two lines have the geometric acceptance and its statistical error.

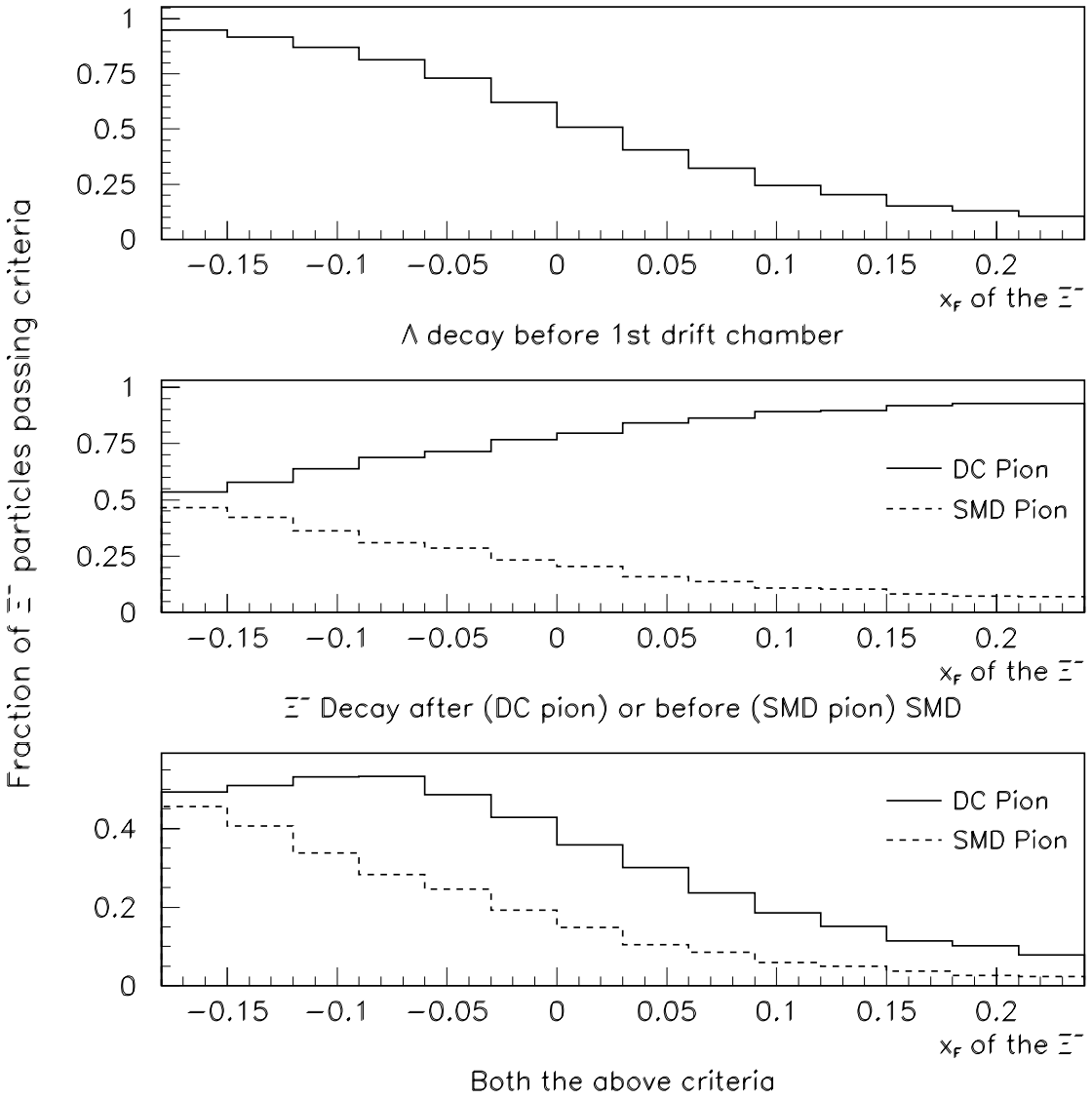

Figure A.3: Effect of the Z coordinates of the decay positions on the acceptance. In all three histograms, the horizontal axis is x_F of the Ξ^-. The first histogram shows the fraction of Λ's that decay before the first drift chamber assembly. The second histogram shows the fraction of Ξ^-'s that decay after (solid line) or before (dotted line) the silicon detector. The last shows Ξ^-'s where both criteria are met. For the main set of cuts, both the Ξ^- and Λ must decay between the silicon detector and first drift chamber assembly to be detected. For the other set of cuts, the pion from Ξ^- decay is assumed to have a track with silicon hits and the criteria for the Ξ^- decay is reversed.

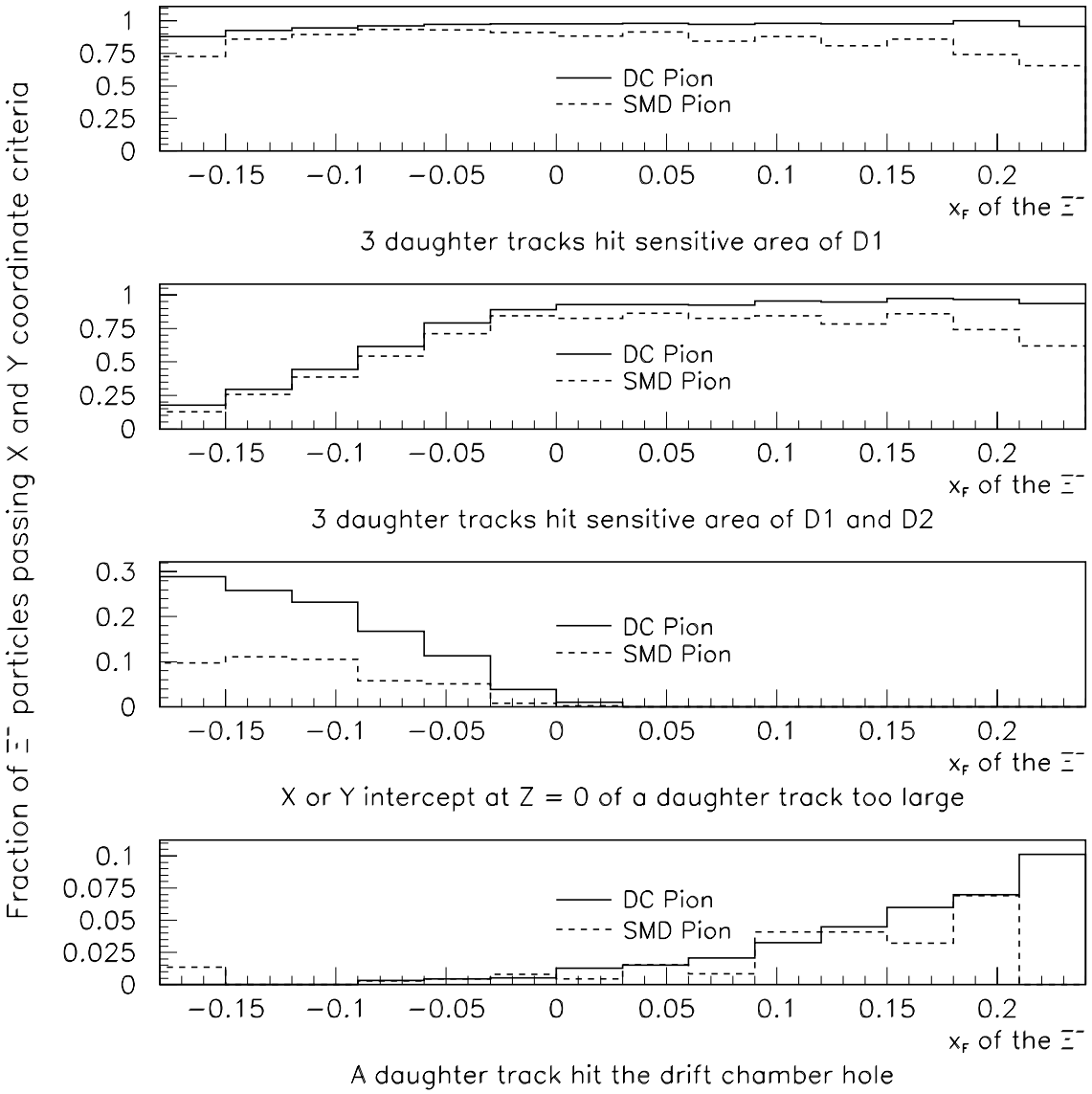

Figure A.4: Effect of geometric constraints related to the X and Y positions of Ξ^- daughter tracks on the acceptance. In all four histograms, the horizontal axis is x_F of the Ξ^-. For all the plots, both the numerator and denominator of the fractions contain only Ξ^-'s where the Λ decayed before the first drift chamber and the Ξ^- decayed after (solid line) or before (dotted line) the silicon detector. In the bottom two plots, both the numerator and denominator contain only Ξ^-'s where all three tracks struck sensitive areas of D1 and D2. D1 and D2 are the first and second drift chamber assemblies. Note the high x_F SMD pion bins suffer from very low statistics.

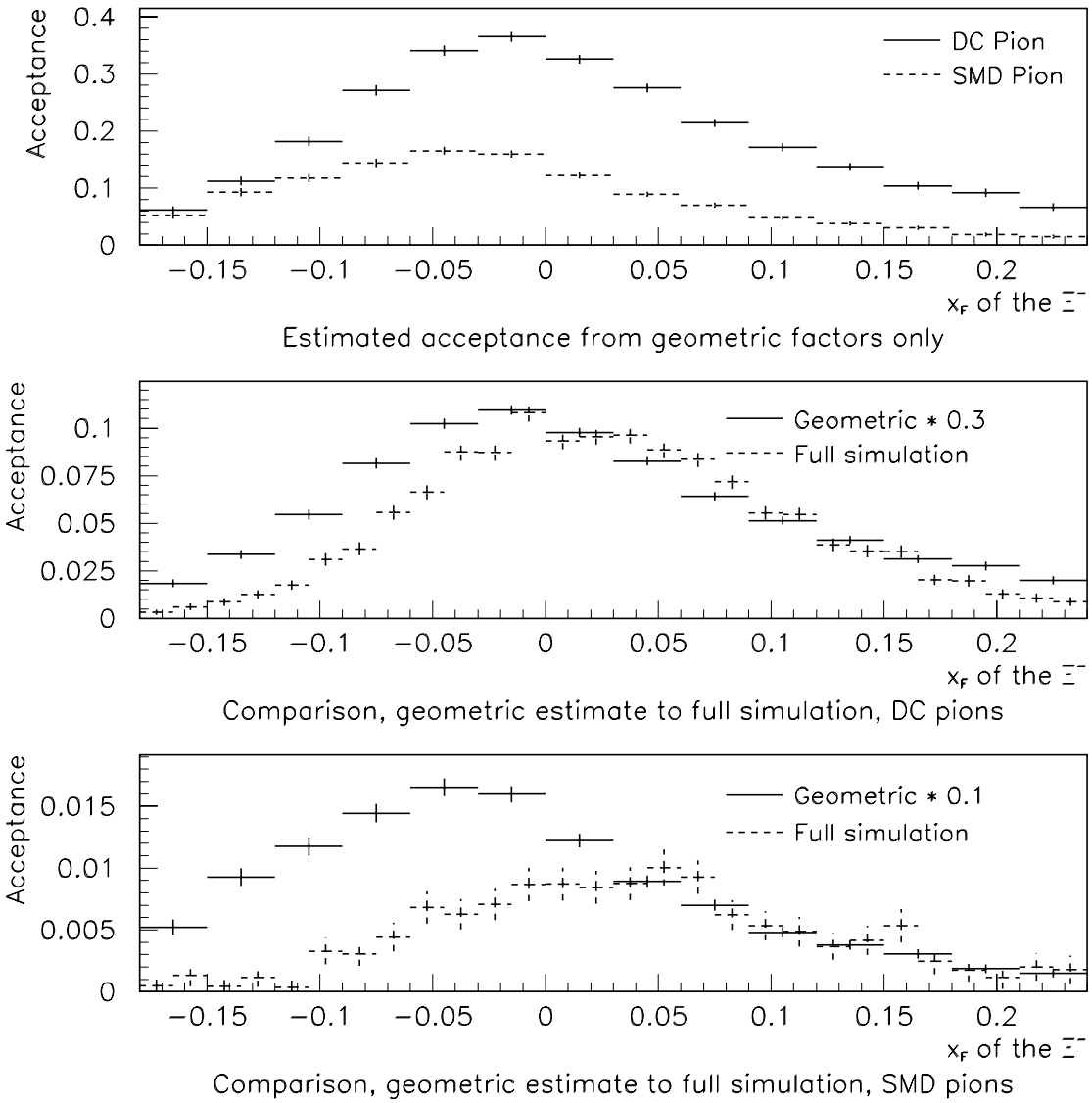

Figure A.5: The top plot shows the geometric acceptances. The other two plots compare the acceptances calculated with the full simulation (dotted lines) to the geometric acceptances (solid lines). In the lower two histograms, the geometric acceptance is normalized so that the shapes can be compared. The normalization factor was 0.3 for the Ξ^-'s reconstructed from three drift chamber tracks (middle plot), and 0.1 for Ξ^-'s with an SMD track for the pion from the Ξ^- (bottom plot). The normalization factor was chosen by eye to make the plots look nice. The difference in shape in the low x_F regions is caused by the vertex cuts. The vertex cuts remove more events at low x_F than at high x_F. The differences are larger for the Ξ^-'s reconstructed from SMD pion tracks, because the cuts are tighter. Tighter cuts are needed, because there is more combinatoric background for SMD pion tracks. All the errors bars include statistical errors only. No attempt is made to estimate the systematic errors here, but they are large.

A.4.2 Λ Lifetime and Ξ^- Lifetime

As a check, the lifetimes of the Λ and Ξ^- are measured from the data. This check is sensitive to geometric effects. In both cases, the lifetime is found to be consistent with the value reported by the Particle Data Group [25]. This gives one confidence that the geometric effects are properly modeled by the simulation. It is also a general sanity check on the entire analysis.

The Λ lifetime is measured using the Λ's that come from Ξ^- decay. Only Λ's from Ξ^- decay are used. The rest are ignored. See Figure A.6 for the acceptance calculation using the simulation. See Figure A.7 for the data distribution and Λ lifetime measurement.

The Ξ^- lifetime is determined is a similar manner. See Figure A.8 for the acceptance calculation using the simulation. See Figure A.9 for the data distribution and Ξ^- lifetime measurement.

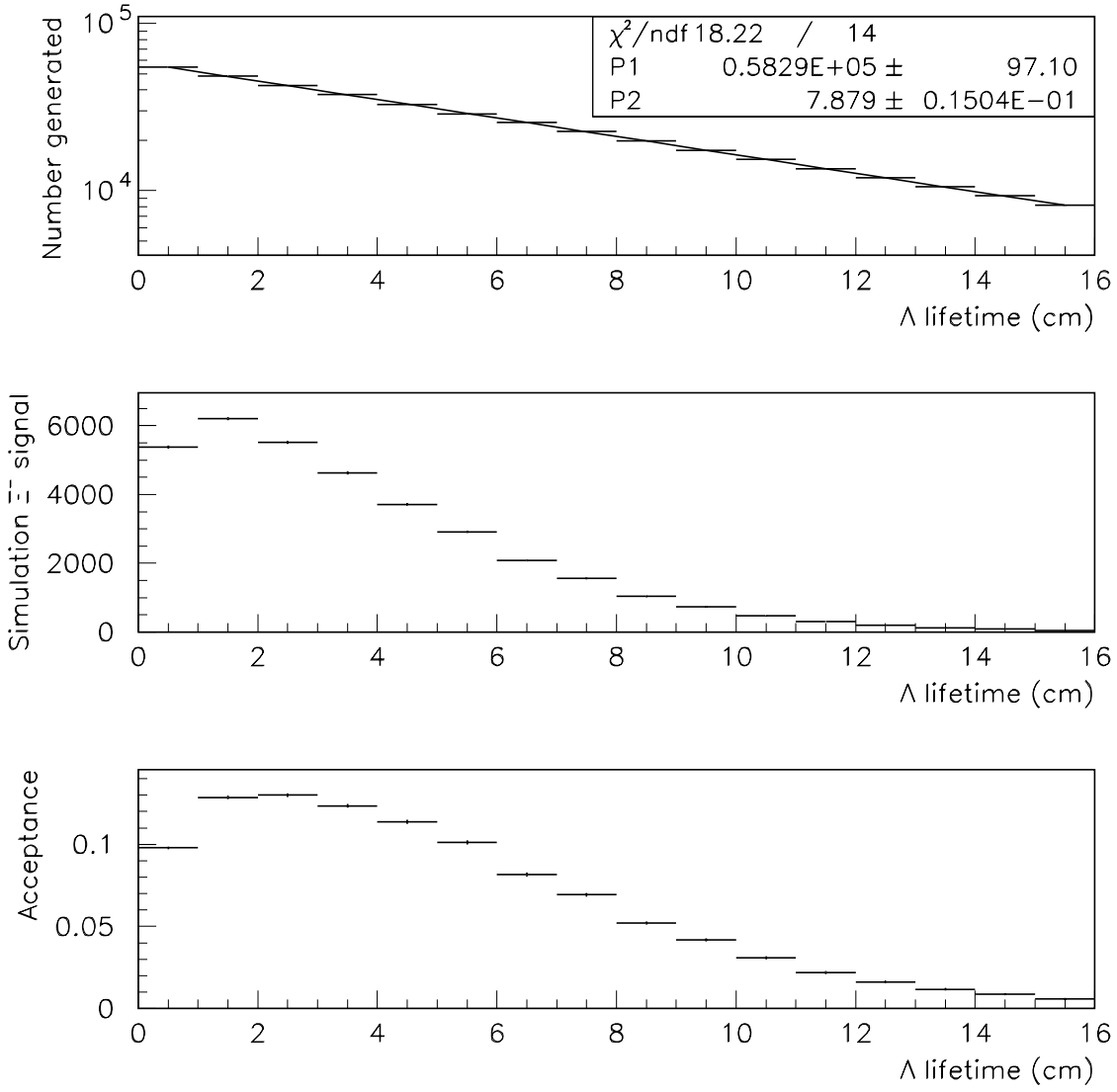

Figure A.6: The Λ lifetime acceptance calculation. The top plot shows the number of Λ's from Ξ^- decay generated in each bin of Λ lifetime. The lifetime is the proper lifetime of the Λ measured in centimeters. The lifetime is calculated using the truth table positions of the death of the Ξ^- and the birth of the π^- from the Λ decay. The Λ lifetime from the PDG [25] is 7.89 ± 0.06 cm. The second parameter in the fit is the lifetime, 7.88 ± 0.02 cm. The generated Λ's have the correct lifetime. The middle plot shows the Ξ^- signal in each bin of Λ lifetime in the reconstructed simulation sample. In this plot, the lifetime is calculated using the reconstructed Ξ^- decay vertex and the reconstructed Λ decay vertex. The primary analysis cuts for 3 drift chamber track Ξ^-'s are used to determine the signals. Background is subtracted. The bottom plot shows the acceptances as a function of Λ lifetime. This is simply the ratio of the other two plots.

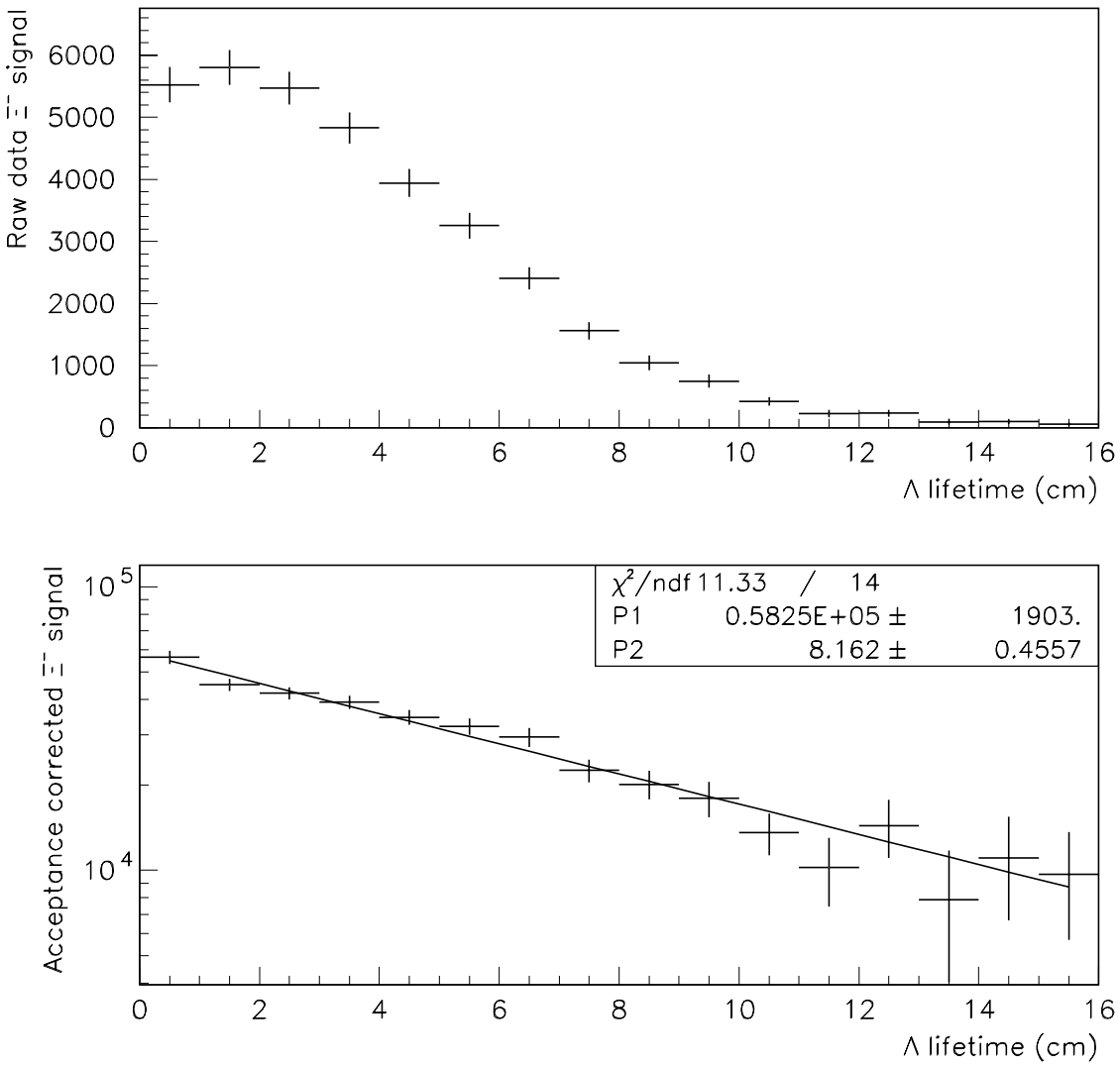

Figure A.7: The Λ lifetime calculated from data. The top plot shows the data Ξ^- signal in each bin of Λ lifetime. The lifetime is based on the reconstructed Ξ^- vertex and the reconstructed Λ decay vertex. These are background subtracted Ξ^- signals passing the primary cuts for 3 drift chamber track Ξ^-'s. The top plot is before the acceptance correction is made. The bottom plot is after the acceptance correction is made. The data is fit to an exponential. The χ^2 of the fit is excellent. The second parameter of the fit is the measured Λ lifetime, 8.16 ± 0.46 cm. This is consistent with the PDG [25] value, 7.89 ± 0.06 cm.

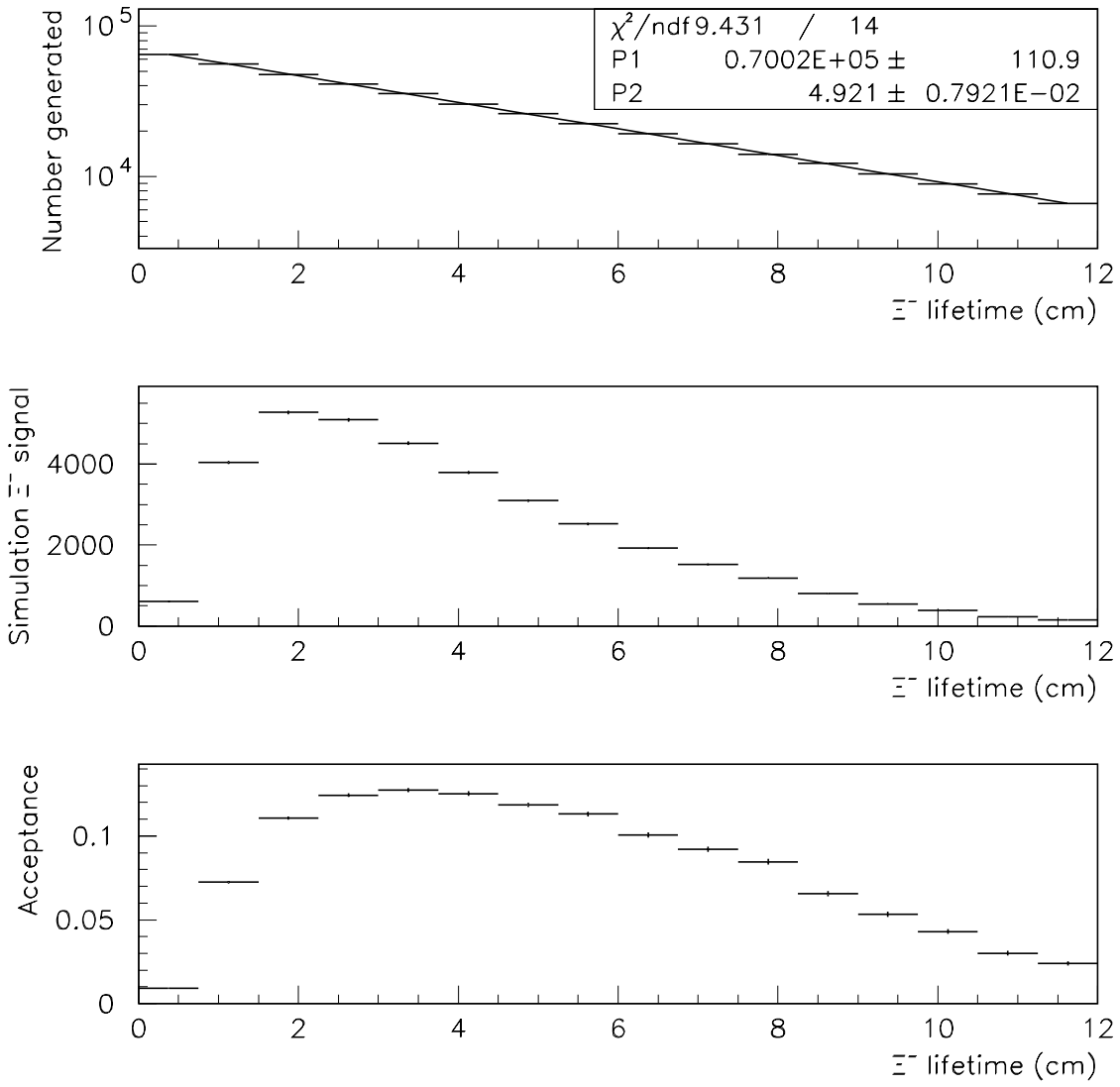

Figure A.8: The Ξ^- lifetime acceptance calculation. The top plot shows the number of Ξ^-'s generated in each bin of Ξ^- lifetime. The lifetime is the proper lifetime of the Ξ^- measured in centimeters. The lifetime is calculated using the truth table positions of the birth and death of the Ξ^- track. The lifetime from the PDG [25] is 4.91 ± 0.04 cm. The second parameter of the fit gives 4.921 ± 0.008 cm. The generated Ξ^-'s have the correct the lifetime distribution. The middle plot shows the Ξ^- signal in the reconstructed simulation sample. In this plot, the lifetime is calculated using the reconstructed Ξ^- decay vertex and the reconstructed primary vertex. This is a background subtracted Ξ^- signal in each bin of Ξ^- lifetime. The primary analysis cuts for 3 drift chamber track Ξ^-'s are used. The bottom plot shows the acceptance as a function of Ξ^- lifetime. This is simply the ratio of the other two plots.

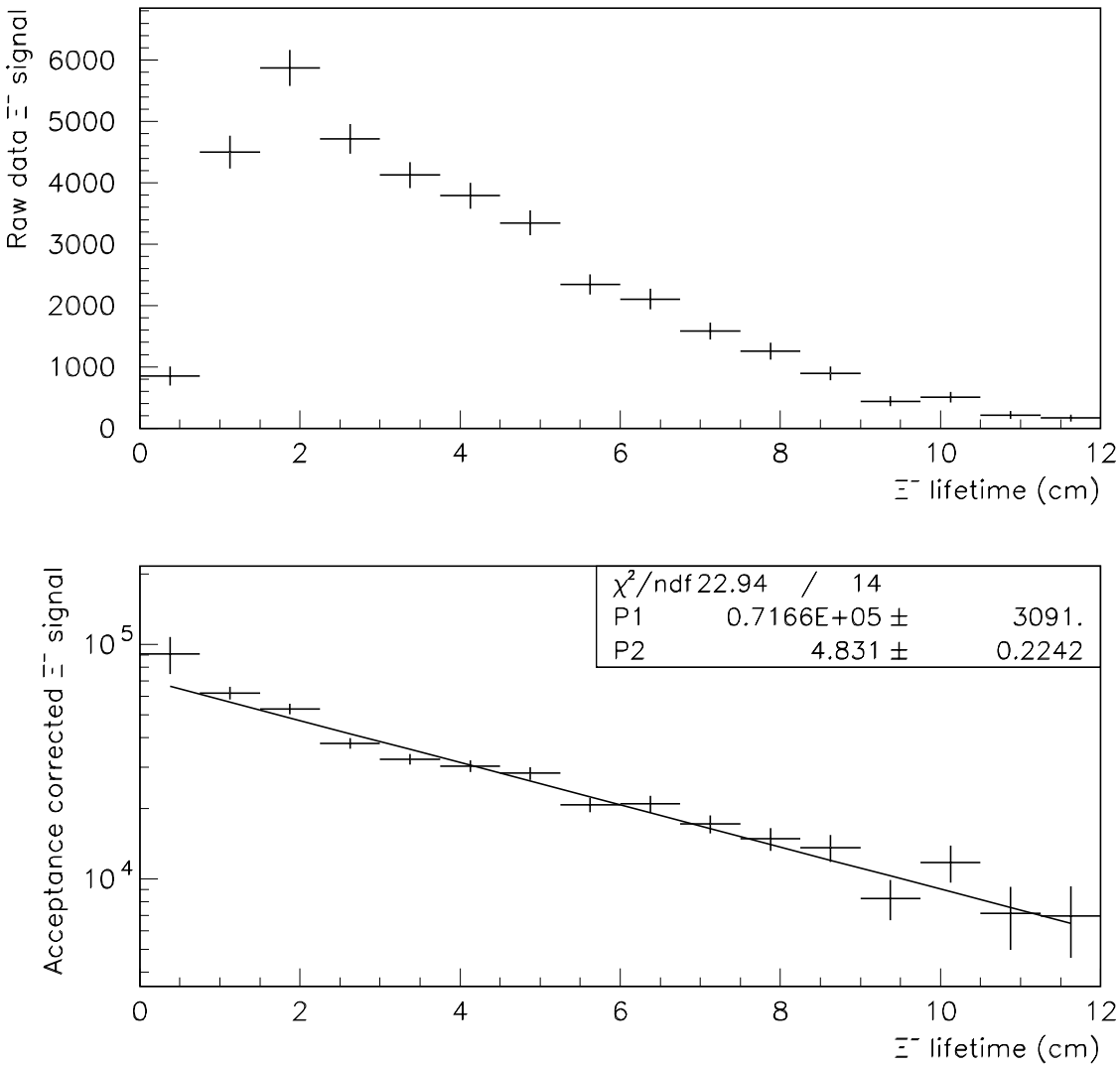

Figure A.9: The Ξ^- lifetime calculated from data. The top plot shows the data Ξ^- signal in each bin of Ξ^- lifetime. The lifetime is based on the reconstructed Ξ^- vertex and the reconstructed primary vertex. These are background subtracted Ξ^- signals passing the primary cuts for 3 drift chamber track Ξ^-'s. The top plot is before the acceptance correction is made. The bottom plot is after the acceptance correction is made. The data is fit to an exponential. The χ^2 of the fit is a little high. It may be statistics, but there could be some small systematic effects that are not being modeled properly by the simulation. The second parameter of the fit is the Ξ^- lifetime, 4.8 ± 0.2 cm. This is consistent with the PDG [25] value, 4.91 ± 0.04 cm.

Appendix B

CDF Research Activities

As a graduate student, I also spent a little more than two years working as part of the CDF (Collider Detector at Fermilab) collaboration. This work was not related to the dissertation topic, but it was a valuable part of my physics education. I gained experience helping to build systems to collect data. I did not get this experience in the Fermilab E769 collaboration, because the experiment was run long before I started.

I wrote the stub reconstruction software for the CMX muon detector in CDF. The CMX detector is a system with eight layers of drift tubes sandwiched between two layers of scintillators. It covers the range of pseudorapidity between 0.6 and 1.0 on both sides of the CDF detector. It has a rather complicated geometry with the layers positioned on the surfaces of cones for 3/4 of its coverage in phi and positioned like irregular spokes in a wheel for the other 1/4 of its coverage in phi. The reconstruction software deals with the raw data format, applies calibration corrections, finds patterns of hits that are consistent with charged tracks passing through the detector, and performs fits to determine the location and direction of muon tracks. The three dimensional fit to the drift distances allows one to measure the position of muon tracks in phi and pseudorapidity. The new code was written in C++ and interfaced with many other new software packages written for CDF in

preparation for the next run. I also tested and debugged the CMX code and many other related pieces of code.

Before I did the muon work, I was involved in testing and evaluating the Objectivity database system. Objectivity was one of three competing options for event data storage. We benchmarked the read/write speed of the database and measured disk space overheads [67]. We also developed a prototype module for data input/output. The collaboration reviewed the three options based on many criteria. The ROOT I/O system was selected and work on Objectivity was stopped in May of 1998.

For 18 months, I did work on the top mass analysis. I performed studies to compare the Dalitz-Goldstein-Sliwa mass fitting technique with the standard chi-squared fitting technique used to derive the published top quark mass. In particular, I measured the fraction of time each fitter assigned the reconstructed jets to the correct partons in simulated $t\bar{t}$ events. There were several steps in this work.

- First, I reproduced the results of the published analysis. It took a full year to get to the point where I could reproduce the published results. A lot of the time was spent simply learning and understanding a complex analysis. Unfortunately, a lot of time was wasted because the code resided in private areas (instead of the CDF code repository) and was poorly documented and controlled.

- A second task involved getting the Dalitz-Goldstein-Sliwa mass fitter code running for the decay channel with one charged lepton, four jets, and one neutrino. The existing version of this code (written by Krzysztof Sliwa) had not been run in a couple years and needed a few fixes. I interfaced it with the code used in the published analysis. The fitter was modified to use the same common blocks for input as the chi-squared fitter.

- The third step involved writing parton matching code. This code looked at the partons associated with the decaying top and anti-top quarks in the truth

table. It looked at the reconstructed jets to find matches. Then it looked at the output of the two fitters to measure how often the fitters assigned the correct partons to the correct jets. Exactly the same criteria and code were used to measure this for both fitters.

One of the major advantages of the Dalitz-Goldstein-Sliwa mass fitter was supposed to be that it found the correct match between jets and partons more often, but this had never been carefully measured. The study showed that the chi-squared fitter found the correct match $26.2 \pm 0.5\%$ of the time. The Dalitz-Goldstein-Sliwa fitter identified the correct match $24.0 \pm 0.5\%$ of the time. The chi-squared fitter did a better job.

Bibliography

[1] G. A. Alves *et al.*, Phys. Rev. D **56**, 6003 (1997).

[2] W. D. Dagenhart, in *Proceedings of the 9th Meeting of the Division of Particles and Fields of the American Physical Society, DPF 96 The Minneapolis Meeting, 1996*, edited by K. Heller and J. K. Nelson (University of Minnesota) and D. Reeder (University of Wisconsin), World Scientific, 880 (1998).

[3] W. D. Dagenhart, *Atomic Mass Dependence of the Charged Cascade Strange Cross-Section*, Fermilab E769 Internal Memo, 1996 (unpublished).

[4] D. Griffiths, *Introduction to Elementary Particles* (John Wiley & Sons, New York, 1987).

[5] J. J. Thomson, Phil. Mag. **44**, 293 (1897).

[6] E. Rutherford, Phil. Mag. **6**, 669 (1911).

[7] J. Chadwick, Nature **129**, 312 (1932).

[8] E. W. Cowan, Phys. Rev. **94**, 161 (1954).

[9] M. Gell-Mann, Phys. Lett. **8**, 214 (1964).

[10] G. Zweig, CERN 8419/TH.412, 1964 (unpublished).

[11] V. E. Barnes *et al.*, Phys. Rev. Lett. **12**, 204 (1964).

[12] O. W. Greenberg, Phys. Rev. Lett. **13**, 598 (1964).

[13] J. D. Björken, Phys. Rev. **179**, 1547 (1969).

[14] C. G. Callan and D. Gross, Phys. Rev. Lett. **22**, 156 (1969).

[15] M. Breidenbach *et al.*, Phys. Rev. Lett. **23**, 935 (1969).

[16] J. J. Aubert *et al.*, Phys. Rev. Lett. **33**, 1404 (1974).

[17] J. E. Augustin *et al.*, Phys. Rev. Lett. **33**, 1406 (1974).

[18] S. W. Herb *et al.*, Phys. Rev. Lett. **39**, 252 (1977).

[19] F. Abe *et al.*, Phys. Rev. Lett. **74**, 2626 (1995).

[20] S. Abachi *et al.*, Phys. Rev. Lett. **74**, 2632 (1995).

[21] H. Fritzsch, M. Gell-Mann, and H. Leutwyler, Phys. Lett. **47B**, 365 (1972).

[22] S. Weinberg, Phys. Rev. Lett. **31**, 494 (1973).

[23] D. J. Gross and F. Wilczek, Phys. Rev. Lett. **30**, 1343 (1973); Phys. Rev. D **8**, 3633 (1973); Phys. Rev. D **9**, 980 (1974).

[24] T. Sjöstrand, PYTHIA 5.6 and JETSET 7.3 Physics and Manual, CERN-TH.6488/92, 1992 (unpublished).

[25] C. Caso *et al.* (Particle Data Group), *Review of Particle Physics*, European Physical Journal **C3**, 1 (1998).

[26] S. Fredrikkson *et al.*, Phys. Rep. **144**, 187 (1987).

[27] A. S. Carroll *et al.*, Phys. Lett. **61B**, 303 (1976).

[28] A. S. Carroll *et al.*, Phys. Lett. **80B**, 319 (1979).

[29] A. S. Carroll *et al.*, Phys. Lett. **80B**, 423 (1979).

[30] R. J. Glauber, in *Lectures in Theoretical Physics*, edited by W. E. Brittin and L. G. Dunham (Interscience Publishers Inc., New York, 1959).

[31] C. De Marzo *et al.*, Phys. Rev. D **29**, 2476 (1984).

[32] N. N. Nikolaev, Sov. J. Part. Nucl. **12**, 63 (1981).

[33] D. S. Barton *et al.*, Phys. Rev. D **27**, 2580 (1983).

[34] A. Beretvas *et al.*, Phys. Rev. D **34**, 53 (1986).

[35] L. G. Pondrom, Phys. Rep. **122**, 57 (1985).

[36] L. Kluberg *et al.*, Phys. Rev. Lett. **38**, 670 (1977).

[37] D. Antreasyan *et al.*, Phys. Rev. D **19**, 764 (1979).

[38] R. L. McCarthy *et al.*, Phys. Rev. Lett. **40**, 213 (1978).

[39] G. A. Alves *et al.*, Phys. Rev. Lett. **70**, 722 (1993).

[40] M. J. Leitch, in Proceedings of Workshop on Charmonium Production in Relativistic Nuclear Collisions, Los Alamos National Laboratory LA-UR-98-3370, New Mexico, 1998 (unpublished).

[41] M. I. Adamovich *et al.*, Z. Phys. C **76**, 35 (1997).

[42] K. Heller *et al.*, Phys. Rev. D **16**, 2737 (1977).

[43] R. C. Hwa, Phys. Rev. Lett. **52**, 492 (1984).

[44] A. Capella and J. Tran Thanh Van, Z. Phys. C **10**, 249 (1981).

[45] K. Zalewski, in Proceedings of the X Int. Symp. Multiparticle Dynamics, Tata Institute, Bombay, 1980 (unpublished).

[46] V. V. Anisovich *et al.*, Nucl. Phys. **B133**, 477 (1978).

[47] A. Bialas and E. Bialas, Phys. Rev. D **20**, 2854 (1979).

[48] F. Takagi, Phys. Rev. D **27**, 1461 (1983).

[49] C. W. Gay, Ph.D. thesis, University of Toronto, 1991.

[50] J. F. Astorga, Ph.D. thesis, Tufts University, 1995.

[51] R. Jedicke, Ph.D. thesis, University of Toronto, 1991.

[52] S. F. Takach, Ph.D. thesis, Yale University, 1993.

[53] D. A. Passmore, Ph.D. thesis, Tufts University, 1995.

[54] A. F. Wallace, Ph.D. thesis, Yale University, 1997.

[55] V. K. Bharadwaj *et al.*, Nucl. Instrum. Methods **228**, 283 (1985).

[56] D. J. Summers, Nucl. Instrum. Methods **228**, 290 (1985).

[57] J. A. Appel *et al.*, Nucl. Instrum. Methods **243**, 361 (1986).

[58] Institute of Electrical and Electronics Engineers (IEEE), *CAMAC Instrumentation and Interface Standards*, (IEEE, distributed in cooperation with Wiley-Interscience, New York, 1982).

[59] C. Gay and S. Bracker, IEEE Trans. Nucl. Sci. **34**, 870 (1987).

[60] S. Hansen *et al.*, IEEE Trans. Nucl. Sci. **34**, 1003 (1987).

[61] C. Stoughton and D. J. Summers, Computers in Physics **6**, 371 (1992).

[62] T. Sjöstrand, Comput. Phys. Commun. **39**, 347 (1986).

[63] T. Sjöstrand and M. Bengtsson, Comput. Phys. Commun. **43**, 367 (1987).

[64] H.-U. Bengtsson and T. Sjöstrand, Comput. Phys. Commun. **46**, 43 (1987).

[65] H. Pi, Comput. Phys. Commun. **71**, 173 (1992).

[66] R. Milburn, [E769.TARGET]TARGET.DFN, Internal Fermilab E769 Note, 1987 (unpublished).

[67] W. D. Dagenhart *et al.*, *An Interim Status Report from the Objectivity/DB Working Group*, Internal CDF Note 4522, 1998 (unpublished).